Strain engineering graphene and bilayer graphene transport properties

Inauguraldissertation

zur
Erlangung der Würde eines Doktors der Philosophie
vorgelegt der
Philosophisch-Naturwissenschaftlichen Fakultät
der Universität Basel

von

Blesson Sam Varghese

Basel, 2024

Genehmigt von der Philosophisch-Naturwissenschaftlichen Fakultät
auf Antrag von
Erstbetreuer: Prof. Dr. Christian Schönenberger
Zweitbetreuerin: Prof. Dr. Ilaria Zardo
Externer Experte: Prof. Dr. Christoph Stampfer
Externer Experte: Prof. Dr. Adrian Bachtold

Basel, 14.11.2023

Prof. Dr. Marcel Mayor
Dekan

Contents

1 Introduction

Strain engineering is a broad field with significant applications in technology and industry. For example, it plays a important role in optimizing mechanical, electrical, optical properties of a material or in analyzing manufactured parts in industry [1, 2]. However, strain is also of interest in fundamental research, as it allows to modulate material structures in a controlled way, starting from the inter-atomic distances to superstructures of folds and crystallites [3–7]. Specifically, strain has been demonstrated to enhance the mobility of the active channel [8, 9] in transistors leading to improved conductivity [10–12]. Moreover, strain can tune the band gap in semiconductors [13, 14] which is a key property utilized in optoelectronic devices [15] like in Light Emitting Diodes (LED) for better performance [16]. In all these applications, strain develops mostly due to a lattice mismatch [17] of two different material grown on top of each other, thus making the strain permanent and not in-situ tunable. For fundamental research, it is more interesting to change the strain in-situ, so that changes in the material properties can be directly monitored without comparing different devices, that, while macroscopically might be identical, can still differ significantly on the microscopic scale. Ideally, we then would prefer to investigate a material in which the material properties can be resonably easily understood from a tight-binding picture, with the hopping parameters changing with the atomic displacement, i.e., with strain.

In 3D bulk crystals, strain can cause mechanical failure as the interlayer bonds are stronger covalent or ionic bonds leading to lack of flexibility, thus engineering tunable strain is a challenge in such systems. With the advent of two dimensional van der Waals materials (2D materials) lead to more possibilities for strain engineering [18]. Two key properties, namely high tensile strength and mechanical flexibility [19–21] makes van der Waals materials an ideal platform to explore strain effects on crystal lattices, bandstructures, electronic and optical properties, possibly even in nanoscale quantum systems. Numerous techniques have been developed to generate strain in 2D materials, including thermal expansion mismatch [22], pre-patterned substrate [23], bending of substrate [24, 25], comb-drive actuator method [26]. The effect of strain on optical properties in 2D materials is mostly investigated in terms of band gap tuning and its application in devices like solar cells (exciton fun-

nel effect) [27, 28], photo detectors [29], quantum emitters [30], light emitting materials [31]. Additionally, strain also drive phase transitions in certain 2D materials such as inducing magnetic phase change in CrSBr, a van der Waals magnet material [32].

Strain effects on charge carrier transport is a new field to explore. The key factors to study strain effect on transport includes the quality of electrical contacts and the compatibility with straining techniques. Since contacts and gates have to be fabricated, cleanliness is usually problematic (e.g. polymer residues), and since in transport experiments the resulting total currents result from an average over the complete device volume, the actual interpretation can become problematic. On the other hand, transport experiments allow to access various parameters, like the density of states and mean-free-paths in a more direct way, so our aim is to combine various techniques in this thesis, like Raman spectroscopy and transport experiments. The possibility of excellent electrical contacts [33] and the ability to withstand high in-plane strain [19] makes graphene and bilayer graphene ideal candidates for investigating strain effects on charge carrier transport. Strain is a new tuning knob in addition to charge carrier density, magnetic field, displacement field in transport experiments. In graphene, strain is predicted to induce changes in the bandstructure through scalar potential [34, 35], an anisotropy of the Fermi velocity [36], a pseudo-magnetic vector potential [37], pseudo magnetic field [38, 39]. In the case of bilayer graphene, the interlayer hopping [40] gives rise to effective charge carrier mass. While the strain-induced effects predicted in graphene may also be observable in bilayer graphene (BLG), there can be additional effects from strain specific to BLG, like effect on charge carrier mass or effect on interlayer symmetry breaking.

The hBN-encapsulated graphene also has some very specific experimental advantages, namely the great device qualities with mobilities of 100,000 cm^2/Vs [41, 42] even in the fabrication-intensive devices of this thesis, as well as a fixed geometry and electrical capcitance, even when bending the substrates to generate the strain, which makes the correct interpretation less ambiguous.

In this thesis, we discuss effects observed in transport and Raman spectroscopy experiments in graphene, bilayer graphene under uniaxial tensile strain at cryogenic temperatures (typically either 4.2K or 1.6K) and in magnetic fields up to 9T. The initial section of the thesis will describe the special technique developed in this project which allows us to apply and control strain while in-situ measuring the electrical and optical signals. We extend some efforts to distinguish strain effects on the metallic contacts and the interface to the graphene from actual changes in the graphene properties, and investigate how to generate not only spatially constant strain, but also strain gradient, expected to

result in anisotropic hopping and thus pseudo-magnetic fields.

Outline of this thesis

In this thesis we describe the development of a new low temperature strain setup which combines optics and charge carrier transport and enables to study the effects strain plays on quantum transport of charge carriers in graphene and bilayer graphene.

In **Chapter 2** the essential theoretical background for the experiments is described. It starts with an introduction to graphene, bilayer graphene crystal structure and the low energy dispersion in these crystal lattices followed by charge carrier transport in such systems. Further a brief introduction to the mechanics of substrate bending is given to provide an understanding of how strain is generated in graphene. The final part briefly describes the predicted strain effects in the bandstructure of graphene.

In **Chapter 3** an overview of the fabrication steps and experimental setup used is provided. The preparation of flexible susbtrates and the mechanism of strain transfer from the bent susbtrate to the graphene device is discussed, along with the mechanical bending setup. Last, the technique used to electrically connect a device to the measurement electronics as well as on low temperature transport measurement is described.

Chapter 4 introduces the new low temperature three point bending setup which we designed and constructed to combine optical experiments with transport experiments. The design, components, working of the setup and the integration of the setup into the attocube system[1] is described in detail. This new setup provides the possibility to characterise strain at low temperature (up to 1.6 K) and high magnetic field (up to 9 T). The technique introduced to measure the bending deflection of the substrate (Δz) using capacitor sensor is also described. In the final part, an estimate for the tensile strain at the top surface of substrate obtained using the bending profile is compared to the strain generated in graphene devices using Raman spectroscopy.

In **Chapter 5** effects of strain on edge contacts to graphene are investigated. Assuming a mobility independent of charge carrier density, the change in conductance corresponds to the tuning of contact resistance from the diffusive transport model. As the mobility of device is large enough to give a mean free path comparable to device dimensions, a ballistic transport model is discussed in addition, resulting in the same overall picture as an increase in effective

[1] attodrY2100 confocal Raman scanning microscopy system.

transmission probability of carriers into the metallic reservoirs. The final section discusses the possible mechanisms that might play a role in changing this transmission or contact resistance.

Chapter 6 reports one of the strain effects on the crystal lattice, namely the strain induced scalar potential observed in graphene [35] and similar effect observed in bilayer graphene (BLG). In transport experiment this scalar potential appears as shift in the position of charge neutrality point (CNP) in gate voltage or in fact of any feature occuring at a specific electron density. The observation of the shift is shown in both graphene and bilayer graphene followed by an estimate for the scalar potential constant in both systems.

Chapter 7 discusses specific effect of strain in charge transport of bilayer graphene. First, the conductance around the charge neutral point (CNP) increases with the tensile strain. Whether the effect is from a change in mobility of the device or a signature of change in density of states is still a question. These early experiments, however, had one degree of freedom not controlled, namely the dielectric displacement field, which in bilayer graphene results in a change of the energy gap and the mass of the parabolic bandstructure. For this reason, we developed dual-gated bilayer graphene (BLG) devices for our strain experiments, with an additional top gate fabricated on our BLG multiterminal devices. Interestingly, we still find strain effects, in spite of the strong encapsulation. Specifically, the width of the conductance curve with charge carrier density around the CNP increased with tensile strain. Is it an effect related to the scalar potential or is it an effect from change in interlayer distance still remains ? The final section shows the strain effect on BLG/hBN moire at finite electric field.

In **Chapter 8** we demonstrate strain engineering in encapsulated graphene junctions using different device geometries. Specifically, we demonstrate that we can generate strain gradient along and perpendicular to the current direction, which we can quantitatively understand in simple models with simple boundary conditions, which in turn can later be used to design more complex device geometry for specific strain patterns. This control developed in tuning strain and strain gradient can be extended to other 2D van der Waals material systems.

The work in the thesis is summarised in the final **Chapter 9**, with perspectives and future directions.

2 Theoretical background

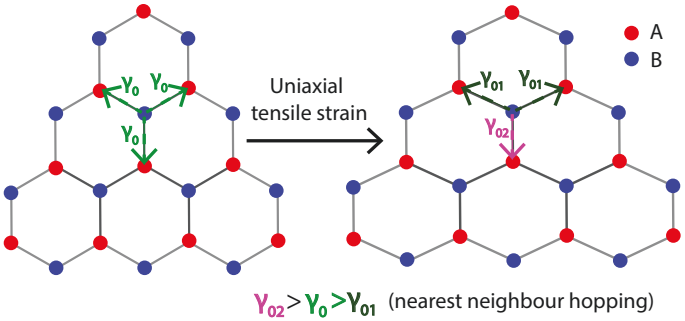

This chapter introduces the essential theory background for the experiments carried out in this thesis. It starts with an introduction to the basics of graphene and bilayer graphene on crystal structure, low energy electronic dispersion [40, 43]. The next section discusses the basics on charge transport and different transport regimes: diffusive and ballistic transport, quantum hall effect. The transition to straining the encapsulated graphene junction begins with introduction to mechanics of bending and arriving at a general differential equation for plate bending [44]. With the simply supported boundary condition for the plate an expression for the bending profile is obtained. Further the technique used to characterize strain is discussed with a brief introduction to Raman spectroscopy in graphene. In the final part, the effect of strain on the electronic properties of graphene is discussed. Strain can change the potential energy of the system, can lead to Fermi velocity anisotropy [1], and can distort the reciprocal space lattice [37].

[1] Schematic showing anisotropy in nearest neighbour hopping under uniaxial strain in graphene lattice. Arrows represent hopping

2.1 Graphene

Graphene, a single layer of graphite is the first two dimensional material extracted. It is a sheet of carbon arranged in honey comb structure as shown in Fig. 2.1(a). Each carbon (C) atom has 6 electrons where $1s^2$ $2s^2$ $2p^2$ is its electronic configuration. The electrons in $1s^2$ orbital are inert and do not contribute to any chemical bonds. The 2s orbital hybridizes with $2p_x$ and $2p_y$ to form three planar sp^2 orbitals. The four valence electrons occupy three sp^2 orbitals and the $2p_z$ orbital. The sp^2 orbitals form the well localised σ bond whereas the $2p_z$ orbitals form the delocalised π bond which contribute to the π band in graphene. The covalent bond between C atoms is one of the strongest bond and thereby making the graphene lattice robust. The tight binding model with nearest neighbour interaction is discussed in the following to derive the low energy dispersion of graphene which results from the electrons in the $2p_z$ orbital.

2.1.1 Graphene lattice , reciprocal lattice

The graphene lattice has two kinds of C atoms however they are not chemically different. The difference is built into the geometry of the lattice structure. Fig. 2.1(a) shows two C atoms A, B and translation from A, B with same vector results in a final position with different nearest neighbour surrounding. Thereby, the primitive unit cell of graphene has two atoms A and B spanned by the following two lattice vectors:

$$\vec{a}_1 = \frac{a_0}{2}\begin{pmatrix} 3 \\ \sqrt{3} \end{pmatrix} \qquad \text{and} \qquad \vec{a}_2 = \frac{a_0}{2}\begin{pmatrix} 3 \\ -\sqrt{3} \end{pmatrix} \tag{2.1}$$

The two different C atoms A and B can be seen as forming two sublattices. Here, $a_0 = 1.42$ Å is the inter-atomic distance. Each A atom directly neighbors three B atoms and vice versa, as depicted in Fig. 2.1(a). In real space, the nearest-neighbors are connected by vectors,

$$\vec{\delta}_1 = a_0\begin{pmatrix} 1 \\ 0 \end{pmatrix} \qquad \text{and} \quad \vec{\delta}_2 = \frac{a_0}{2}\begin{pmatrix} -1 \\ -\sqrt{3} \end{pmatrix} \quad \text{and} \quad \vec{\delta}_3 = \frac{a_0}{2}\begin{pmatrix} -1 \\ \sqrt{3} \end{pmatrix}. \tag{2.2}$$

The reciprocal lattice is shown in Fig. 2.1(b) with the hexagon being the first Brillouin zone. The two reciprocal lattice vectors are given by

$$\vec{b}_1 = \frac{2\pi}{3a_0}\begin{pmatrix} 1 \\ \sqrt{3} \end{pmatrix} \qquad \text{and} \qquad \vec{b}_2 = \frac{2\pi}{3a_0}\begin{pmatrix} 1 \\ -\sqrt{3} \end{pmatrix} \tag{2.3}$$

which are obtained by the relation $\vec{a_i}\vec{b_j} = 2\pi\delta_{ij}$.

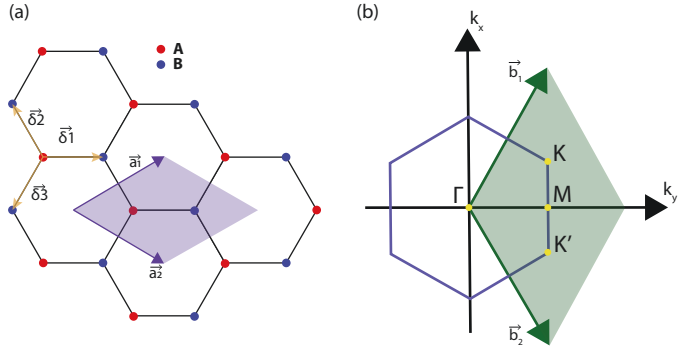

Figure 2.1 Real and reciprocal space lattice of graphene. (a) Unit cell (shaded in violet) of graphene containing two atoms (A and B) spanned by the two lattice vectors $\vec{a_1}$ and $\vec{a_2}$ in real space. **(b)** The first Brillouin zone shown as hexagon spanned by the two reciprocal lattice vectors $\vec{b_1}$ and $\vec{b_2}$. The two inequivalent sets of valleys K and K' sit at the six corners of the Brillouin zone.

2.1.2 Tight binding model in graphene lattice

The tight binding model based on the principles of quantum mechanics, well describes the properties of tightly bound electrons in a system. It describes a system where an electron only shows minimal interaction with its other neighbours. The assumption is that tightly bound electrons can only hop between nearest neighbour atoms. The electrons in $2p_z$ orbitals contribute to π band in graphene which in turn forms the low energy dispersion of graphene. Let $\phi(\vec{r})$ represent the p_z orbital of the C atom at position $\vec{r}$. Thus for the unit cell atoms A and B,

$$\phi_A = \phi(\vec{r} - \vec{R}) \tag{2.4}$$

$$\phi_B = \phi(\vec{r} - \vec{R} - \vec{\delta_1}) \tag{2.5}$$

where $\vec{R}$ is the real space lattice vector. $\vec{R} = m_1\vec{a}_1 + m_2\vec{a}_2$ where m_1,m_2 are integers and $\vec{a}_1$,$\vec{a}_2$ are the two basis lattice vectors described in susbec. 2.1.1. The wave function(ψ_k) is taken to be the linear combination of atomic orbitals ϕ_A and ϕ_B,

$$\psi_\mathrm{k}(\vec{r}) = \frac{1}{\sqrt{N}} \sum_{\vec{R}} e^{i\vec{k}\vec{R}} (c_A\phi_A + c_B\phi_B), \tag{2.6}$$

where N is the nuber of unit cells, $\mathrm{c_A}$ and $\mathrm{c_B}$ are the unknown coeffcients of contributions of basis to ψ_k. The Hamiltonian for the graphene crystal lattice

can be written as,

$$H = \frac{p^2}{2m_e} + \sum_{\vec{R}} (V_o(\vec{r} - \vec{R}) + V_o(\vec{r} - \vec{R} - \vec{\delta_1})) \tag{2.7}$$

where V_o represents the atomic potential. The Hamiltonian acting on ϕ_A and ϕ_B gives

$$\begin{aligned} H\phi_A &= (\frac{p^2}{2m_e} + V_o(\vec{r}))\phi_A + V_o(\vec{r} - \vec{\delta_1})\phi_A + \sum_{\vec{R}\neq 0} (V_o(\vec{r} - \vec{R}) + V_o(\vec{r} - \vec{R} - \vec{\delta_1}))\phi_A \\ &= \epsilon_{p_z}\phi_A + \Delta V_A \phi_A \end{aligned} \tag{2.8}$$

Similarly,

$$H\phi_B = \epsilon_{p_z}\phi_B + \Delta V_B \phi_B \tag{2.9}$$

where ϵ_{pz} is the energy of p_z orbital and let's choose $\epsilon_{pz} = 0$, then:

$$\begin{aligned} H\phi_A &= \Delta V_A \phi_A \\ H\phi_B &= \Delta V_B \phi_B \end{aligned} \tag{2.10}$$

The Schrodinger equation for the system gives,

$$H\psi_k = E\psi_k \tag{2.11}$$

The projection of ϕ_A and ϕ_B onto ψ_k gives two equations,

$$\begin{aligned} \int \phi_A^* H\psi_k \, d^3r &= E \int \phi_A^* \psi_k \, d^3r \\ \int \phi_B^* H\psi_k \, d^3r &= E \int \phi_B^* \psi_k \, d^3r \end{aligned} \tag{2.12}$$

Further taking into account the three nearest neighbour gives the matrix equation as shown in [45],

$$\begin{pmatrix} \sigma - E & \alpha^*(k)(\gamma_0 - Es) \\ \alpha(k)(\gamma_0 - Es) & \sigma - E \end{pmatrix} \times \begin{pmatrix} c_A \\ c_B \end{pmatrix} = \begin{pmatrix} 0 \\ 0 \end{pmatrix} \tag{2.13}$$

where,

$$\begin{aligned} \sigma &= 3 \int \phi_A^* V_o(\vec{r} - \vec{\delta_1})\phi_A \, d^3r \\ \alpha(k) &= 1 + e^{i\vec{k}(\vec{\delta_2} - \vec{\delta_1})} + e^{i\vec{k}(\vec{\delta_3} - \vec{\delta_1})} \\ \gamma_0 &= \int \phi_A^* V_o(\vec{r})\phi_B \, d^3r \\ s &= \int \phi_A^* \phi_B \, d^3r \end{aligned} \tag{2.14}$$

In the eigen value problem in Eq. 2.13 we assume the overlap integral(s) to be small. This gives the energy eigenvalues (E),

$$E(\vec{k}) = \sigma \pm \gamma_0 |\alpha(k)| \tag{2.15}$$

where σ is the first order shift in the atomic levels due to the remaining crystal lattice and it is a constant. Thus on redefining the zero of energy gives,

$$E(\vec{k}) = \pm\gamma_0 \sqrt{1 + 4\cos\left(\frac{3}{2}k_x a_0\right)\cos\left(\frac{\sqrt{3}}{2}k_y a_0\right) + 4\cos^2\left(\frac{\sqrt{3}}{2}k_y a_0\right)} \tag{2.16}$$

where γ_0 is the nearest neighbour hopping energy, $\gamma_0 \approx$ -2.8eV [43]. On plotting E($\vec{k}$) vs $\vec{k}$ gives the graphene bandstructure in k space as shown in Fig. 2.2. In pristine graphene, the Fermi level lies at zero energy.

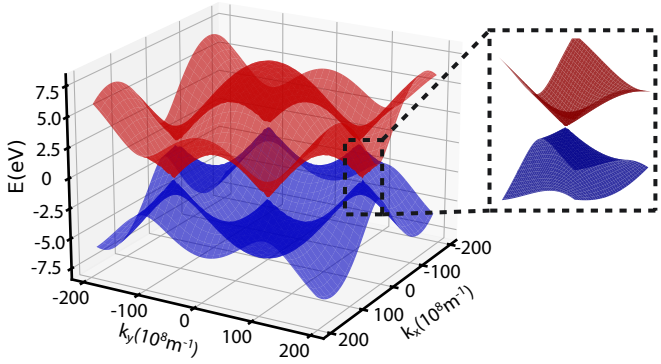

Figure 2.2 Graphene bandstructure. The band structure of graphene plotted for the first Brillouin zone (BZ) using Eq. 2.16. The zoom in around the region where conduction (red) and valence(blue) band touch each other shows the dirac cone of the bandstructure. These dirac points are located at the corners of the BZ. Except at these points in k space, graphene bandstructure is gapped.

2.1.3 Graphene bandstructure peculiarities

Fig. 2.2(a) clearly shows that graphene band structure is gapped except at two points in the brillouin zone (BZ). The points where conduction and valence band touches coincides with the K and K' points in the BZ, these points are called Dirac points and it represents the two distinct valleys in k space .

Graphene bandstructure around these K and K' points will be discussed in the following.

Valley degree of freedom

The two distinct valleys in k space are consequence of two sublattice namely A and B in the real space lattice of graphene,Fig. 2.1(a). Both K and K' valleys are degenerate in energy but inequivalent as they cannot be connected by a reciprocal lattice vector ($\vec{G}$). Thus the charge carriers in graphene have a new degree of freedom called valley degeneracy, in addition to the magnetic spin degeneracy. Two such K and K' points of the Brillouin zone are located at

$$\vec{K} = \frac{2\pi}{3a_0}\begin{pmatrix} 1 \\ 1/\sqrt{3} \end{pmatrix} \qquad \text{and} \qquad \vec{K}' = \frac{2\pi}{3a_0}\begin{pmatrix} 1 \\ -1/\sqrt{3} \end{pmatrix}, \tag{2.17}$$

respectively. The momentum mismatch between the K and K' valley is large thus intervalley scattering is strongly suppressed for long-range scattering, making valley a good quantum number in graphene in such scattering events but not for local defect scattering.

Linear dispersion

The zoom-in of graphene band structure around Dirac points shows that it is linear at low energies,as shown in Fig. 2.2. Mathematically, this can be shown by Taylor expanding Eq. 2.16 around K point with $\vec{k} = \vec{K} + \vec{q}$, where $|\vec{q}| \ll |\vec{K}|$ is the momentum measured from the K point, this results in (the same expansion can be found for the K' point),

$$E_{\pm}(\vec{q}) = \pm\hbar v_f |\vec{q}|, \tag{2.18}$$

where $\hbar$ is the reduced Planck constant and $v_f = 3\gamma_0 a_0/(2\hbar) \approx 10^6 ms^{-1}$ is the Fermi velocity. The + (-) denotes conduction (valence) band. The linearized Hamiltonian for both valleys can be written as

$$H_0 = \hbar v_f(\kappa q_x \hat{\sigma}_x - q_y \hat{\sigma}_y) \tag{2.19}$$

with $\kappa = +(-)$ for the K (K') valley and $\hat{\sigma}_i$'s are the Pauli matrices acting on the sublattice space. This is similar to the Hamiltonian for a massless relativistic particle. Therefore, charge carriers in graphene are often described as "massless" Dirac Fermions with Fermi velocity v_f, similar to the energy dispersion in photons. With the relation $q = \sqrt{\pi \mathrm{n}}$, the Fermi energy of charge carriers(E_f) can be connected to charge carrier density (n) by,

$$E_f(n) = \hbar v_f \sqrt{\pi n} \tag{2.20}$$

Density of states

The density of states (DoS) in graphene is given by,

$$DoS(E) = \frac{g_s g_v E}{2\pi(\hbar v_f)^2}, \tag{2.21}$$

where $g_s = g_v = 2$ are the degeneracies due to spin and valley. The linear dependance of DoS on energy is a consequence of the linear energy dispersion relation in graphene.

2.2 Bilayer graphene

Bilayer graphene (BLG) is a two layer graphene system with one layer sitting on top of the other. The two layers are held together by van der Waals intercation between the $2p_z$ orbitals. Depending on how the top layer is arranged with respect to the bottom layer there are two types of stacking for bilayer graphene, AA and AB stacking namely. A and B represents the two different carbon atoms in each of the two graphene layers.

In AA stacking ,the A atom of top layer sits directly above A atom of the bottom layer whereas in AB stacking, the A atom of top layer sits directly above B atom of the bottom layer. Fig. 2.3(a),(b) shows the crystal lattice structure and bandstructure for AB stacked bilayer graphene. The energy dispersion in AB bilayer grpahene will be discussed in the following.

2.2.1 Energy dispersion in Bilayer graphene

The unit cell has four atoms which lead to presence of different hopping terms. The interlayer hopping in bilayer graphene (BLG) is schematically illustrated in Fig. 2.3(a). The intralayer hopping between A1(A2) and B1(B2) in the lower(upper) layer is same as the nearest neighbour hopping in single layer graphene. Therefore, we write the in-plane hopping term as $\gamma_0 = t = 2.8\,\text{eV}$. Another hopping terms arises from the interlayer coupling. The interlayer hopping term includes the following [47]: (a) between A2 and B1 atom which sits directly above each other, γ_1= 0.38eV (b) between A1 and B2 atom , γ_3= 0.38eV (c) between B1 and B2 atom, γ_4 = 0.14eV as shown in Fig. 2.3(a). The Hamiltonian for bilayer graphene considering both intra and interlayer

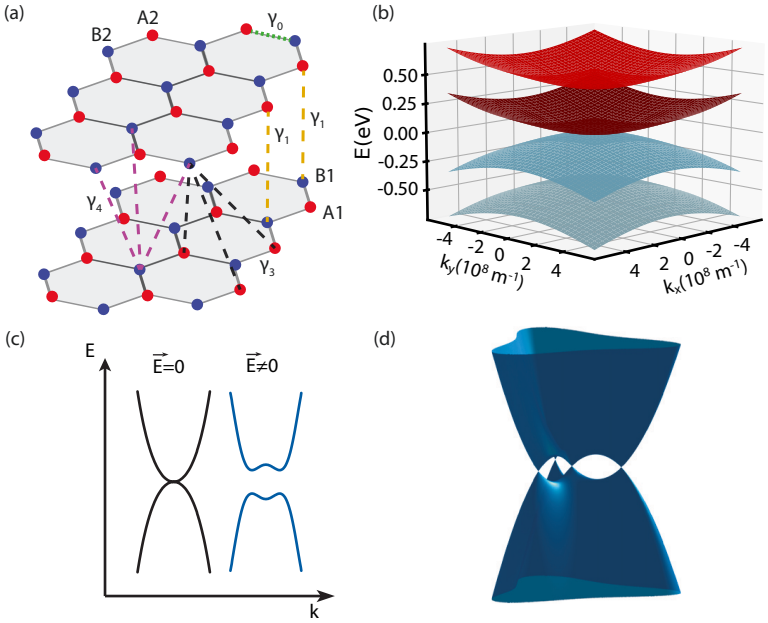

Figure 2.3 Band structure of bilayer graphene. **(a)** The lattice of an AB stacked bilayer graphene shown in real space with all relevant hopping terms indicated by γ_i. **(b)** Low energy dispersion relation in BLG plotted with Eq. 2.26 when $\left|\vec{k}\right| \ll k_0$. **(c)** Band structure around the K point without and with a perpendicular electric field. A finite gap opens up with electric field. The trigonal warping is not taken into account. Figure is adapted from Ref. [46]. **(d)** Low energy spectrum at the K valley including trigonal warping. Figure is adapted from Ref. [46].

hopping terms is ,

$$H_{BLG} = \begin{pmatrix} \epsilon_{A1} & -\gamma_0\alpha(k) & \gamma_4\alpha(k) & -\gamma_3\alpha^*(k) \\ -\gamma_0\alpha^*(k) & \epsilon_{B1} & \gamma_1\alpha(k) & \gamma_4\alpha(k) \\ \gamma_4\alpha^*(k) & \gamma_1 & \epsilon_{A2} & -\gamma_0\alpha(k) \\ -\gamma_3\alpha(k) & \gamma_4\alpha^*(k) & -\gamma_0\alpha^*(k) & \epsilon_{B2} \end{pmatrix} \tag{2.22}$$

The term $\gamma_0\alpha$(k) describes same as discussed for graphene Hamiltonian previously in Eq. 2.14. The terms ϵ_{A1}, ϵ_{B1}, ϵ_{A2}, ϵ_{B2} describes the onsite energy of the atoms in the unit cell. Three parameters are introduced to describe the on site energy differences of the four atoms in the unit cell (A1,B1,A2,B2) in the most general case: (a) Interlayer asymmetry (U), (b) energy difference between dimer(A2-B1) and non-dimer site(B2-A1) (Δ') (c) energy difference of the A and B sites(δ_{AB}) [40].

$$\begin{aligned} U &= \frac{1}{2}((\epsilon_{A1} + \epsilon_{B1}) - (\epsilon_{A2} + \epsilon_{B2})) \\ \Delta' &= \frac{1}{2}((\epsilon_{B1} + \epsilon_{A2}) - (\epsilon_{A1} + \epsilon_{B2})) \\ \delta_{AB} &= \frac{1}{2}((\epsilon_{A1} + \epsilon_{A2}) - (\epsilon_{B1} + \epsilon_{B2})) \end{aligned} \tag{2.23}$$

The onsite energies can now be expressed in terms of the above mentioned parameters in Eq. 2.23. For the case of $\delta_{AB} = 0$, $\Delta' = 0$ and only non-zero interlayer asymmetry U, $\epsilon_{A1} = \epsilon_{B1} =$ -$U/2$ and $\epsilon_{A2} = \epsilon_{B2} =$ U/2. The hopping term γ_4 can be neglected as it is small compared to γ_0,γ_1,γ_3. Then the eigen energies of the Hamiltonian, H_{BLG} are $E = E_m^\alpha$, α = 1,2 represents the valence and conduction band, m = 1,2 describes the two subbands (lower and upper) in each of the conduction and valence band. Thus there are four energy bands for bilayer graphene. "U" describes the difference of potential between the two layers, which can, for example, be tuned by an external perpendicular electric field [48]. The eigne value of H_{BLG} are [40],

$$E_m^2 = \frac{\gamma_1^2}{2} + \frac{U^2}{2} + (v_f^2 + \frac{v_3^2}{2})\hbar^2k^2 + (-1)^\alpha\sqrt{J} \tag{2.24}$$

$$J = \frac{1}{4}(\gamma_1^2 - v_3^2\hbar^2k^2)^2 + v_f^2\hbar^2k^2(\gamma_1^2 + U^2 + v_3^2\hbar^2k^2) + 2\kappa\gamma_1v_3v_f^2\hbar^3k^3cos3\phi \tag{2.25}$$

where $v_f = \sqrt{3}a_0\gamma_0/2\hbar$, $v_3 = \sqrt{3}a_0\gamma_3/2\hbar$, $v_4 = \sqrt{3}a_0\gamma_4/2\hbar$,$\kappa = \pm1$(valley index). In an intermediate energy range $(v_3/v_f)^2 < E_1 < \gamma_1$ we can neglect γ_3 and for the case in which $U = 0$, the energy dispersion takes the form,

$$E_m^\alpha = (-1)^\alpha \cdot \frac{\gamma_1}{2} \pm \frac{\gamma_1}{2}\sqrt{1 + (\vec{k}/k_0)^2}. \tag{2.26}$$

where $k_0 = \gamma_1/2\hbar v_f$. The lowest energy bands represented by $\pm E_1$ comes from the non-dimer sites A1, B2 and the higher energy bands ($\pm E_2$) comes from

the dimer sites A2, B1. These two bands are seperated in energy by γ_1.

Density of states

For small $\vec{k}$ ($\left|\vec{k}\right| \ll k_0$), Eq. 2.26 describes a parabolic dispersion relation with an effective mass $m^* = \gamma_1/(2v_f^2) \sim 0.03m_e$, where m_e is the free electron mass. For large $\vec{k}$ ($\left|\vec{k}\right| \gg k_0$), the dispersion relation becomes linear. The turning point is around a charge carrier density of $5{\times}10^{12}\mathrm{cm}^{-2}$. The low energy density of states in bilayer graphene (BLG) is independent of energy due to the parabolic dispersion relation.

$$DoS(E) = \frac{4m^*}{2\pi\hbar^2}, \tag{2.27}$$

where the factor 4 accounts for the spin and valley degeneracy.

But including the hopping parameters γ_3 , γ_4 results in changing the topology of bandstructure at low energies from parabola to four mini Dirac cones as shown in Fig. 2.3 resulting in a trigonal shaped band. This effect is called trigonal warping. The transition of Fermi surface from a single circle to four circles occurs at an energy scale $\sim$ 1 meV [49]. By breaking the interlayer symmetry a gap can be opened in BLG by an external perpendicular electric field as schematically shown in Fig. 2.3(c). BLG under finite electric field will be discussed in Ch. 7.

2.3 Charge transport in graphene

The thesis focuses on charge transport in graphene with strain as a new tuning knob. For the better understanding of the experiments it will be vital to know the basic concepts in transport. So this section will introduce different transport regimes in graphene.

The source (S) and drain (D) edge contacts in the fabricated device junctions (as shown in Fig. 3.8) serves the dual role of straining the junction and enabling charge transport through graphene/bilayer graphene (channel). In the transport studies, a small voltage bias, V_{SD} is applied between S and D electrode, this drives a current, I_{SD} through the channel. The conductance of graphene junction is then, $G = I_{SD}$ / V_{SD}. In addition device is equipped with a global back gate (V_{bg}) to tune the charge carrier density (n) in the channel.

As the charge moves according to the direction of bias, transport can be diffusive or ballistic depending on the scatterer distribution. The quantities that

can quantify this is the mean free path (l_{mfp}) or momentum scattering time (τ). The l_{mfp} is the distance that charge carriers travel between two momentum scattering events whereas τ tells the time between such two momentum scattering events.

The length scale of a channel is characterized by the length (L) and width (W) of the device junction. When $l_{mfp} \ll W, L$ the transport will be diffusive as many momentum scattering events occur when charge carriers travel through the device whereas if $l_{mfp} \sim W, L$, the ballistic regime occurs. In the following, charge carrier density tuning and some details of diffusive, ballistic transport regimes will be discussed. Furthermore, the quantum Hall effect in graphene will be introduced and explain how charge carrier transport behaves in presence of magnetic field.

2.3.1 Tuning charge carrier density

The conductance (G) can be tuned by varying V_{bg} as it changes the charge carrier density (n) in graphene. The back gate voltage (V_{bg}) is applied between back gate electrode and graphene channel, with a dielectric in between. The induced charge carrier density can be estimated with a plate capacitor model,

$$C = \epsilon_0 \epsilon_r \frac{A}{d}, \tag{2.28}$$

where C is the capacitance between metal back gate and graphene, A is the device area, d is the thickness of the dielectric (hBN), ϵ_r is the relative dielectric constant, ϵ_0 is the permittivity of free space. The back gate voltage V_{bg} shifts the energy bands through the Fermi level (E_f) determined by the contacts. Due to graphene's band structure without a band gap, energy band can be tuned with respect to the Fermi level continuously from the electron to the hole regime and vice versa. Theoretically the Dirac point (E_D) in graphene can be tuned to the E_f but potential fluctuations which cannot be screened at low carrier densities prevent this in real devices. The device breaks into random electron-hole puddles near the Dirac point instead of having a homogeneous carrier density [50]. The residual doping n_0, which is the lowest homogeneous carrier density that can be realized in a device, characterizes the device quality [51] in terms of how close the Fermi level can be tuned to the Dirac point. In the following, conductivity in diffusive and ballistic transport regime will be discussed.

2.3.2 Diffusive regime and Drude model

In the diffusive regime, the Drude model describes conductivity as

$$\sigma = \frac{ne^2\tau}{m_e}, \tag{2.29}$$

where τ is the average time between two momentum scattering events, n is the charge carrier density, m_e is the electron mass, e is the electron charge. The opposing force acting on the free charge carriers from the bias and the scattering causes it to attain an average velocity. The sources for scattering can be impurities, phonons or strain fluctuations [52, 53]. The mobility (μ) in a diffusive system is given by, $\mu = e\tau/m_e$ and thus

$$\sigma = ne\mu \tag{2.30}$$

In a two-terminal configuration, the graphene resistance is measured in series with the contact resistance, R_c (including line resistance of the measurement circuit). The conductance starts to saturate at higher gate voltages because the contact resistance starts to dominate. The conductance is related to the conductivity by $\sigma = \alpha_g G$ with a geometry factor α_g, which is the aspect-ratio (L/W) of the channel. Taking the contact resistance into account, the conductance of a two-terminal device as a function of carrier density is given by

$$G^{-1} = \frac{1}{\frac{ne\mu}{\alpha} + G_0} + R_c \tag{2.31}$$

where G_0 is the residual conductance from graphene channel at charge neutrality point (CNP), where CNP corresponds to n = 0.

2.3.3 Ballistic transport

As discussed above, when $l_{mfp} \sim W, L$ the scattering in the channel is highly reduced and happens only at edges and at the contacts. In this regime the Drude model will fail to explain the conductivity of such a system. Conductance in the ballistic regime is determined by the number of modes (M), transmission probability (T_p) and degeneracy of each mode. In a pure ballistic regime, T_p=1 and the ballistic conductance in graphene (G_b) [54] is given by,

$$G_b = \frac{4e^2}{h} M T_p = \frac{4e^2}{h} \frac{W}{\lambda_f/2} = \frac{4e^2}{h} W\sqrt{n/\pi}, \tag{2.32}$$

with $\lambda_f = 2\pi/k_{yf}$ and $M = 2W/\lambda_f$. k_{yf} and k_{xf} are the x , y components of the Fermi momenta (k_f). The k_{yf} component of momenta becomes discrete as the modes need to match the width (W) of the junction, $k_{yf}^M = \pi M/W$ but the k_{xf} component remains continuous.

Temperature effects on Ballistic transport

Eq. 2.32 describes G_b at 0 K. In actual experiments the temperature (T) is finite, in our case T = 4 K. At finte bias (V_{SD}),the current due to a mode (I_M) is given by,

$$I_M = \frac{4e}{h}\int_{-\infty}^{\infty} T_{pM}(E)(f(E-\mu_S) - f(E-\mu_D))\,dE \tag{2.33}$$

where $T_{pM}(E)$ is the transmission probability of the M^{th} mode, μ_S and μ_D are the respective electrochemical chemical potential at source(S) and drain(D) contacts, $f(E-\mu_{S/D})$ is the Fermi distribution function at S/D and is given by

$$f(E-\mu_{S/D}) = \frac{1}{1+e^{\left(\frac{E-\mu_{S/D}}{k_B T}\right)}} \tag{2.34}$$

where k_B is the Boltzmann constant and T is the temperature of the bath. The transmission probability ($T_{pM}(E)$) is given by,

$$T_{pM}(E) = T_0\theta(E-(E_D+\hbar v_f k_{yf}^M)) \tag{2.35}$$

where T_0 is taken to be a constant, θ is the heaviside function, E_D is the Dirac point energy of graphene. Let E_f fixed by contacts to be the zero energy level of the system, then we get

$$E_f - E_D = -E_D = \hbar v_f\sqrt{\pi n} \tag{2.36}$$

When $E > E_D + \hbar v_f k_{yf}^M$, M^{th} mode contributes to transport if the chemical potential in the graphene is tuned into the bias window (V_{SD}) by back gate voltage (V_{bg}).

$$\mu_S - \mu_D = eV_{SD} \tag{2.37}$$

For a small bias V_{SD},

$$f(E-\mu_S) - f(E-\mu_D) = \frac{\partial f}{\partial E}eV_{SD} \tag{2.38}$$

Thus Eq. 2.33 can be rewritten as,

$$I_M = \frac{4e}{h}\int_{-\infty}^{\infty} T_{pM}(E)\Big(\frac{\partial f}{\partial E}eV_{SD}\Big)\,dE \tag{2.39}$$

Thus the condutance of the M^{th} mode can be written as ,

$$G_M = \frac{I_M}{V_{SD}} = \frac{4e}{h}\int_{-\infty}^{\infty} T_{pM}(E)\Big(\frac{\partial f}{\partial E}\Big)\,dE \tag{2.40}$$

The total conductance is,

$$G_b = \sum_M G_M \tag{2.41}$$

Ballistic conductance (G_b) with this model at T = 4 K is plotted in Fig. 2.4(a) for varying width of the junction. For $W > 500$ nm the quantised conductance step vanishes indicating numerous modes present in the system. Ballistic conductance calculated from Eq. 2.32 is equal to that from this model for $W = 3\mu$m at T = 4 K, shown in Fig. 2.4(b). So, for graphene junctions with $W \geq 3\mu$m Eq. 2.32 is sufficient to quantify G_b.

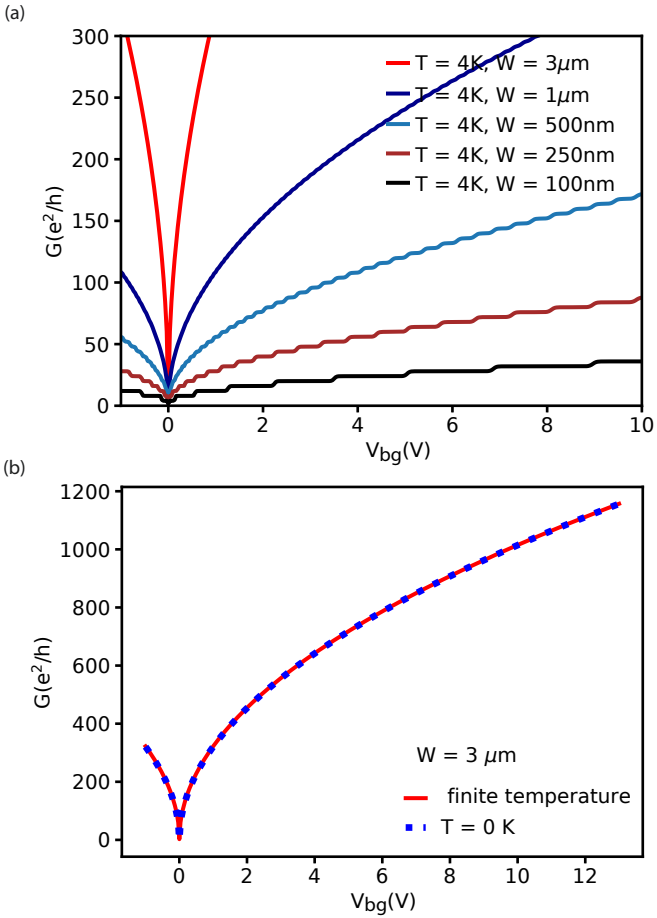

Figure 2.4 Ballistic charge transport model. (a) Ballistic conductance of channels with varying width (W) at T = 4 K. To observe the quantised conductance modes at 4K the width of junction should be less than 1 μm. **(b)** Comparing ballistic conductance including temperature factor as discussed in subsec. 2.3.3 (red solid line) and the ballisitc conductance calculated with Eq. 2.32 (blue dotted line). Both curves overlap indicating that at T = 4 K and $W = 3$ μm, Eq. 2.32 is suffcient to quantify ballistic conductance.

2.3.4 Quantum Hall effect

During charge transport, the path of the charge carriers can be changed by the presence of a perpendicular magnetic field (B) as it experiences a Lorentz force. The charge carriers exhibit cyclotron motion in the presence of perpendicular magnetic field. This deviation of charge carrier path causes it to accumulate on one edge of the sample along the direction of current flow and builds up a transverse voltage to the normal current path. The voltage measured known as Hall voltage and the effect came to be known as classical Hall effect [55]. For a 2D system, the Hall voltage $V_H = IB/ne$ where n is the charge carrier density. So, measuring V_H is a way to measure the nature of charge carrier and density. In classical Hall effect, the longitudinal resistivity is $\rho_{xx} = \frac{m}{ne^2\tau}$ and the Hall resitivity is given by $\rho_{xy} = \frac{B}{ne}$.

When the dimensions of the 2D system becomes microscopic and under high magnetic field as well as at low temperature, ρ_{xx} and ρ_{xy} show a striking behaviour. The ρ_{xy} shows plataeus in certain range of magnetic field and is generalised by,

$$\rho_{xy} = \frac{\mathrm{h}}{\nu \mathrm{e}^2} \tag{2.42}$$

where ν is an integer. The longitudinal resistivity ρ_{xx} drops to zero when ρ_{xy} is plateaued and peaks when ρ_{xy} jumps from one plateau to other. This effect came to be known as the Integer Quantum Hall Effect (QHE) [56]. The system under magnetic field causes the energy dispersion to change to discrete Landau Levels (LL). To observe QHE : a) temperature should be low enough so that thermal energy scale k_BT is less than the LL energy seperation. b) B field should be high enough so that electrons can complete circular orbits (cyclotron motion) before scattering happens.
In a classical picture, electrons make skipping orbits at edge of the system which move in opposite direction at opposite edges as B field breaks the time reversal symmetry. So the effect can be understood in terms of dissipationless edge channels carrying the current while the bulk of the system is gapped and it results in quantized hall conductance. The longitudinal and hall conductivity is given by,

$$\sigma_{xx} = \frac{\rho_{xx}}{\rho_{xx}^2 + \rho_{xy}^2} \tag{2.43}$$

$$\sigma_{xy} = -\frac{\rho_{xy}}{\rho_{xx}^2 + \rho_{xy}^2} \tag{2.44}$$

By solving the Hamiltonian for graphene under perpendicular magnetic field, the energy of the N^{th} LL [57] is

$$E_N = sign(N) v_f \sqrt{2e\hbar B|N|}, \tag{2.45}$$

The LLs are non-equidistantly spaced due to the square root dependance of N which is in contrast to conventional semiconductors with parabolic band structure. The zeroth LL is at zero energy which contains half holes and half electrons [58]. The largest LL spacing is between $N = 0$ and $N = 1$, large enough such that the QHE can be observed at room temeperature in graphene [59]. The quantum Hall conductivity of graphene is given by

$$\sigma_{xy} = \frac{g_s g_v e^2}{h}(N + 1/2) \tag{2.46}$$

with $g_s = g_v = 2$ being the spin and valley degeneracy. In case of bilayer graphene, the LL energy is given by [49, 60]

$$E_N = \pm\hbar\omega\sqrt{N(N-1)}, \tag{2.47}$$

where $\omega = eB/m$ is the cyclotron frequency , m is the cyclotron mass of charge carriers in bilayer graphene. The LLs are 4 fold degenerate due to spin and valley degeneracy except for $N = 0$ and $N = 1$. From the above expression for $E_N = 0$ for $N = 0$ and $N = 1$, thus the eigenvalue at zero energy is 8 fold degenerate and it contains half holes and half electrons. The quantum Hall conductance values are multiples of four in units of $\frac{e^2}{h}$.

The Hall bar measurements are usually done on 6 probe or 4 probe devices where ρ_{xx} and ρ_{xy} can be distinguished clearly. The two probe hall bar measurements will give an effective resistivity or conductivity which is a combination of ρ_{xx} and ρ_{xy}. When the Fermi level is positioned in between LLs there is no conduction in the bulk of the system but only along the edge. So the conductance plateau with B field will still be clear in two probe hall bar measurements [61].

2.4 Mechanics of Bending

The strain attained in the experiments in this thesis is achieved by bending the substrate. To get an understanding of the mechanism, it is vital to introduce the bending of plates mechanics first and try to deduce the strain on the top surface from the bending curvature of the substrate. The substrate used for experiments can be considered in the limit of thin plates [44] as t/L or $t/W \ll 1$ where t is the thickness of substrate, L and W are the in plane length and width of substrate. In the following we will discuss about plate bending, derive plate bending equation and further use it to get the bending profile of the substrate using the boundary conditions in the bending setup. This section follows the Ref. [44].

2.4.1 Plate bending

A plate is a flat structural element where its thickness is small compared to its surface dimensions. Let's consider the plate lying in xy-plane and its thickness (h) in the z direction.

Assumptions
The three basic assumption in plate bending theory is :
(a) Midplane - middle plane section of plate with zero in-plane stress and strain. The bending of plate will cause the layers above and below the midplane to be deformed in-plane.
(b) The line elements in the thickness direction remain perpendicular to the midplane before and after deformation. The corresponding strain components, $\varepsilon_{xz} = \varepsilon_{yz} = 0$.
(c) Line elements lying perpendicular to midplane remain unchanged in length and thus the strain component $\varepsilon_{zz} = 0$.

Stress and strain components in plate
For a three dimensional object there are nine stress and strain components. There are three normal components and the other six are the shear components. These stress components produce resultants such as normal force, shear force and moments in the 3D object. We define these resultants in the following.
Let $\sigma_{ij}/\epsilon_{ij}$ represent the stress/strain components, describing the stress/strain acting on j^{th} directed face in the i^{th} direction where i,j = x,y,z (Cartesian coordinate axis), as illustrated in Fig. 2.5(a).
The in-plane normal forces and bending moments are defined as (Fig. 2.5(b)),

$$N_x = \int_{-h/2}^{+h/2} \sigma_{xx}\, dz\,, \quad N_y = \int_{-h/2}^{+h/2} \sigma_{yy}\, dz \tag{2.48}$$

$$M_x = -\int_{-h/2}^{+h/2} z\sigma_{xx}\, dz\,, \quad M_y = -\int_{-h/2}^{+h/2} z\sigma_{yy}\, dz \tag{2.49}$$

The in-plane shear forces and twisting moment are defined as (Fig. 2.5(c)),

$$N_{xy} = \int_{-h/2}^{+h/2} \sigma_{xy}\, dz \tag{2.50}$$

$$M_{xy} = \int_{-h/2}^{+h/2} z\sigma_{xy}\, dz \tag{2.51}$$

Out of plane shearing forces are defined as (Fig. 2.5d),

$$V_x = \int_{-h/2}^{+h/2} z\sigma_{zx}\, dz\,, \quad V_y = \int_{-h/2}^{+h/2} z\sigma_{yz}\, dz \tag{2.52}$$

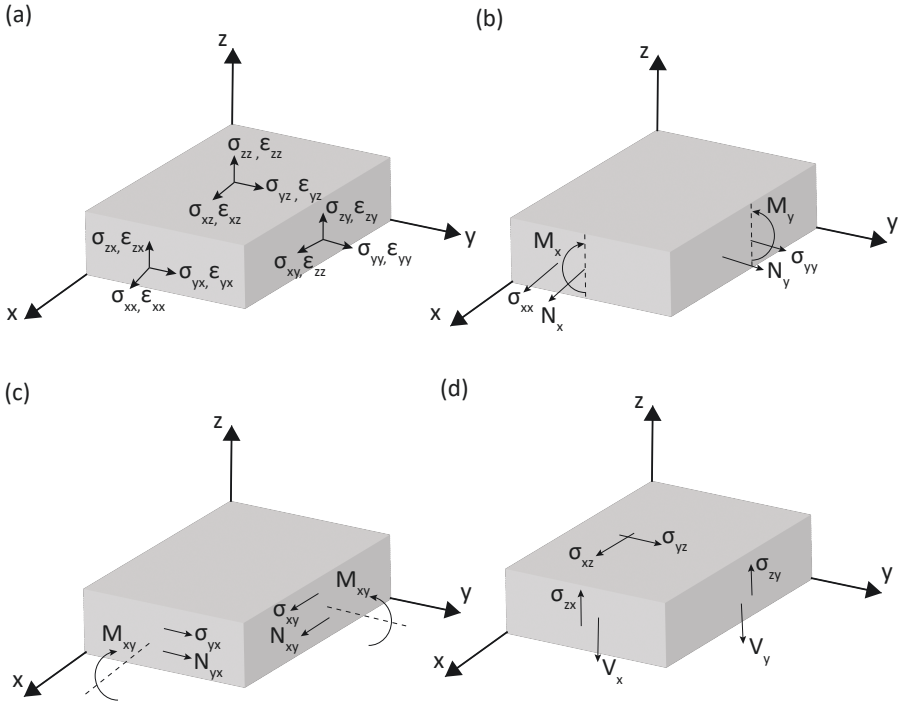

Figure 2.5 Stress, strain components and stress resultants. (a) Stress and strain components on the xy, zx, zy plane face of the cuboidal block. **(b)** In-plane normal forces(N_x , N_y) and bending moments (M_x,M_y) due to the normal in plane stress components σ_{xx} , σ_{yy}. **(c)** In-plane shear forces(N_{xy}) and twisting moment(M_{xy}) resulting from shear stress component σ_{xy}. **(d)** Out of plane shear force resulting from σ_{zx} , σ_{zy} stress components.

2.4.2 Expressions for stress and strain resultants

Let w(x,y,z) represent the general vertical displacement of any point on the plate and similarly u(x,y,z) and v(x,y,z) represent the general in-plane displacements in the x and y direction. Consider a line element lying in x-axis of length Δx. Let the deformed and original length of element be denoted by $|a'b'|$ and $|ab|$, as illustrated in Fig. 2.6.

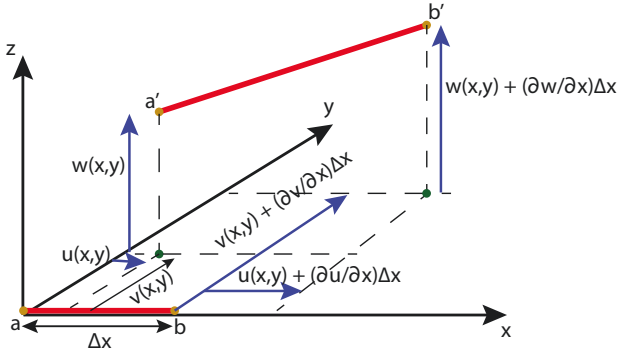

Figure 2.6 Calculating ϵ_{xx}. A line element "ab" of the plate is lying along the x- axis. Upon deformation the line element gets displaced in the x,y,z directions and its length changes. The quantities u, v, w represents the displacement to the points in ab in x,y,z direction. The length of ab changes upon deformation, the strain in the x direction acting on the element due to the deformation force in x direction(ε_{xx})is calculated.

Using Pythogora's theorem we can write,

$$\varepsilon_{xx} = \frac{|a'b'| - |ab|}{|ab|} = \sqrt{\left(1 + \frac{\partial u}{\partial x}\right)^2 + \left(\frac{\partial v}{\partial x}\right)^2 + \left(\frac{\partial w}{\partial x}\right)^2} - 1 \tag{2.53}$$

For small bending, displacement gradients are approximated to be small. Thus the square and product terms of it can be neglected. Thus,

$$\varepsilon_{xx} = \frac{\partial u}{\partial x} \tag{2.54}$$

Similar calcualtion along y and z direction gives,

$$\varepsilon_{yy} = \frac{\partial v}{\partial y} \quad , \varepsilon_{zz} = \frac{\partial w}{\partial z} \tag{2.55}$$

The shear strain components are as follows:

$$\varepsilon_{xy} = \frac{1}{2}\left(\frac{\partial u}{\partial y} + \frac{\partial v}{\partial x} + \frac{\partial w}{\partial x}\frac{\partial w}{\partial y}\right), \varepsilon_{xz} = \frac{1}{2}\left(\frac{\partial u}{\partial z} + \frac{\partial w}{\partial x}\right), \varepsilon_{yz} = \frac{1}{2}\left(\frac{\partial v}{\partial z} + \frac{\partial w}{\partial y}\right) \tag{2.56}$$

From the assumptions made intially ($\varepsilon_{xz} = \varepsilon_{yz} = 0$) for plate bending,

$$\frac{\partial u}{\partial z} = -\frac{\partial w}{\partial x} \quad , \frac{\partial v}{\partial z} = -\frac{\partial w}{\partial y} \tag{2.57}$$

Thus we get,

$$u(x, y, z) = -z\frac{\partial w}{\partial x} + u_0(x, y, 0) \tag{2.58}$$

$$v(x, y, z) = -z\frac{\partial w}{\partial y} + v_0(x, y, 0) \tag{2.59}$$

$$w(x, y, z) = w_0(x, y, 0) \tag{2.60}$$

where u_0, v_0, w_0 are midplane displacements. The strain components in terms of the midplane displacements are then,

$$\varepsilon_{xx} = \frac{\partial u_0}{\partial x} - z\frac{\partial^2 w}{\partial^2 x} \tag{2.61}$$

$$\varepsilon_{yy} = \frac{\partial v_0}{\partial x} - z\frac{\partial^2 w}{\partial^2 y} \tag{2.62}$$

$$\varepsilon_{xy} = \frac{1}{2}\Big(\frac{\partial u_0}{\partial y} + \frac{\partial v_0}{\partial x}\Big) - z\frac{\partial^2 w}{\partial x \partial y} \tag{2.63}$$

From the assumptions of plate theory, the midplane is free of stress components. Thus the strain components become,

$$\varepsilon_{xx} = -z\frac{\partial^2 w}{\partial^2 x}\,, \quad \varepsilon_{yy} = -z\frac{\partial^2 w}{\partial^2 y}\,, \quad \varepsilon_{xy} = -z\frac{\partial^2 w}{\partial x \partial y} \tag{2.64}$$

Let the Young's modulus and Poisson ratio of the material be E and ν. From the assumptions $\sigma_{zz} = 0$. Further, from the Hooke's law we can write [62],

$$\varepsilon_{xx} = \frac{1}{E}\sigma_{xx} - \frac{\nu}{E}\sigma_{yy} \tag{2.65}$$

$$\varepsilon_{yy} = \frac{1}{E}\sigma_{yy} - \frac{\nu}{E}\sigma_{xx} \tag{2.66}$$

$$\varepsilon_{xy} = \frac{1+\nu}{E}\sigma_{xy} \tag{2.67}$$

Now combining Eq. 2.64 and 2.67 gives,

$$\sigma_{xx} = -\frac{E}{1-\nu^2}z\Big(\frac{\partial^2 w}{\partial^2 x} + \nu\frac{\partial^2 w}{\partial^2 y}\Big) \tag{2.68}$$

$$\sigma_{yy} = -\frac{E}{1-\nu^2}z\Big(\frac{\partial^2 w}{\partial^2 y} + \nu\frac{\partial^2 w}{\partial^2 x}\Big) \tag{2.69}$$

$$\sigma_{xy} = -\frac{E}{1+\nu} z \frac{\partial^2 w}{\partial x \partial y} \tag{2.70}$$

Now using the stress resultants defined in Subsec. 2.4.1 we get,

$$M_x = D\Big(\frac{\partial^2 w}{\partial^2 x} + \nu \frac{\partial^2 w}{\partial^2 y}\Big) \tag{2.71}$$

$$M_y = D\Big(\frac{\partial^2 w}{\partial^2 y} + \nu \frac{\partial^2 w}{\partial^2 x}\Big) \tag{2.72}$$

$$M_{xy} = -D(1-\nu)\frac{\partial^2 w}{\partial x \partial y} \tag{2.73}$$

where $D = \frac{Eh^3}{12(1-\nu^2)}$. The prefactor D is called plate stiffness or flexural rigidity. The stress components and moments are directly related by

$$\sigma_{xx} = -\frac{M_x z}{h^3/12},\ \sigma_{yy} = -\frac{M_y z}{h^3/12},\ \sigma_{xy} = -\frac{M_{xy} z}{h^3/12} \tag{2.74}$$

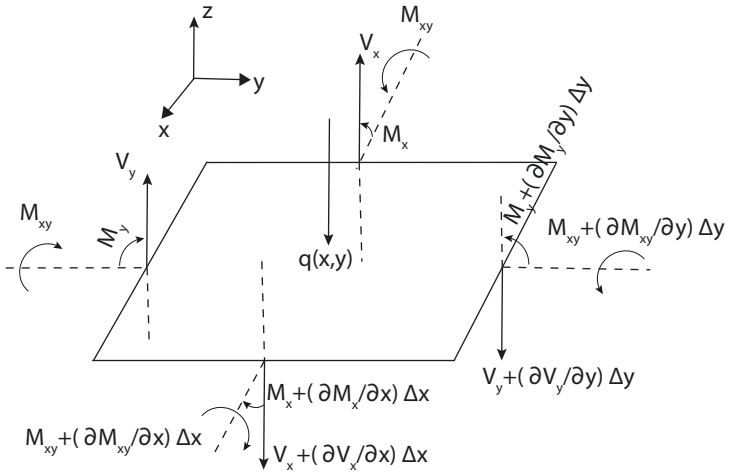

Figure 2.7 Midplane of plate under load q(x,y). The diagram shows the bending moment components and out-of-plane shear force components acting on the four sides of the midplane of plate under the distributed load q(x,y). The force equilibrium in the z direction and bending moment equilibrum gives the plate bending differential equation for a given load q(x,y).

2.4.3 Differential equation for plate bending

The strain, stress components and the stress resultants for the plate discussed in the previous section will now be used to derive the plate bending differential equation for a lateral load (q). Load (q) is the force per unit area or per unit length applied on the plate. Let's consider a plate element with center at (0,0) and with length Δx and Δy. The plate element is subjected to the lateral pressure(q), moments and shear forces. Fig. 2.7 shows the midplane of the plate element under load q and illustrates the stress resultants acting in different direction. These quantities are related through the force equilibrium condition. The lateral load,q(x,y) is in the z direction and is applied to the top surface of plate. Thereby the stress component,σ_{zz} is

$$\sigma_{zz} = \begin{cases} 0 & z = -h/2 \\ -q(x,y) & z = +h/2 \end{cases}$$

where h is the thickness of the plate. By taking the force equilibrium in the z direction, $\sum F_z = 0$ gives

$$\sum F_z = V_y \Delta x - (V_y + \frac{\partial V_y}{\partial y}\Delta y)\Delta x + V_x \Delta y - (V_x + \frac{\partial V_x}{\partial x}\Delta x)\Delta y - q\Delta x \Delta y = 0 \tag{2.75}$$

Thus we get the following condition,

$$\frac{\partial V_x}{\partial x} + \frac{\partial V_y}{\partial y} = -q \tag{2.76}$$

Under equilibrium the moments along x-axis add up to zero, $\sum M_x = 0$. Thus one obtains,

$$\sum M_x = M_{xy}\Delta x - (M_{xy} + \frac{\partial M_{xy}}{\partial y}\Delta y)\Delta x - M_x \Delta y + (M_x + \frac{\partial M_x}{\partial x}\Delta x)\Delta y + (-\Delta x/2)V_x \Delta y - (\Delta x/2)(V_x + \frac{\partial V_x}{\partial x}\Delta x)\Delta y = 0 \tag{2.77}$$

Neglecting the $(\Delta x)^2$ terms in Eq. 2.77 results in

$$V_x = \frac{\partial M_x}{\partial x} - \frac{\partial M_{xy}}{\partial y} \tag{2.78}$$

Similarly, for the moment along y axis, $\sum M_y = 0$ gives

$$V_y = \frac{\partial M_y}{\partial y} - \frac{\partial M_{xy}}{\partial x} \tag{2.79}$$

On combining Eq. 2.78, 2.79 in Eq. 2.76 we get,

$$\frac{\partial^2 M_x}{\partial^2 x} + 2\frac{\partial^2 M_{xy}}{\partial x \partial y} + \frac{\partial^2 M_y}{\partial^2 y} = -q \tag{2.80}$$

We can convert this differential equation in terms of the vertical displacement (w) of the plate using Eq. 2.71 to 2.73,

$$\frac{\partial^4 w}{\partial^4 x} + 2\frac{\partial^4 w}{\partial^2 x \partial^2 y} + \frac{\partial^4 w}{\partial^4 y} = -q/D \tag{2.81}$$

This differential equation is called equation of Sophie Germain who first obtained it in 1815.

2.4.4 Three point bending

Now we consider a problem that is specific to the technique we adopt for straining in this thesis, that is the three point bending case and we assume that the bending is symmetric. One of the main points from the plate theory assumptions we use is $w(x, y, z) = w_0(x, y, 0)$. The opposite edges of the plate along the y direction are simply supported (not fixed) and the edges along the x direction are free. The boundary conditions are as follows:

$$w(-L/2, y) = w(+L/2, y) = 0 \tag{2.82}$$

$$\frac{\partial w}{\partial x}|(0, y) = 0 \tag{2.83}$$

$$\frac{\partial^2 w}{\partial^2 x}|(-L/2, y) = \frac{\partial^2 w}{\partial^2 x}|(+L/2, y) = 0 \tag{2.84}$$

The load is put at two ends of the substrate similar to pulling it down. The center of the substrate is kept fixed against the central wedge. Thus the there is no bending in y direction, therefore the corresponding terms in the plate differential equation (Eq. 2.81) will drop off. Since the problem is symmetric we can solve the differential equation for one half of the substrate either $-L/2 \leq x \leq 0$ or $0 \leq x \leq L/2$ as the bending is symmetric in both the halves. Consider the region $0 \leq x \leq L/2$,

$$\frac{\partial^4 w}{\partial^4 x} = -\frac{f}{2D}\delta(x - L/2) \tag{2.85}$$

where $q = \frac{f}{2}\delta(x - L/2)$, $f = F/b$ is the force (F) acting per unit length along the width (b) of the substrate. On solving this differential equation with the boundary conditions mentioned above we get,

$$w(x) = -\frac{f}{48D}(6x^2 L - 4x^3 - L^3) \tag{2.86}$$

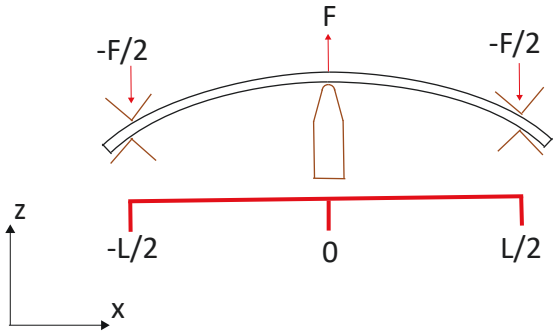

Figure 2.8 Cross section of three point bending. Symmetric three point bending of a plate with free clamping at the two ends. F/2 is the force exerted at the two ends downwards to bend the plate and from the central wedge a reaction force F acts upwards and maintains the vertical force equilibrium. The length of plate between the clamps is L

The maximum deflection is $w_{max} = w(0) = \frac{fL^3}{48D}$. The bending results in an effective tensile strain in the upper surface of the plate as described in Eq. 2.64 for ϵ_{xx}, as the other strain components are zero from the boundary conditions. In Ch. 4 the equations derived in this section will be used to check whether the cubic polynomial solution from plate bending differential equation can fit with the actual bending achieved in the strain setup II. Also the details on how much of the tensile strain on top surface of the plate is transferred to the encapsulated graphene device junction will also be discussed in Ch. 4.

2.5 Graphene, strain and Raman spectroscopy

Strain can modify the graphene lattice as it directly affects the C-C bond and thus has an effect on lattice vibrations or phonon modes. Raman spectroscopy is a vital tool to get information on phonon modes in the system [63] and is used to characterise strain [64]. In the two dimensional material community it is also used as a tool to differentiate among few layers of a given material [65, 66]. In addition to strain, the phonon modes also shows dependance on doping density, edge chirality [52, 67]. In the following more about the phonon modes in graphene will be discussed and how strain can be characterised with Raman spectroscopy.

2.5.1 Raman spectroscopy

Raman spectroscopy is the study of inelastic scattering of photons by electrons and phonons. The laser light of energy, E_l incident on the material excites an electron to another resonant/non-resonant level and the interaction with phonon causes it to lose or gain energy depending on whether the system was initially in ground or excited vibrational state and further recombination of electron and hole gives out the scattered light of energy, E_s. The difference in energy, E_l - E_s corresponds to the phonon mode energy. The Raman spectrum basically shows the intensity of scattered light as a function of E_l - E_s in relative wavenumber (rel.cm^{-1}). The Raman spectrum of graphene has two major peaks, G and 2D peak namely. To understand about the origin of these two peaks in a graphene Raman spectrum, it is necessary to introduce the phonon dispersion of graphene, shown in Fig. 2.9.

2.5.2 Phonon modes and Raman spectrum in Graphene

The graphene unit cell has two atoms, thus 6 different vibrational modes or phonon modes are possible. The phonon modes can be classified as optical (O) and acoustic (A) based on how the atoms in the unit cell oscillate with respect to each other. If the atoms in the unit cell oscillate in the same direction it results in acoustic phonon mode whereas if it is against each other it is optical phonon mode. Then, depending on the directon of vibration of a C atom with respect to the C-C bond direction it can be a transverse (T) or longitudinal (L) phonon mode. The modes are longitudinal if atoms vibrate along the bond direction and transverse when atoms vibrate perpendicular to the bond direction. The vibration can be in-plane (i) or out of plane (o). Thus the phonon dispersion of graphene has 6 branches. The in-plane transverse optical (iTO) and in-plane longitudinal optical (iLO) phonons are responsible for the main Raman peaks, the G and 2D peak in graphene [52, 68].

G peak

The process involved in G peak in graphene Raman spectrum is schematicaly shown in Fig. 2.10(a). It is a first order process with only one phonon involved. The incident photon excites an electron to a virtual state creating an electron-hole pair, the electron is further scattered by iTO or iLO at the Γ point (center of the first Brillouin zone) and then recombines with the hole which results in the emission of a photon with an energy smaller than that of the incident photon. Both iTO and iLO are degenerate at the Γ point. The wavevector of the phonon involved in this process is zero as it happens at the Γ point.

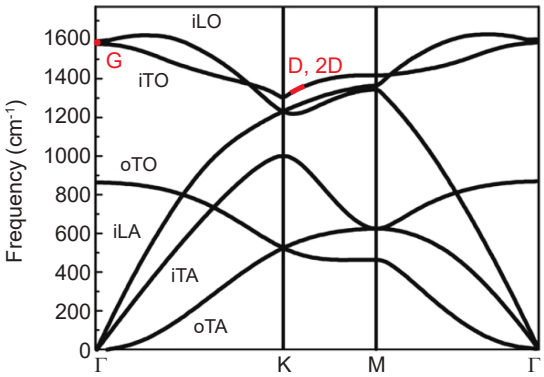

Figure 2.9 Phonon dispersion of graphene. All six phonon branches in graphene are shown. The phonons associated with the G, D and 2D Raman bands are highlighted. Figure adapted from Ref. [69].

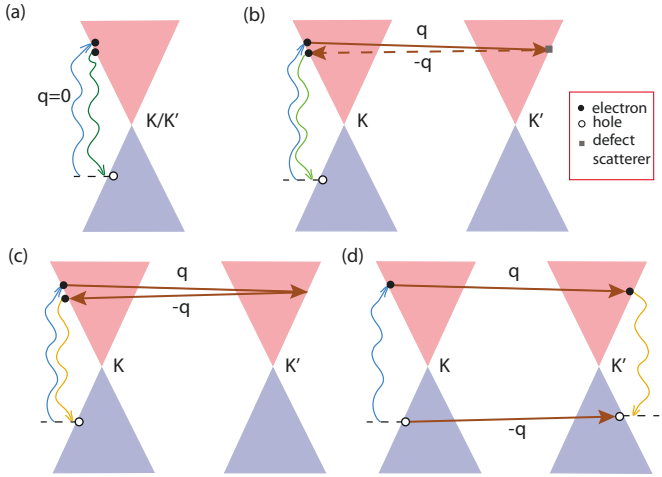

Figure 2.10 Raman scattering process in graphene. **(a)** G band, involving a phonon with almost zero momentum. **(b)** D band, involving one phonon and a defect scattering (horizontal dashed line). **(c)** G' or 2D band originating from a double resonant process with electronic levels. Two phonons are involved.

2D peak

The 2D peak (or G') in Raman spectrum of graphene is a result of second order process as it involves two electron-phonon scattering event. The incident photon excites electrons to a new resonant energy level and creates an electron-hole pair near the K point. Further the iTO phonon scatters the excited electron to the other valley around K' point inelastically. From the momentum conservation, the electron must be scattered back to the initial valley around K and further it recombine with the hole at the K valley. The back scattering of electron is aided by a second iTO phonon. The incident photon and the first phonon scattering (or the scattered photon and the second phonon scattering) are resonant with electronic levels in the graphene, this process is known as double resonant. The shape of 2D peak helps to differentiate between few layer graphene flakes in experiments as shown in Fig. 3.2.

D peak

In addition to the G and 2D (G') peak, the Raman spectrum of graphene shows another peak called D peak. The intensity of this peak is proportional to the defect density in graphene [70, 71]. It is also a second order process but with only one phonon involved [72]. The first half of the process is identical as that for the 2D peak but the second half involves back scattering of electron form K' valley back to K valley which is aided by defects. This results in momentum conservation. The back scattering of electons by defects is elastic. Thus the scattered photon is only red shifted by half as 2D peak.

Raman spectrum of Graphene

The Fig. 2.11 shows a typical Raman spectrum of pristine graphene flake. The D peak is absent which indicates absence of defect. The G peak occurs at $\sim$1580 cm^{-1}, which is independent of the energy of the incident photon. This is because only virtual electron-hole pairs are involved in this process and the involved phonons are always from the Γ point. The intensity of 2D peak is much higher than that of the G peak. The peak position of D and 2D peak can shift with the energy of incident phonon as the process involved is resonant with the energy leves in graphene and also due to the phonon energy dispersion around the K/K' point [73].

2.5.3 Strain characterization

The peak position of the G and 2D peak (ω_G, ω_{2D}) gives the frequency of the phonon mode involved, which is sensitive to strain. Tensile strain softens the bond strength and there by redshift the phonon frequency. In the experiments carried out, graphene/bilayer graphene is uniaxial tensile strained.

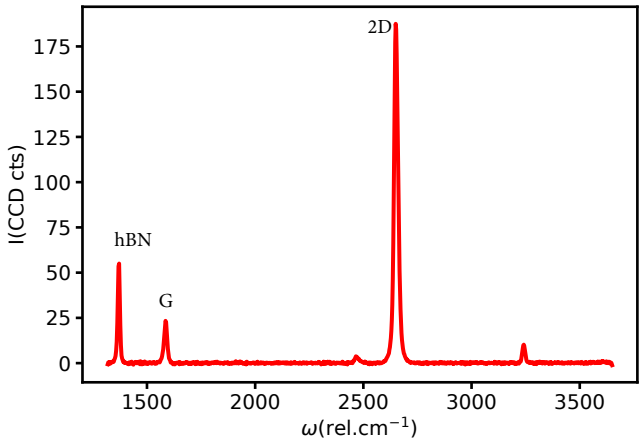

Figure 2.11 Example Raman spectrum of graphene. Raman spectrum of a pristine graphene flake, showing the characteristic G and 2D (G') bands.

The red shift of the 2D peak is used to characterize strain in our experiments. From theory calculations te shift rate of ω_{2D} with strain(ε) is $\frac{\partial\omega_{2D}}{\partial\varepsilon}$ = -54 cm^{-1}/% [74]. So combining the red shift observed in experiment with the shift rate gives the magnitude of strain in the graphene junction.

2.5.4 Strain effects in electronic properties of graphene

In addition to strain affecting the phonon modes in graphene, it can also possibly bring changes in the low energy dispersion of the graphene bandstructure as strain can affect the nearest neighbour hopping [75]. The changes in bandstructure directly affects the electronic properties of graphene. First of all we will derive the relation between bond displacement(u), bond length(δ) and in-plane strain(ϵ). In graphene each C atom has 3 nearest neighbor. Let $\vec{\delta}_j$ be the unstrained position vector of nearest neighbor C atom and $\vec{\delta}'_j$ represents after straining, where j = 1,2,3 and $|\vec{\delta}_j| = a_0$. The displacement vector of the nearest neighbor C atom (considering the central C atom to be fixed) can be written as

$$\vec{u}_j = \vec{\delta}'_j - \vec{\delta}_j \tag{2.87}$$

The bond length change in graphene due to strain can be written as,

$$\Delta\delta_j = |\vec{\delta}'_j| - |\vec{\delta}_j| \approx \vec{u}_j \cdot \frac{\vec{\delta}_j}{a_0}. \tag{2.88}$$

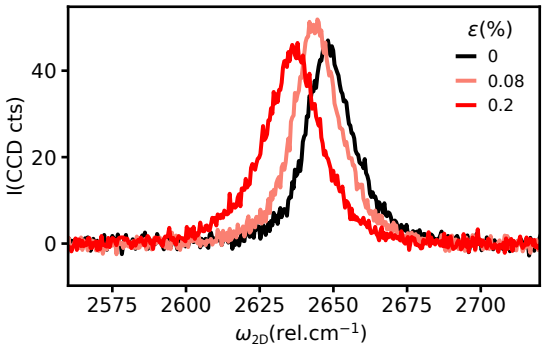

Figure 2.12 2D peak shift of graphene with tensile strain. Raman spectra showing 2D Raman mode intensity(I) versus peak position(ω_{2D}) for tunable tensile strain (ε(%)) of 0, 0.08 and 0.2%. The ω_{2D} red shifts with ε. Tensile strain is estimated using $\frac{\partial\omega_{2D}}{\partial\varepsilon}$ = -54 cm^{-1}/% [74] by extracting change in $\omega_{2D}(\Delta\omega_{2D})$.

Now we consider the whole graphene lattice and in the continuum limit the strain tensor ε can be written from the theory of elasticity with its components(only in-plane strain considered here) given as [62]

$$\varepsilon_{mn} = \frac{1}{2}(\partial_n u_m + \partial_m u_n), \qquad m, n \in \{x, y\}\,. \tag{2.89}$$

So the displacement vector, $\vec{u}_j$ can be approximated as,

$$\vec{u}_j \approx \begin{pmatrix} \varepsilon_{xx} & \varepsilon_{xy} \\ \varepsilon_{yx} & \varepsilon_{yy} \end{pmatrix} \cdot \vec{\delta_j}. \tag{2.90}$$

where $\vec{u}_j$ and $\vec{\delta}_j$ are in-plane vectors.

Changes in bond distance and bond displacements with strain brings changes in the symmetry of crystal lattice as well as in the reciprocal lattice and thereby change the bandstructure. The three major strain effects predicted in theory involves the following [76]:

(a) Shift of Dirac cones in energy space.
(b) Shift of Dirac cones in k space.
(c) change in the slope of linear low energy dispersion.

Each of the above mentioned effect will be discussed in the following.

Scalar potential

The shift of the positions of atoms due to strain changes the on-site energy of the p_z orbitals. This leads to an effective shift in the energy of the graphene lattice. The effect can be captured by the addition of a scalar potential term to the Dirac equation. The effect can be visualised as the shift of Dirac cones in energy axis. The scalar potential depends on the strain as follows,

$$V(x,y) = s_0(\varepsilon_{xx} + \varepsilon_{yy}) \tag{2.91}$$

where s_0 is the scalar potential constant. The value for $s_0(\sim 2.5$ eV) is estimated from the workfunction studies in graphene with strain [34]. More details on scalar potential in graphene will be discussed in Ch. 6.

Fermi velocity anisotropy

The slope of the low energy dispersion in graphene around the K or K' point is proportional to Fermi velocity (v_f) of the charge carriers and is a constant,$v_f = 3\gamma_0 a_0/2\hbar$. The hopping term t depends on bond distance [36] as

$$t_j = \gamma_0 e^{-\beta(\frac{|(\bar{I}+\bar{\varepsilon}).\vec{a}_0|}{a_0} - 1)}, \quad j = 1,2,3 \tag{2.92}$$

$\vec{a}_0$ is the undeformed nearest neighbour vector , $\bar{\varepsilon}$ is the in-plane strain tensor,$\bar{\boldsymbol{I}}$ is the 2×2 identity matrix described in Eq. 2.90

$$\vec{a}_j = (1 + \bar{\varepsilon})\vec{a}_0 \tag{2.93}$$

where j represents the nearest neigbour, γ_0 is the undeformed in-plane hopping energy (as described in Eq. 2.16), $\beta = \partial \log t/\partial \log a \mid_{a=a_0} \approx 2-3$ [77] is the modulation factor for the strained hopping energy, $\vec{a}_j$ is the deformed nearest neighbour vector. Fermi velocity v_f is dependent on strain (ε) through the hopping (t) term and the nearest neighbour distance (a_0). Considering the in-plane strain, v_f can be generalised as [78],

$$\bar{v} = v_{f0}\left(\bar{\boldsymbol{I}} + (1-\beta)\bar{\varepsilon}\right), \tag{2.94}$$

The Fermi velocity becomes anisotropic when the graphene lattice is strained. For example in the case of uniaxial tensile strain along x direction, $\varepsilon_{xx} = \varepsilon$, $\varepsilon_{xy} = 0$, $\varepsilon_{yy} = -\nu\epsilon$, where ν is the Poisson ratio[79, 80]. This gives the following,

$$v_{fxx} = v_{f0}(1 + (1-\beta)\epsilon) \tag{2.95}$$

$$v_{fyy} = v_{f0}(1 - \nu(1-\beta)\epsilon) \tag{2.96}$$

Therefore the Fermi veocity in the direction of tensile strain will be less than in the direction perpendicular to it.

Magnetic vector potential

The distortion of graphene lattice with strain in real space cause displacement of the bonds which will also distort the reciprocal space lattice [81, 82]. The Dirac cones position in k space will shift from the K, K' points under strain [78]. As mentioned above the hopping term changes with strain,

$$t_j = t_0(1 - \beta\frac{\Delta\delta_j}{a_0}) \tag{2.97}$$

where $\frac{\Delta\delta_j}{a_0} = \frac{|(\bar{I}+\bar{\varepsilon}).\vec{a}_0|}{a_0} - 1$,from the previous part. Therefore straining the graphene lattice changes the hopping term t_j(j = 1,2,3) different for neighbouring C atoms. The tight binding model discussed in Subsec. 2.1.2 for graphene can be solved with the new hopping terms t_j's. The off diagonal terms of the Hamiltonian in Eq. 2.7 ($\gamma_0\alpha(k)$) is replaced with new term,

$$H_{AB} = H^*_{BA} = \sum_j t_j e^{i\vec{k}\cdot\vec{\delta'}_j} \tag{2.98}$$

where $\vec{\delta'}_j = (1+\epsilon)\vec{\delta}_j$.

$$H = \gamma_0 \cdot \begin{pmatrix} 0 & \tilde{\alpha}(\vec{k}) \\ \tilde{\alpha}(\vec{k})^* & 0 \end{pmatrix}. \tag{2.99}$$

where

$$\tilde{\alpha}(\vec{k}) = \sum_j (1 + \delta t_j + i\vec{k}\cdot\varepsilon\cdot\vec{d}_j)e^{i\vec{k}\cdot\vec{d}_j} \qquad and \qquad \delta t_j \equiv (t_j - \gamma_0)/\gamma_0. \tag{2.100}$$

In Eq. 1.83 we see that δt_j is proportional to first order in strain as the term $\frac{\Delta\delta_j}{a_0}$ describes the strain in the bond to jth nearest neighbour. The δt_j term originates from the expansion of t_j and the $i\vec{k}\cdot\varepsilon\cdot\vec{\delta}_j$ term results from the expansion of $e^{i\vec{k}\cdot\vec{\delta'}_j}$. Both the terms are first order in strain (ε) and higher order ε terms are neglected. The effect of these first order terms in ε can be effectively put into the vector $\vec{A}_i$. The modified dispersion relation of graphene is,

$$\tilde{H}_{\pm K_i} \approx \hbar v_f \hat{\sigma}(\vec{q} \pm \frac{e}{\hbar}\vec{A}_i), \tag{2.101}$$

where i = 1,2,3 represents the three K and K' point in the k space as these are not degenerate anymore in graphene lattice under strain.

$$\vec{A} = \frac{\hbar\beta}{2ea_0}\begin{pmatrix} \epsilon_{xx} - \epsilon_{yy} \\ -2\epsilon_{xy} \end{pmatrix}. \tag{2.102}$$

The $\pm$ represents the K and K' valley. The vector $\vec{A}_i$ resembles a magnetic vector potential and is called pseudo vector potential. The $\pm$ infront of $\vec{A}_i$ shows it is asymmetric in valley and is due to the constraint of time reversal symmetry [37, 83].

3 Experimental methods

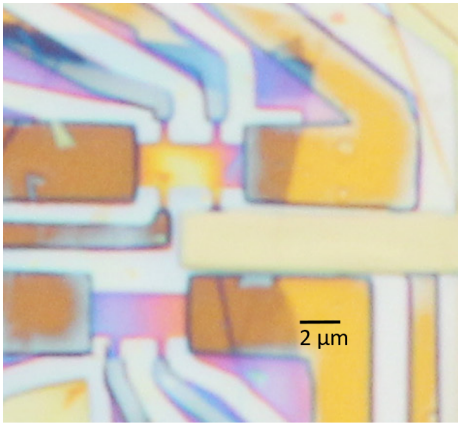

This chapter describes the experimental methods employed in this thesis. First, the fabrication techniques are introduced, followed by bending setup for room temperature Raman scanning microscopy for strain characterizaton and low temperature bending setup used for charge transport measurement under tensile strain are described. Furthermore, the way to achieve electrical connection from the dipstick to the fabricated sample and the basic concepts of the low temperature transport measurements are described in the final section[1].

[1] An optical image of dual(top and bottom) gated bilayer gaphene hall bar.

3.1 Fabrication

The making of device for the strain transport study involves several preparation steps at different levels starting from the polishing of substrate to the final step of mounting device in the strain setup. This section will focus on the steps involved in the fabrication of device junctions studied in this thesis. First, exfoliate the required 2D materials : graphene and hBN, followed by encapsulation of graphene with hBN , and finally edge contact graphene and shaping of the device junction.

Exfoliation and encapsulation are key steps in making high quality devices. Encapsulating graphene in hBN proved to be better in terms of mobility [41, 42],less residual doping compared to the the bare graphene flake on Si/SiO_2 substrate and also even comparable to suspended graphene junctions [84]. Fabrication of a high quality stack needs to be combined with a good contacting technique which ensures low contact resistance. The technique of edge contacting the graphene [33] stands ahead in terms of offering low contact resistance compared to surface contacts [85].

The process of edge contacting the graphene followed by shaping the device junction for a well defined geometry involves the use of electrom beam lithography,reactive ion etching(RIE) and depositing metal with e-beam evaporation. The recipes involved in these steps will be discussed in appendix 1.

3.1.1 Exfoliation

The research growth in 2D materials field is boosted by mechanical exfoliation technique with graphene being the first 2D material to be exfoliated [86]. This technique results in producing clean flakes directly from the crystal sources without introducing any further chemical steps. Eventhough the yield in obtaining graphene of reasonable size $\sim 15\ \mu m \times 15\ \mu m$ is average,the technique is faster than other crystal growth techniques and produces material with low defect concentration [87].

The technique involves using sticky tape[2] to exfoliate flakes from the crystals of the required materials. The steps in the exfoliation process involves putting the bulk crystal in contact with the tape followed by repetitive cleaving of crystal into thinner flakes and at this stage transfer the flakes onto the SiO_2/Si substrate from the tape. Even though no chemical steps are involved in the technique one should choose a tape that will leave less residues on the substrate after exfoliation. This is to ensure lesser probability of these residues to end up on the device junction after pick up and stacking process.

[2]For example, SPV 224P, Nitto Europe NV

The crystal sources for graphene and hBN are the following : (a) natural graphite[3] (b) high quality hBN crystals grown by K. Watanabe and T. Tanaguchi [88]. Examples of exfoliated graphene and hBN flakes are shown in Fig. 3.1. Optical microscope images are used to identify the exfoliated flakes on SiO_2/Si (∼285 nm thick SiO_2) of desired thickness from the optical contrast. Single layer graphene gives the least contrast under optical microscope compared to the bilayer and its multilayers [89] which can be seen in Fig. 3.1(a). In addition to the optical contrast, Raman microscopy can clearly distinguish graphene from its multilayer from the peculiar shape of the 2D peak in the Raman spectrum [65]. The Raman spectrum of graphene will be discussed in Ch. 2. For hBN, we usually choose the flakes with a thickness in the range ∼20 nm - ∼60 nm, which can be recognized by the color under optical microscope, see for example the image of flake shown in Fig. 3.1(b) with 100x objective. The bright field and dark field optical images at 100x is also used to screen out flakes with tape residues, cracks or folds.

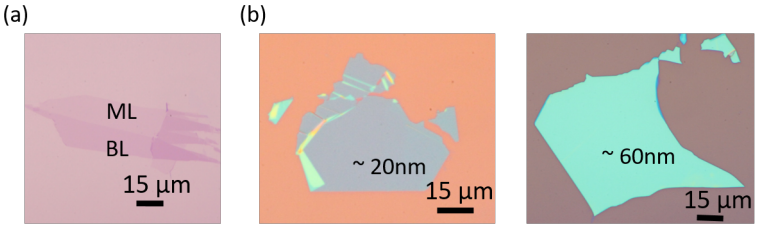

Figure 3.1 Graphene and hBN exfoliation. **(a)** Exfoliated graphene flakes on a Si wafer with ∼285 nm of SiO_2. Monolayer (ML) and bilayer (BL) graphene on a single flake. **(b)** Exfoliated hBN flakes. The flake on left side is around 20 nm thick and is ideal as the top hBN for the stack . The flake on right is 60 nm thick and is good as a bottom hBN for the stack, also act as the back gate insulator for graphene device junctions.

[3] Obtained from NGS Trading & Consulting GmbH.

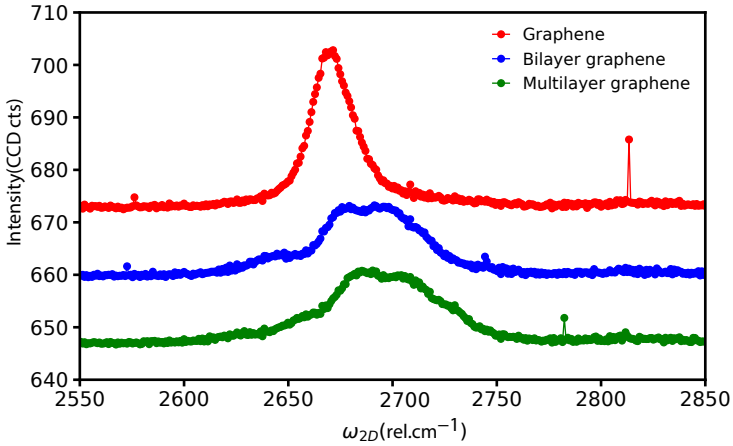

Figure 3.2 Raman spectrum of graphene, bilayer and multilayer graphene. Intensity (in CCD counts) versus 2D Raman peak position(ω_{2D}) of graphene(red), bilayer graphene(blue) and multilayer graphene(green). Raman spectroscopy can be a quick tool to identify few layers of graphene especially between monolayer and bilayer graphene as clearly the shape of 2D Raman peak is different.

3.1.2 Encapsulation

After identifying the required flakes, it is followed by the assembly of heterostructure using dry transfer technique. These steps make it possible to encapsulate graphene in hBN. In device fabrication for charge carrier transport, encapsulation of graphene in hBN serves the dual purpose of high charge carrier mobility as well as a gate dielectric to tune the charge carrier density [42]

The main steps involved in encapsulation are shown schematically in Fig. 3.4, where the pick-up technique introduced by Wang et al. and Zomer et al. [41] is followed. The steps involved in encapsulation will be briefly described in the following.

PDMS/PC stamp preparation: The first step is preparation of a polycarbonate (PC) film on a glass slide using the premade PC solution. The PC solution is prepared by dissolving PC pellets in chloroform with an overnight stirring. The recipe for preparing PC solution is discussed in appendix 1. Its followed by transferring the PC membrane using a Scotch tape with a window of size 0.5 cm by 0.5cm opened at its center. Further a pdms piece roughly of size 0.25 cm by 0.25 cm is placed on other glass slide and the scotch tape with PC membrane is put on top of this glass slide such that the PC film passes smoothly (without any airbubbles) over the pdms piece and then the two sides are fixed additionally to the glass slide with the help of scotch tape. The pdms piece is cleaned initially with sonication in isopropyl alcohol (IPA) before using it.

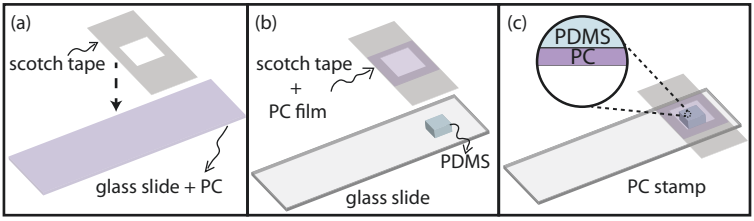

Figure 3.3 Steps in PC stamp preparation (a). First step of transferring the PC film prepared on glass slide to the scotch tape with a window opened. **(b)** Another glass slide with a clean pdms piece on it. **(c)** The PC film is placed over the pdms piece and the scotch tape adhere to the glass slide forming the PC stamp.

Stacking : The process of stacking the 2D materials is done with the help

of transfer setup. The transfer setup consists of a bottom stage on to which the exfoliated substrate is mounted and a top stage to mount the PDMS/PC stamp. The bottom stage is movable in x,y direction whereas top stage is movable in x,y,z direction. The bottom stage also has roll and pitch degree of freedom. These two parameters are used to tilt the bottom stage relative to the top translation stage, so that the PC film can touch the wafer gradually. A clean area on the PC film of the stamp is selected with optical microscope for the stacking process. The details of stacking process will be discussed for the pick up of graphene which is in general same for all the 2D materials. First of all the top hBN is picked from the substrate with the PDMS/PC stamp,further used for pick up of graphene. The graphene flake is now alligned such that it will be almost fully covered by top hBN. The stamp is lowered until it touches the wafer at one corner, see Fig. 3.4(c1) and a contact interface of PC film of the stamp will be visible. The contact interface is slowly moved forward by further lowering the stamp carefully until top hBN is just next to the graphene flake. At this point the bottom stage is heated to 80 °C from room temperature, leading to a thermal expansion of the PC film, which moves the interface across the graphene flake making the top hBN fully in contact with the graphene, see Fig. 3.4(c2). Now the interface which is over the location of graphene is kept at a fixed position by slowly retracting the stamp until the temperature reaches 80 °C. The heater is switched off at 80 °C and the substrate starts to cool down. Now the PC film slowly start to shrink and retract automatically, as shown in Fig. 3.4(c3). The flake will be picked up during retraction as graphene shows better adhesion to hBN than to SiO_2 due to stronger van der Waals interaction. That is also the mechanism when picking up the top hBN layer in the first step where hBN exhibits better adhesion to PC film than to SiO_2 at 80 °C. The bottom hBN is further picked with the above mentioned procedure,see Fig. 3.4(c). The bottom hBN is alligned such that it fully covers the graphene. Thus the graphene is sandwiched between top and bottom hBN. The stack on the stamp needs to be transferred further to the target substrate as the next step in device fabrication.

Transfer of stack : The target substrate is fixed in the bottom stage and the stamp with assembled hBN/graphene/hBN stack is brought close to the desired region on substrate with the help of top translation stage of transfer setup. The stamp is brought in contact with target substrate and the heater is switched on to 80 °C. As the PC interface goes over the stack, the heater is set to 170 °C. The target substrate is heated and the PC film detaches from the PDMS stamp, as shown in Fig. 3.4(d). At this temperature, the PC film adhere better to the substrate than to the PDMS stamp. In the end, the PC is dissolved in chloroform, leaving the assembled stack on the substrate.

Then the stack is characterized with AFM to locate bubble-free regions and

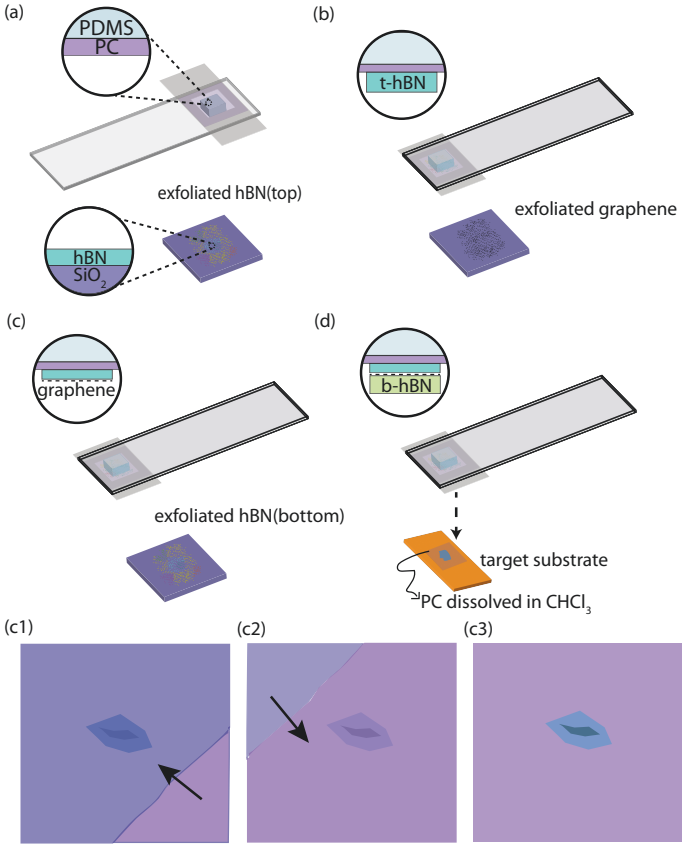

Figure 3.4 Steps in encapsulation and transfer of stack. **(a)** The PDMS/PC stamp prepared is used to pick up the identified top hBN. **(b)** The PDMS/PC stamp with top hBN is further used to pick up the graphene. The details of the picking up of graphene is shown in c1,c2,c3. First, the PC interface upon contact with substrate on heating will move and spread over the substrate as shown in c1. Further after that when heating is stopped by decreasing the temperature to room temperature PC film will shrink and the interface will now move in the opposite direction as shown in c2. In this process graphene upon contacted with top hBN on the PDMS/PC stamp pick up the graphene due to its better adhesion to van der Waals material over the SiO_2/Si substrate. **(c)** Now the PDMS/PC stamp with top hBN and graphene is used to pick up bottom hBN following similar procedures shown in c1,c2,c3 and results in graphene encapsulation. **(d)** Transfer of encapsulated graphene stack to the target substrate folowed by removal of PC film by dissolving it in $CHCl_3/CH_2Cl_2$. The figure is adapted from Ref. [90].

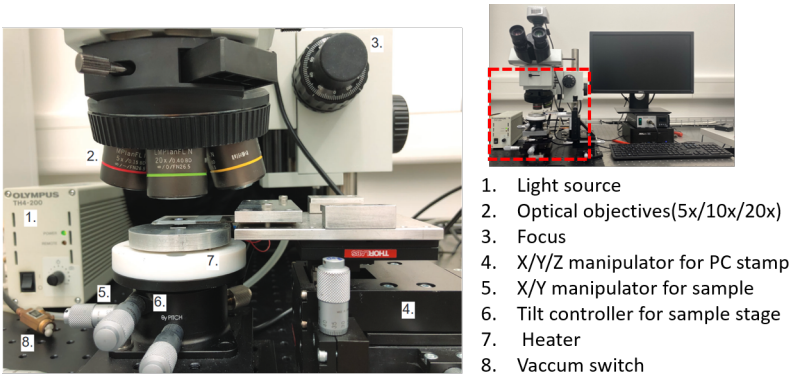

Figure 3.5 Transfer setup for stacking. The image on right side shows the overview of the whole stacking setup along with the computer to which camera is connected to position the sample , PC stamp , to carryout the pick up and stacking process. The image on left is zoom in of the red dotted box in the image on right. It shows the PC stamp under microscope for the pickup process and other components of the stacking setup is labeled.

also to determine the thickness of top and bottom hBN layers for designing the device junctions. Later, standard nanofabrication techniques, including e-beam lithography, reactive ion etching and metallization processes (electron beam evaporation), are used to make electric contacts and shape the stack into the desired device geometry. Details of the recipes in nanofabrication are given in the appendix. 1.

3.1.3 Top gate

For strain transport studies on bilayer graphene(BLG) top gate was implemented so that charge carrier density and electric field can be independently tuned [48]. Two methods were tried , (a) Method 1 : Place an additional graphite layer in the top at the end of normal stacking procedure. (b)Method 2 : Transfer an additional graphite/hBN stack on top of the edge contacted bilayer graphene device junction. Fig. 3.6 illustrates top gate fabricated device junctions for the two possibilities mentioned. The same stacking procedures as mentioned in subsec. 3.1.2 were followed for both the methods.

Method 1
Steps involved are :
1. Prepare the hBN/BLG/hBN stack and place it on the target substrate

followed by removal of PC film.
2. Pick up the graphite with the PDMS/PC stamp.
3. Place the graphite on hBN/BLG/hBN stack with the help of transfer setup and followed by removal of PC film.
4. Etching of graphite with O_2 plasma to shape the top gate. This step involves e-beam lithogrpahy to put the mask for shaping the top gate.
5. Edge contacting BLG and shaping of device junction. This step involves e-beam lithography, e-beam evaporation of Cr/Au followed by lift off for the edge contacts. The edge contacts are designed to be slightly away from the top gate structure. After edge contacting,the device junction is shaped with help of RIE.
6. Depositing Cr/Au on the top graphite to connect the top gate to the outter contact pad for electrical connection to supply gate voltage. This step involves e-beam lithography, e-beam evaporation of Cr/Au followed by lift off.

Method 2
Steps involved are :
1. Fabricate hBN/BLG/hBN stack completely including edge contacting the BLG and shaping of the device junction.
2. Preparing a new stack of graphite on hBN.
3. Placing the new stack prepared in step2 on top of the fabricated hBN/BLG/hBN device junction with the help of transfer setup. It is followed by removal of PC film.
4. Depositing Cr/Au on the top graphite to connect the top gate to the outter contact pad for electrical connection to supply gate voltage. This step involves e-beam lithography, e-beam evaporation of Cr/Au followed by lift off.

Method 1 should ideally give the best top gate as it would be flat giving a uniform top gating on the sample. But the gate leak was an issue in two such fabricated devices from method 1. The device that worked for measurements came out from method 2 but the top gate graphite will not be flat near the edge contact regions as gold deposited can be slightly higher than the etched depth of the stack for edge contacting. But this issue was considered while fabricating,so the amount of gold deposited is around as high as the etch depth to minimise the issue.

3.2 Bending setup

The devices are fabricated on flexible substrate. The graphene in the device junction is uniaxially strained with the three point bending setup which bends the substrate. The thesis consists of experiments run with two different bending setups. In this section, first the preparation of flexible substrate will be

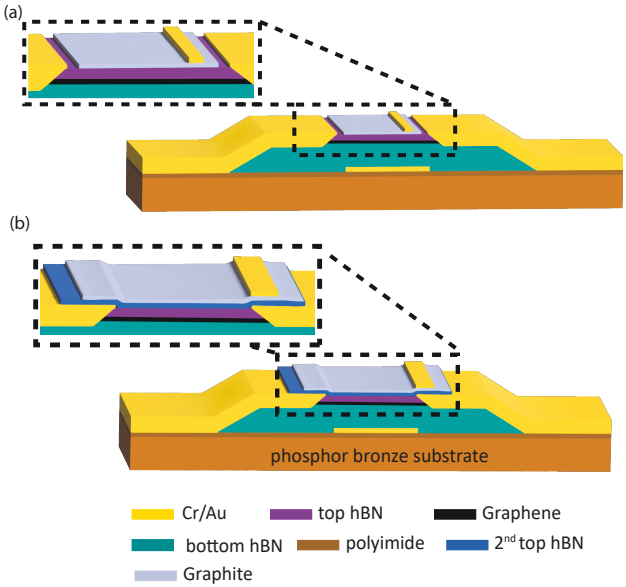

Figure 3.6 Top gate fabrication on hBN/BLG/hBN stacks (a) An additional top graphite layer picked up during the stacking procedure which will act as top gate with top hBN as the gate dielectric. (b) hBN/BLG/hBN stack fabricated completely including the process of edge contacting the graphene and shaping of the device junction. Its followed by another step of placing a two layer stack of hBN and graphite on top of the device junction.

introduced, followed by the details of initial bending setup(Strain setup I) designed for low temperature transport measurements and for measuring raman spectra to characterize strain. Strain setup I is designed and used for quantum transport experiments in graphene under strain during the Phd work of Lujun Wang [91]. Also transport measurements need sucessfull electrical connection to the device junction and how its implemented in the strain transport experiments in this thesis will be briefly described. The newly designed bending setup(Strain setup II) and its specialities will be discussed in detail in Ch. 4.

3.2.1 Flexible substrate preparation

The flexible substrate used for fabrication is 0.3 mm thick phosphor bronze plate[4] in strain stetup I 3.2.2. The commercially available phosphor bronze plate are not flat enough for the nanofabrication,the substrate roughness is shown in Fig. 3.7. Polishing helps to make the substrate flat enough on a length scale of 20 μm,enough for the device junction size. Upon polishing the flatness becomes comparable to the Si wafers. The big plate piece is cut into several 5 cm $\times$ 5 cm plate pieces and is further polished with the help of a lapping machine.

For electrical insulation,thick layer($\sim$5 μm) of polyimide[5](PI) is spin coated on the polished plate. Further on the plate is cut into smaller pieces with dimensions of 24 mm $\times$ 9.5 mm with the help of diamond wire saw. In order to protect the PI surface from the metal fragments and particles produced during sawing, the substrates are coated with PMMA layer. After the plate is sucessfully cut, the PMMA layer is removed with acetone, isopropyl alcohol wash and standard nanofabrication techniques are further used to pre-fabricate the base structure for the device. The base structure includes the bottom gate with markers,outter contact pads and the metallic leads to the contact pads. The bottom gate has a varying width of 10 μm to 30 μm for different size of flakes. After all these processes the preparation of substrate is complete and can be further used for the transfer of stack to fabricate the devices.

3.2.2 Strain setup I

The setup bends the flexible phosphor bronze substrate about three points. The three point bending is inspired from the break junction technique. [3–6]. The metallic leads including the contact pads are fixed to the top PI layer on the substrate and the encapsulated graphene device junction located at the centre of substrate is edge contacted. Bending the substrate can uniaxially tensile strain the edge contacted graphene, will be discussed in Ch. 8. The

[4] CuSn6, häuselmann metall GmbH
[5] PI2610, HD MicroSystems GmbH

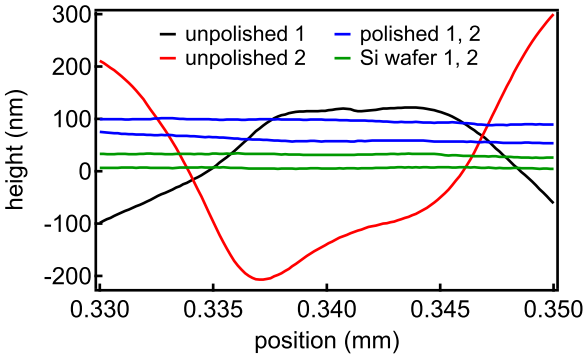

Figure 3.7 Surface roughness. The height profiles of PI surface on unpolished bronze plates (black and red) and on polished bronze plates (blue) are plotted for a 20 μm distance. For reference, the height profiles on the surface of Si wafers (green) are also plotted. In this length scale, the polished surface is almost as flat as the Si wafer. The curves are shifted in y-direction for clarity. The height profile is measured using profilometer

substrate is mounted between two counter supports and a central wedge as shown schematically in Fig. 3.8. The strain characterisation and low temperature strain transport measurements in strain setup I are carried out in two different three-point bending setups shown in Fig. 3.9 and 3.10, which will be briefly described in the next section.

Raman bending setup: The central wedge of the three-point bending setup is kept fixed whereas the two counter support at the two edges of the substrate where it is freely clamped is pulled down with the bending. Thus the center part of substrate is kept fixed to keep it at focus of the microscope even after bending. This bending setup can be mounted on the sample stage of room temperature Raman microscope,as shown in Fig. 3.9. The sample stage is piezoelectric and thus its movable in x,y,z direction. The displacement Δz of the counter support is controlled by the long screw sticking out which controls the bending of substrate. The long screw is connected to a gear system and the reduction effect of it is such that one full rotation of the long screw corresponds to a displacement $\Delta z \approx 20\,\mu$m, giving a very fine control of the bending of substrate and thereby the strain in graphene. The piezoelectric stage makes it possible to get spatially resolved Raman maps over the device junction,which is important for characterizing strain over the whole device area. The room temeperature Raman microscope used is confocal Raman sys-

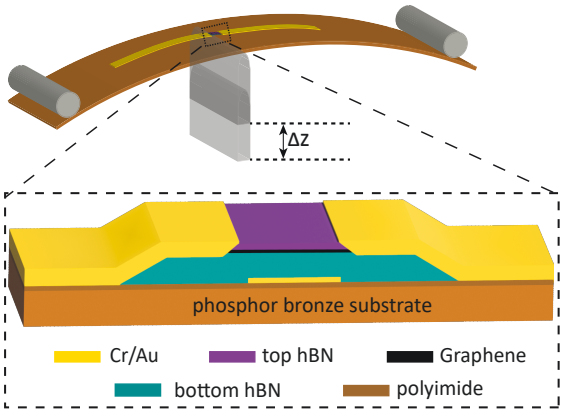

Figure 3.8 Schematic of three point bending. The wedge pushing at the center of substrate with the two ends of the substrate freely clamped by the counter support. The zoom in at the center of substrate shows schematic of a edge contacted device junction of hBN encapsulated graphene. The material of flexible substrate used is phosphor bronze and it is coated with an insulation layer of polyimide.

tem WiTec alpha300. Green laser of wavelength 532 nm, laser power of 1 mW and 600 grooves/mm as the grating of the spectrometer were used for obtaining the Raman maps. The laser spot size is around 500 nm.

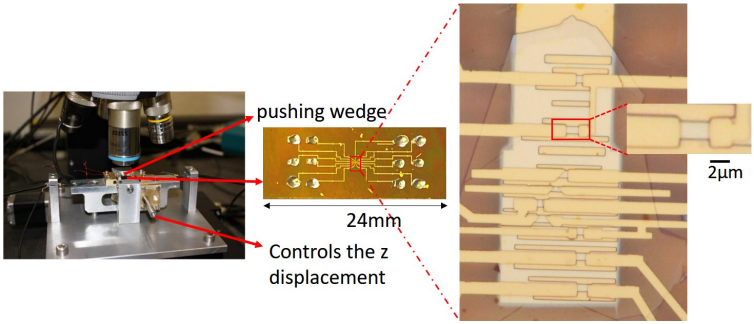

Figure 3.9 Raman bending setup. Room temperature bending setup mounted under the Raman microscope. A typical prepared flexible substrate with metallic leads and contact pads are prefabricated before transfer of the encapsulated stack on the central gate structure. The zoom in on the right side shows the gate structure in the center and the metallic leads to the encapsulated graphene device junctions. Also indium pieces are pressed on to the contact pads on the substrate for further electrical clamping for making electrical connection to cryostat, will be discussed in subsec. 3.2.3.

Low temperature bending setup: The sample is inserted between two fixed counter supports and a pushing central wedge. The central wedge is connected to a controlling knob at the top of dipstick with a rotating rod connected to a differential screw. The wedge pushes the center part of the substrate against the two counter supports at the two edges of substrate. The differential screw makes fine control over substrate bending where one full rotation of control knob corresponds to a displacement of $\Delta z \approx 100\,\mu$m. The base temperature of setup is 4.2 K. The dipstick insert with the low temperature bending setup, in Fig. 3.10(a) is enclosed with a metallic tube. Its then pumped to vaccum and is further filled with a little amount of He exchange gas for thermalisation before inserting it into the liquid ^{4}He bath in cryostat. The cryostat is equipped with superconducting magnet with limits up to +/- 9 T out of plane field.

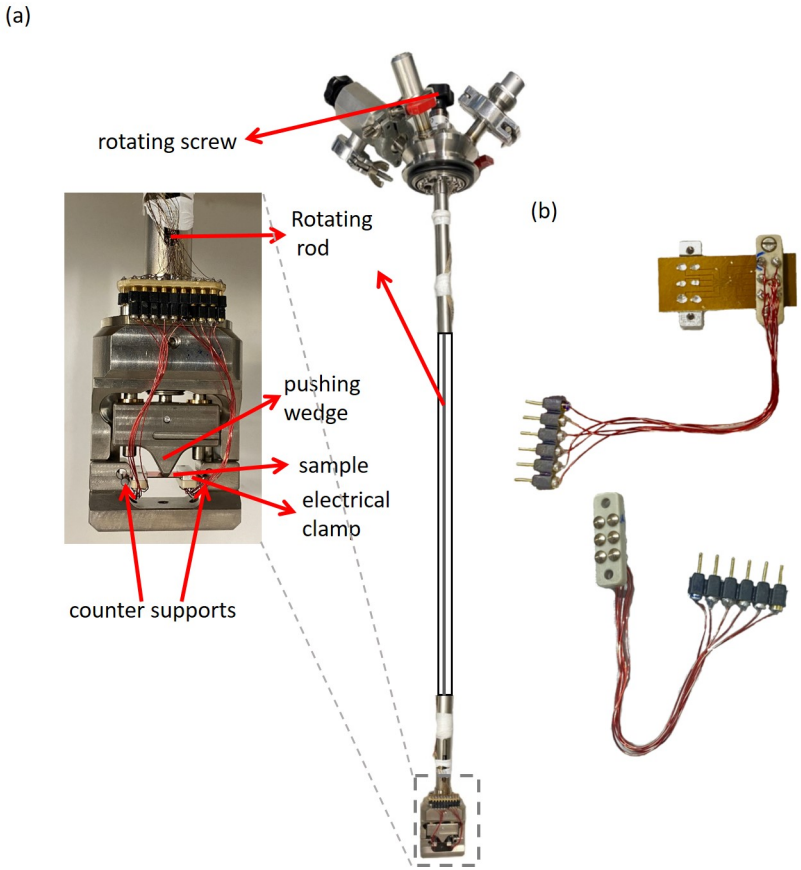

Figure 3.10 Cryogenic strain setup I. (a) Home-built insert for studying strain effects in transport measurements. The inset shows the three-point bending setup. **(b)** electrical clamping technique : first indium pieces are placed over the nanofabricated gold contact pads on substrate and then pressed by screwing the electrical clamp with pins to its counterpart.

3.2.3 Electrical connection and electrical measurement setup

Usually the electrical connection to the devices on SiO_2/Si substrate is carried out through wire bonding on the bonding pads. But unfortunately the wire bonding technique will not work on the bonding pads which are on top of the PI layer of the flexible substrate for strain transport measurement. The PI layer is soft compared to SiO_2 and the bonding pads peels of the substrate when the wire bonding technique is tried. So it is a very important step to develop a technique to contact the fabricated device for strain transport measurement as it should also be compatible and reliable with the low temperature bending in the cryostat.

Electrical connection : Electrical clamps are designed which can be connected to the nanofabricated contact pads. The clamping technique is shown in Fig. 3.10(b). First,small indium pieces of diameter 1-2 mm and thickness of 0.5 mm, are cut from indium wire. The indium pieces are placed on top of the nanofabricated contact pads and then the electrical clamp is pressed on to the indium pieces. The clamp is fixed by screwing to the counter part of it. The clamp itself is connected to electrical pins through copper wire. These electrical pins makes the connection to the electrical lines in the dipstick and from there it further gets connected to the measurement electronics via a breakout box. There are 12 contacts to the sample including the bottom gate.

Electrical measurement : The measurements in the thesis were carried out with the new turning knob of strain. The differential conductance measurements are carried out with standard low-frequency lock in[6] techniques. For the voltage-biased differential conductance measurement, the I/V converter used is SP983c, Basel Precision Instruments. For the current biased differential conductance measurement, the differential amplifier used is SP100 from Basel Precision Instruments. were used. For the back gate or top gate of the device, the DC voltage source used is SP927 DAC (Basel Precision Instruments)[7]. All the measurement instruments were communicated and controlled through RS232 or GPIB interfaces with Qcodes based on Python.

[6] Standford SR830 lock-in amplifier.
[7] Designed and made by the Electronics Lab at the Department of Physics, University of Basel

4 Strain setup II : strain setup with combination of optics and electrical transport

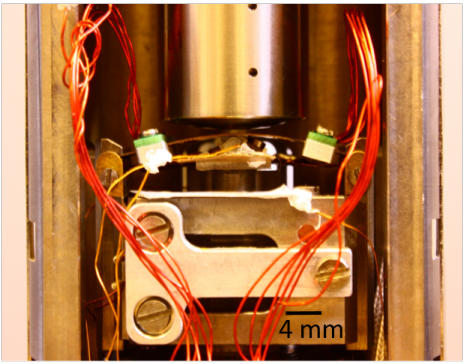

This chapter decribes the design and integration of strain setup to the attoDRY2100[1] cryostat with a base temperature of 1.6 K. It is specially designed for low temperature Raman scanning microscopy. The first two sections briefly describes about the cryostat and optical setup in the system. The next section discusses about the newly designed strain setup[2] (strain seup II) and the mechanism implemented for bending the susbtrate. The technique of electrical connection via clamping to the sample in this system is further discussed followed by a section on shielding the electrical lines to sample from the high voltage lines to the piezo walkers in the strain setup to avoid damage. The next section emphasizes the technique implemented to read out the distance moved by piezo walkers to bend the substrate using a capacitor sensor in the strain setup. An estimate for the tensile strain on the top surface of substrate is further carried out using the bending profile of the substrate and is compared with the strain generated in graphene device.

[1] a product of attocube.
[2] Photograph of newly designed strain setup integrated to atooDRY2100

4.1 Introduction

Several techniques are implemented to strain 2D materials. The difference in thermal expansion rates of the substrate and the material is used to induce strain [22]. The other type includes pre-patterned substrates, where material deposited on such substrates is strained spatially according to the surface profile of the substrate [23]. Suspended samples can be strained with comb-drive actuator method [26] or by using AFM tip [92] to press on is the other way to strain 2D materials. Straining using flexible substrates is another category where material transferred on the substrate due to its adhesion will get stretched or compressed depending on the way substrate is bend [93]. Technique that offers reliable control on strain is ideal for studying the effects of strain on charge carrier transport. The three point bending technique introduced in Ch. 3 generates an average strain in the device junction proportional to the distance the substrate is pushed by the wedge to bend [25].

This chapter describes the design and integration of a new strain setup to the attoDRY2100[3] cryostat based on three point bending technique. The system is unique in combining optics and charge carrier transport with strain as a new tuning knob at cryogenic temperature.

4.2 Attodry2100 dry fridge

This section gives a brief description to the attocube system for low temperature Raman microscopy. The new strain setup will be integrated to this system to combine strain engineering with optics at cryogenic temperature.

attoDRY2100 is a dry fridge with base temperature of 1.6 K. It is equipped with a confocal Raman scanning microscope and a magnet which can deliver out of plane magnetic fields up to ± 9 T. The Raman microscopy is a tool for strain characterization as discussed in subsec. 2.5.3. The objective lens for confocal Raman microscopy in the system is specially designed for low temperatures, also withstands warm up and cool down cycles in temperature carried out in the cryostat. The setup has two sets of piezo units : (a) piezo scanners x,y,z (b) positioner piezo x,y,z. The positioner piezo x,y is used for the coarse potioning of the sample in the x,y direction and the z positioner piezo unit is used for focussing of the sample and the laser spot. The scanner piezo units are used to do the Raman mapping spatially of the sample region in the substrate. The piezo units in the setup are illustrated in a later section in the chapter. The low temperature setup is combined with the possibility to do transport and optical experiments, in addition the strain setup is integrated

[3] a product of attocube.

to it. In the coming sections details on the optical system and the designed strain setup will be discussed in more detail.

4.3 Optical part of setup

The optical components involved in the confocal Raman microscope will be discussed in this section. The setup is equipped with red laser source of wavelength 632.8 nm. The optical head, shown in Fig. 4.1(a) at the top of the microscope stick, act as an intermediate channel to send in and collect the laser signal reflected from the sample in the cryostat. The optical head consists of four layers:

a) **Excitation layer** : Laser light from the source enters the optical head in the excitation layer through optical fibre. Further it passes through a laser clean up filter so that the laser light is as narrow in width for the specified wavelength. The optical path of the laser then involves reflection from the two mirrors arranged at an angle one after the other and guide the laser light to the dichroic beam splitter at the top right corner of the excitation layer where the laser light is directed down the optical head into the cryostat with the help of a slanting mirror at the base of optical head. The components in excitation layer are shown in Fig.4.1(a). Dichroic beam splitters are optical elements in which reflection to transmission ratio is different in different range of wavelength. In the setup,it reflects the 632.8 nm laser light mostly and allows more transmission of laser light different from 632.8 nm when the reflected signal from sample comes back.

b) **Detection layer** : Laser light comes through the same physical space as in the excitation path. The detection layer receives the laser light reflected from the sample in cryostat and is then further send to the spectrometer through an optical fibre. This layer is arranged above the excitation layer so that the reflected signal having same wavelength component of excitation signal gets partly blocked by dichroic beam splitter in the excitation layer just before entering the collection layer. Once the laser light reaches the top right corner of collection layer, three mirrors are arranged at specific angles such that it will properly direct it to optical fibre. In addition there is a 633 nm razor edge long pass filter kept just before the entry to optical fibre to filter out the laser wavelength and only send signal of wavelength larger than laser to the spectrometer. The components in detection layer are shown in Fig. 4.1(c).

c) **LED illumination layer** : It is located below excitaton layer. Red LED light in the layer is used to illuminate the sample to view it with the camera. The same physical space through the top right corner of the optical head as

for the laser is utilized for illumination of the sample to view it.

d) **Camera layer** : This layer holds the camera to capture the live optical image of the sample in cryostat. Important to navigate to the device junction to do the raman mapping on the device junction.

In between the mirrors at bottom left and right corners in the excitation and collection layer there are two slots each available for new optical elements to be introduced. So there is a possibility to add polarizers in the two layers for polarization dependent optical measurements.

e) **Raman spectrometer** : The signal from detection layer finally ends in the spectrometer. The spectrometer has two grating sets to seperate out the signal of different energy spatially and the intensity of corresponding signal is recorded by CCD and is shown as the output in the software.

4.4 Strain setup II

The initial low temperature strain setup discussed in subsec. 3.2.2 is purely mechanical and it lacked the optical parts to do the strain characterization at low temperature. The newly designed strain setup for attoDRY2100 dry fridge opens up this possibility to do optics and electrical transport with strain as a new knob. It is a new tool to look into the strain distribution in device junctions at low temperature. The same principle of straining edge contacted graphene junctions by bending the flexible phosphor bronze substrate is still used but the way of bending in the new version of setup is carried out by driving a piezo walker unit. The possibility to bend the substrate using a pushing wedge technique as in subsec. 3.2.2 had to be avoided in the new version as it can interfere with the optical path if it is designed to come from above in the vertical direction and from bottom the scanners, positioners for Raman mapping makes it difficult to design such a system. Thus access to bend the substrate with pushing wedge technique is difficult. In collaboration with mechanical workshop the piezo walker setup is designed and fabricated to bend the substrate. The design, techniques and components of the piezo walker setup will be discussed in this section.

4.4.1 Design dimensions of piezo walker setup

The design of the strain setup began with the avaialble space in the dipstick of attoDRY2100[4]. To the bottom part of dipstick , a half open cylindrical metallic cage holds the positioner and scanner piezo units of attocube Raman

[4] a product of attocube.

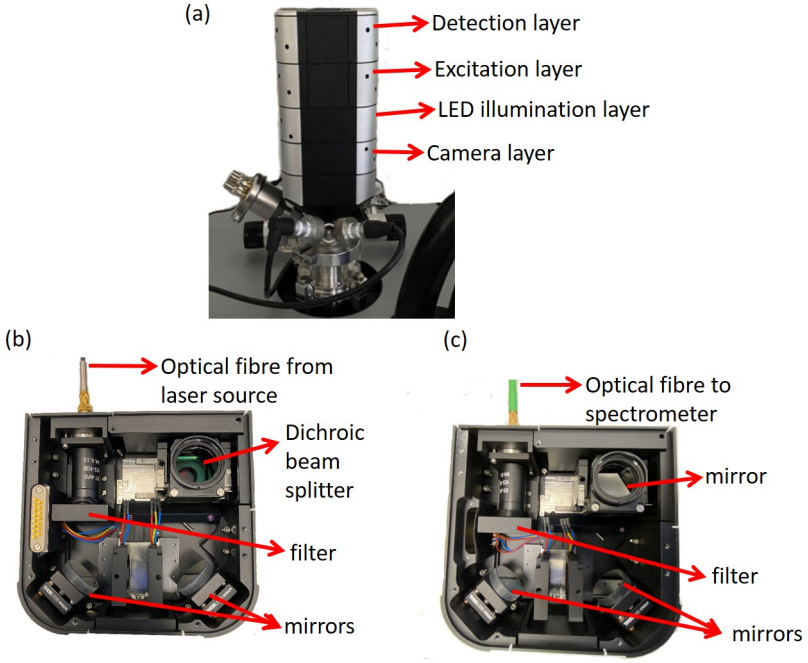

Figure 4.1 Optical head of setup. **(a)** Optical head on top of the cryostat labelled with different layers it is equipped with. **(b)** Cross-section showing components in the excitation layer. The laser light brought in by optical fibre is refelcted by mirrors and is directed downward into the cryostat. **(c)** Cross-section showing components in the detection layer. The reflected laser signal from sample is further reflected by mirrors and directed to the optical fibre to spectrometer.

microscope, shown in Fig. 4.2. The strain setup to be designed should fit into this part of the dipstick. The 33 mm opening in the front face of cylinder sets the limit for the size in horizontal direction. In the vertical direction space available between focal point of objective and the attocube sample stage is 12.3 mm. On considering the available dimensions of the components for the strain setup and the distance the setup needs to move to bend the substrate, it required more space in vertical direction. Thus the bottom spacer of 10 mm (shown in Fig.4.8) and attocube sample stage of 6 mm in height is removed for enough space for the strain setup. Thus the limit in the vertical direction is 28.3 mm.

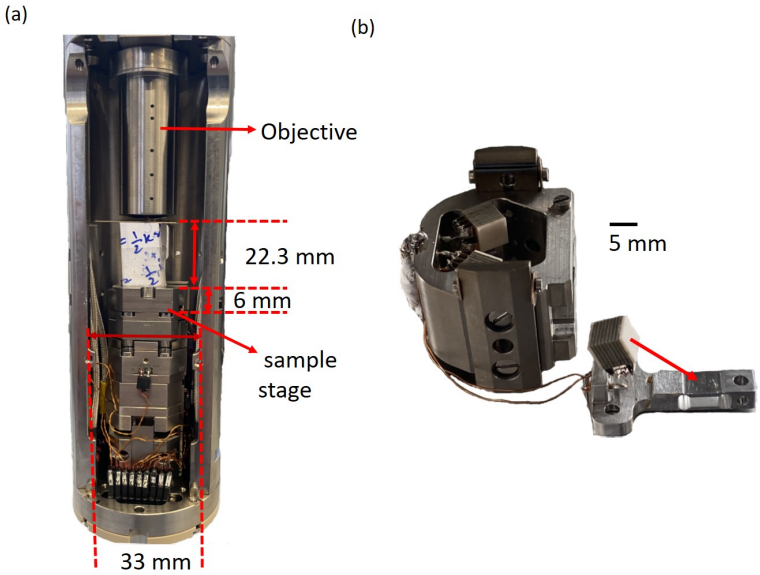

Figure 4.2 (a) Estimating the space available for the piezo walker setup in the bottom region of dipstick/microscope stick of the attodrY2100 system. **(b)** Outter titanium cage of the piezo walker setup, the piezo stacks are glued to it in the inside. The surface of the piezo stack to be glued is terminated with white alumina sheet, red arrow points to the location where that piezo stack need to be glued.

4.4.2 Components of piezo walker

The parts of the piezo walker unit are illustrated in Fig. 4.3. A brief description of the parts are highlighted below:

a) **outer titanium cage** - the clamps to hold the two ends of the substrate are fixed to it.

b) **center sapphire rod** - the wedge is attached at the top of the sapphire rod. It is hexagonal in cross section with three rough faces and three smooth faces. The three alternating faces of sapphire rod is polished to make it smooth for the piezo walkers to carrout the walking motion with less friction. The choice of three alternating face and not three adjacent face comes from the design of the setup which will be clear from Fig. 4.3.

c) **shear piezo actuators (piezo walkers)** - There are five shear piezo stacks in the piezo walker setup. One side of the piezo stack with square face is glued to the outter titanium cage and the face on the other side of stack contacts the smooth face of center hexagonal sapphire rod. Each shear piezo stack consists of 8 capacitors stacked together as a single unit with PZT(Lead Zirconium Titanate) as the piezoelectric material between the plates. The capacitor plate is 5 mm by 5 mm in areal dimension.

Assembly of parts

Here we shortly describe the assembly of the components of piezo walker setup step by step including details on the material of each component.

The choice of materials including titanium, sapphire, PZT, alumina, copper is based on thermal expansion of these materials as the setup will be cooled down from room temperature to low temperature [94–98]. The idea is to keep the stress occuring at the junction of differnt material types minimum by using materials with similar thermal expansion coeffcients.

The copper capacitor plates and PZT material is glued with epoxy glue, the two ends of the capacitor piezo stack is terminated with alumina sheet (white in colour, as shown in Fig. 4.2(b)) making electrical isolation from the outter titanium cage and also it makes good contact with epoxy glue to the titanium.

One face of piezo stack is fixed to the outter titanium cage at positions shown in Fig. 4.3 with T7110 epoxy glue(grey coloured). Four piezo stacks are glued to the outter titanium cage and the fifth one is glued to pre-loader with a different epoxy, EPO-TEK 353ND(shown in Fig. 4.2) as the preloader is made

out of aluminium. For the T7110 epoxy glue, after the process glued parts are left for one day without disturbance inorder for it to solidify. For EPO-TEK 353ND Epoxy, the glued parts are heat treated at 80°C for around 2 hours so that glue gets solidified and makes the adhesion stronger. The pre-loader is connected to the outter titanium cage with three screws, as shown in Fig. 4.3(b).

The center sapphire rod is connected to a base plate via a long screw which connects to wedge at the top, Fig. 4.3(a). The central sapphire rod is passed through the completely assembled outter titanium cage, the other square face of piezo stacks makes contact with the smooth surface of the central sapphire rod and is tightened with the screws on the pre-loader. The function of the three screws in the bending process will be discussed later in the section for optimisation of bending at low temperature.

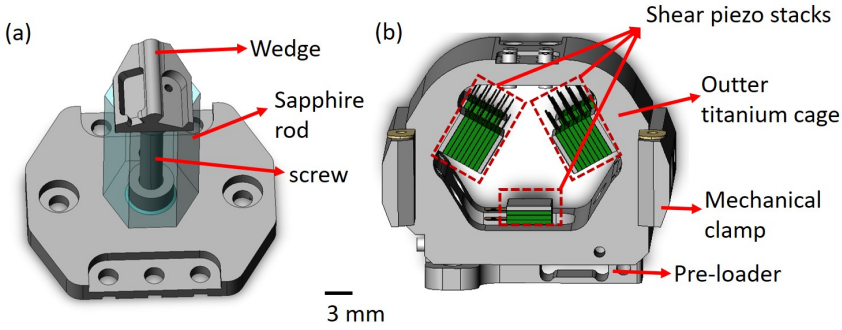

Figure 4.3 Parts of piezo walker strain setup. (a) The inner part, sapphire rod with a wedge at the top fixed to a base plate through a long screw. **(b)** Outter titanium cage with shear piezo stacks glued to the inner side of it.

4.4.3 Working of strain setup II

The working of the strain setup II to bend the substrate will be breifly described in this section. The shear piezo stacks are actuated with sawtooth voltage signal. The sawtooth voltage signal is supplied by home built piezo motor controller (PMC). The schematic of the up and down walking motion of the piezo walkers are illustrated in Fig. 4.5, where the sawtooth voltage signal with the corresponding motion happening to the shear piezo stacks are shown. The sawtooth voltage signal has two parts, a slow linear change in the voltage applied followed by a fast switching of the voltage polarity. The slow step is in

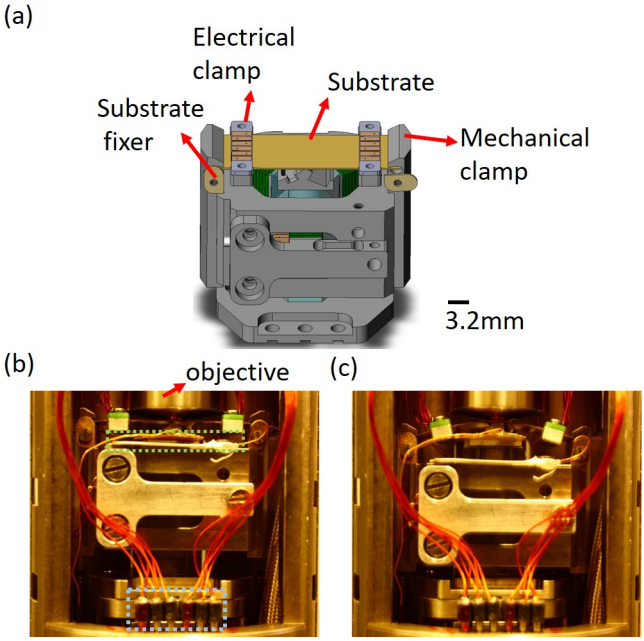

Figure 4.4 (a) Schematic of strain setup with substrate mounted. The schematic is made using Solidworks software in collaboraton with the mechanical workshop in the department. **(b),(c)** Initially unbend and completely bend substrate in the strain setup II after integrating it into the attocube system.

the millisecond time scale and fast switching in microsecond time scale. In the slow step, piezo stack makes the shear motion against the sapphire rod and in the fast step the piezo stack switches back to the original shape by making a small walking step on the sapphire rod. Depending on whether the polarity changes from positive to negative or vice-versa in the slow step, the outter titanium cage moves up or down with respect to the central sapphire rod. The maximum voltage that PMC can deliver is ± 400 V. The substrate is clamped at the two ends in the outter titanium cage and the center of substrate will be initially just in contact with the central wedge but still flat and not bend.

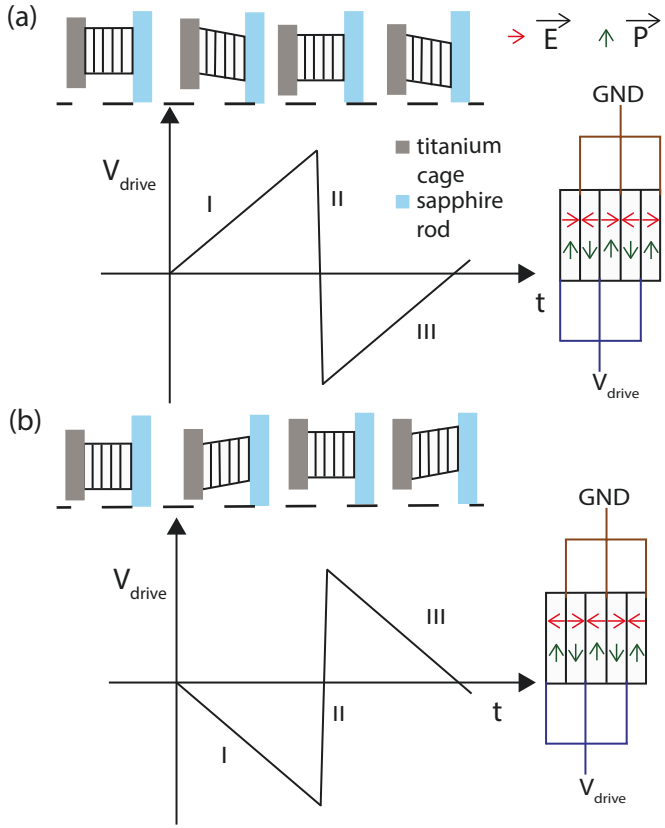

Figure 4.5 Schematic of the walking motion of piezo stack. One face of the piezo stack (represented by black square box comprising of 5 capacitors) is fixed to the titanium cage and the other face is in contact with smooth sapphire surface. A zoom in to the capacitor stack is shown next to the plot of drive signal (V_{drive}) versus time (t) for region I of drive signal with direction of applied electric field ($\vec{E}$) and polarization/poling direction of the piezo material ($\vec{P}$) in between the capacitor plates labeled. In other sections of the drive signal, direction of $\vec{E}$ changes in the diagram which will decide the shear direction. **(a)** Piezo stack walking down with the application of a positive sawtooth voltage drive. **(b)** Piezo stack walking up with the negative sawtooth voltage drive.

By applying a positive drive signal, outer titanium cage moves down with respect to wedge(as shown in Fig. 4.5(a)) and the substrate is pulled down at the two ends against the wedge at the center, which is kept fixed, thus resulting in bending of the substrate. Fig. 4.4(c) shows the substrate bend with strain setup II. The maximum distance outer titanium cage can move (Δz) at low temperature is $\sim$ 2.5 mm to bend the substrate. The drive voltage from PMC is increased from $\pm$ 180 V to $\pm$ 380 V to move the outer titanium cage from $\Delta z = 0$ to 2.5 mm in order to bend the substrate at low temperature.

Optimising the pre-loader for minimum driving voltage

As shown in Fig. 4.3 or Fig. 4.4, the preloader with one shear piezo stack glued to it presses on to the smooth surafce of central sapphire rod. The force with which it presses on to the central rod is decided by the three screws(as seen in Fig. 4.4) on the preloader which is screwed to the outer titanium cage. The single screw on the right side of the pre-loader is used to fix it to the outter titanium cage and the two screws on the left can be used to adjust how hard or soft the pre-loader is pressed to the sapphire rod. The more tighter the screws on the left side, it requires a higher peak voltage of sawtooth signal to make the shear piezo stack to start the walking motion. But on the other extreme, if it is too loose there won't be good enough contact of piezo walkers to the sapphire rod to make the walking motion. Therefore, the two screws are adjusted in a way to minimize the peak voltage of the sawtooth signal required to drive the piezo walkers.

4.4.4 Dimensions of substrate used in strain setup II

The substrate material (phosphor bronze) used and processes involved in its preparation are same as described in subsec. 3.2.1. The dimensions of the new setup and the force that the piezo walkers could deliver to bend the the substrate lead to changes in dimesnions of the substrate to be used compared to that in strain setup I. This section will breifly describe the key factors that went into deciding the substrate dimension for the devices to be fabricated for strain setup II.

In strain setup I, substrate is 0.3 mm thick and the initial bending tests in strain setup II were carried out with this 0.3 mm thick substrate. From Fig. 4.6, the 0.3 mm thick substrate requires drive voltage higher than $\pm$165 V to bend by the same amount as 0.2 mm thick substrate bend with $\pm$74 V at room temperature. The drive voltage is supplied by Piezo Motor Controller (PMC), discussed in subsec. 4.4.3. The strain experiments to be carried out is at low temperature, 1.6 K. The shear piezo electric deformation coefficient (d_{15}) decreases with temperature [99] and thus the voltage to be applied to

piezo walkers to bend the substrate by the same amount as at room temperature will be higher. From the bending test at low temperature, 0.2 mm thick substrate starts to bend at ±180 V and to achieve a bending of 1.6 mm the voltage needs to be increased to ±250 V. So for 0.2 mm thick substrate,the voltage required at low temperature is 2.5-3 times that at room temperature. Thus for 0.3 mm thick substrate, the voltage required at low temeprature to initiate the bending will be closer to the limits of PMC, i.e.,±400 V and for bending by 1.6 mm it will go beyond the voltage limits of PMC. The voltage limits of PMC lead to the choice of thinner substrate. Also on considering the safety of fabricated samples, the objective is to keep the drive voltage as minimum as possible.

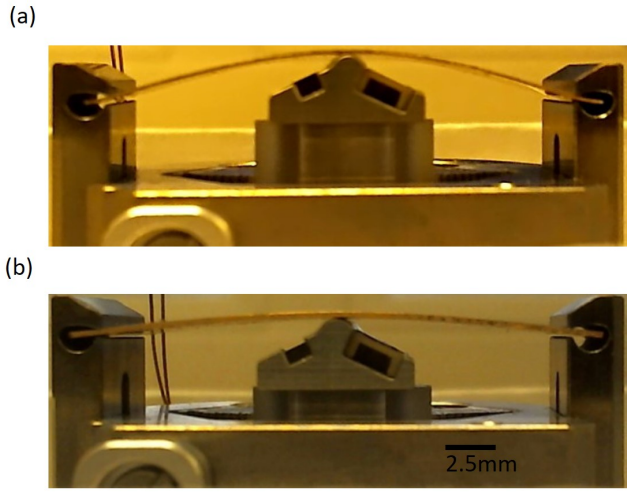

Figure 4.6 Bending test at room temperature. **(a)** 0.2 mm thick substrate bend with $V_p = \pm 74$ V delivered from PMC. **(b)** 0.3 mm thick substrate bend with $V_p = \pm 165$ V.

But the choice of thinner substrate will also have an impact on the strain generated in the device junction as it depends on the substrate thickness,Eq. 2.64. Also, thinner substrate can get bend in the fabrication process easily, making it not ideal for strain experiments. Based on all these considerations 0.2 mm thick substrate is taken as the best choice over 0.3 mm for strain setup II.

The length of the substrate needs to be increased from 24 mm(used in strain setup I) to 28.45 mm so that electrical clamps connected to the substrate are

spaced adequately for the objective lens to be brought in focus on the device junction,as illustrated in Fig. 4.7(a),(b). The width of the substrate is 10 mm so that it perfectly fits the length of mechanical clamps(Fig. 4.4(a)) on the outer titanium cage.

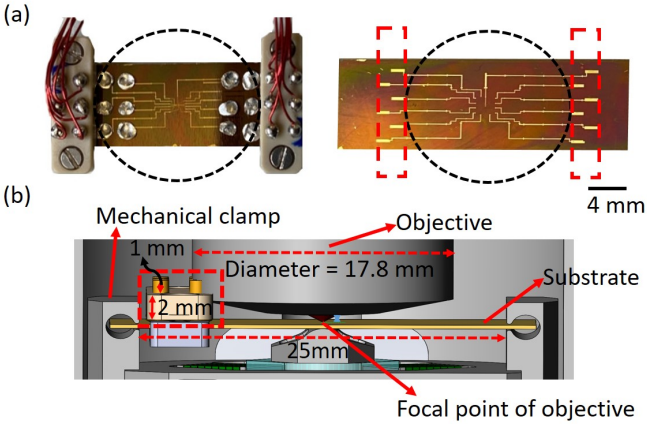

Figure 4.7 (a) The electrical clamps fixed at the left and right end of the substrate should be spaced by a distance of nearly the diameter of objective. This is to ensure that objective will not hit the clamps when the sample/laser spot is focussed. The black dotted circle is the cross section of objective lens. The left image shows device substrate for strain setup I, contact clamps should be at the position of pressed indium pieces but the objective diameter size being large requires the clamps to be spaced out. Thus the devices designed for strain setup I will not fit in strain setup II. The right image shows the newly designed device susbtrate for strain setup II with contact pad positions(red dotted rectangles) outside the objective lens cross section. **(b)** The thickness of electrical clamp should be designed as thin as possible. The clamps used in strain setup I is thicker and will not go with strain setup II. The upper part of clamp should be designed less than 3mm thick as objective can hit the clamp when it is brought to focus on the substrate.

4.4.5 Integrating strain setup II to attocube system

The bottom spacer (10 mm) and attocube sample stage (6 mm) is removed from the attocube piezo stack. Then the whole attocube piezo stack required to be turned 90° so that the screw holes on the bottom z positioner piezo stack

matches with those on base circular electronic plate of attocube piezo stack. A thin spacer of 3 mm is screwed at the top of x,y,z scanner and on top of that the strain setup is mounted. First the central sapphire rod part is fixed to the thin spacer and then the assembled outer titanium cage with pre-loader is fixed around the sapphire rod by tightening the screws on the pre-loader. An important reminder to be kept in mind, the face of capacitor piezo stack should make contact with smooth sapphire surface for the proper walking motion of piezo stacks. Fig. 4.8 shows the whole piezo stack of the attodry2100 system before and after adding the strain setup. Now the integrated system can be loaded into the bottom part of dipstick, as shown in Fig. 4.2

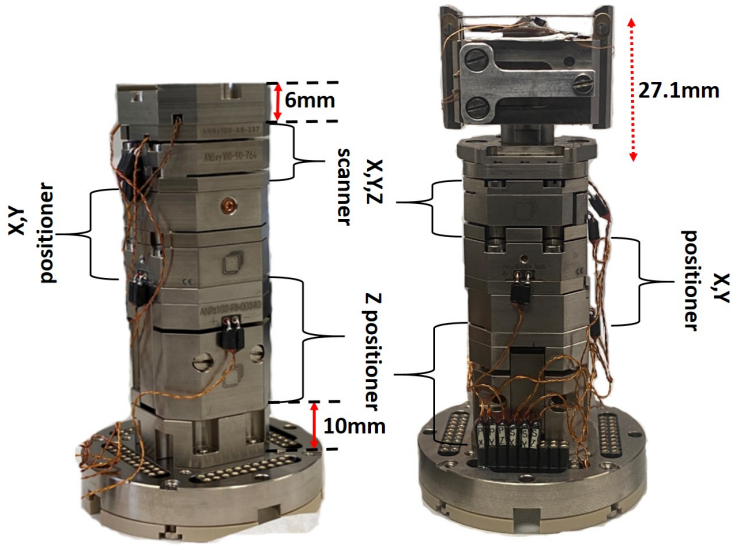

Figure 4.8 Integration of strain setup II to attocube setup. The attocube piezo stack, comprising of positioner and scanner piezo along with a 10 mm high bottom spacer and 6 mm high sample stage is shown in the left image. The image on right side shows the attocube piezo stack with the home built strain setup II integrated to it. The steps involved replacing bottom spacer and sample stage in attocube piezo stack followed by adding strain setup to the attocube piezo stack.

4.5 Electrical connection to samples in strain setup II

The technique of contacting the nanofabricated contact pads in the device substrate is slightly improvised in strain setup II. The old technique of putting small indium pieces on the contact pads and further pressing with the clamps(as discussed in subsec. 3.2.3) is replaced by a PCB clamp with indium balls pre-soldered on it. This allows direct clamping of it on to the device substrate by screwing with the counterpart. This section describes the design and fabrication of the electrical clamps, a vital component to carry out the transport measurements as wire bonding doesn't work in these devices (discussed in subsec. 3.2.3).

4.5.1 Design and material for electrical clamp

The electrical clamp is made out of a PCB. The PCB[5] used for the design of electrical clamp should be thick enough so that it will not bend much at the middle when the two ends of it are screwed to its counterpart with the substrate in between and also not too thick to hit the objective when it is brought in to focus on the sample (this issue is shown in Fig. 4.7(b)). These constraints had to be taken into account for the design for electrical clamp. The design of the electrical clamp is shown in Fig. 4.9, one side with round gold pads and the other side with rectangular gold pads. The round gold pads make a via contact through copper to the rectangular gold pads on the other side of the PCB. The position of the round gold pads are fixed with the design of the nanofabricated contact pads on the substrate. Indium solder of equal amount is put on the round gold pads, which makes contact to the gold contact pads on the substrate. The technique and materials involved in making equal-sized indium solder balls on the PCB electrical clamp is described in the following:

Indium pre-soldering on the electrical clamp

The steps and tricks involved in it are the following:
(a) The whole PCB with 10 electrical clamps is taken to the soldering station while we ensure that it is kept on a fairly clean surface. (b) The indium solder ball is soldered on the round gold pads (in left of Fig. 3.5a) one by one. The solder wire is 99.99% pure indium(In100), which is soft. (c) The round gold pad is composed of chemical gold. The indium solder will not adhere to the chemical gold without the required flux. The indium wire used doesn't have any flux in its core. (d) The flux we use is SMD291, a bit of flux is put over the round gold pads first and then the solder is put by initially

[5]The design for the clamp is made in collaboration with electronics workshop in the Physics department. PCB with this specific design is manufactured by **multi-cb printed circui boards**in Germany

heating the round gold pads. (e) The temperature of the soldering unit is maintained around 320° C. The flux helps the indium to spread on to the round gold pad and provides the surface tension. In the first round, small amount of indium solder is placed on the round gold pads, and the second round is used to give a fine finishing touch to the solder balls to ensure equal height within each of the electrical clamp. This is to ensure it makes uniform contact when its further used in next step to electrically clamp the fabricated device. (f) The flux residues left on the whole PCB needs to be cleaned. The chemical solution called fluxclene, a fast drying solvent (PCB cleaning solution), is used initially to brush the flux residue out, followed by a wash in ethanol or IPA , then drying with compressed air. (g) The next step is to cut the 10 electrical clamps out of the whole PCB. This is done in the mechanical workshop using a vertical cutting tool. The PCB is mounted on a metal block holder for clamping in the cutting setup. The sharp tip of the machine can be programmed to move in x,y,z directions and thus it moves over the PCB and makes the vertical cuts at defined positions of the electrical clamp. The instrument used is FEHLMANN-Picomax 60M from the mechanical workshop in the department, shown in Fig. 4.10.

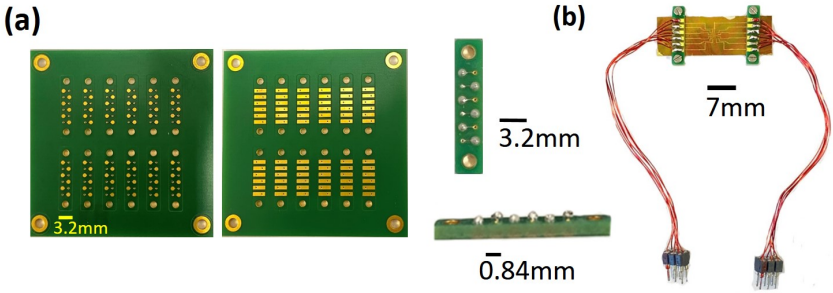

Figure 4.9 Electrical clamping. **(a)** PCB with printed clamps, the two square images shows the two sides of the PCB board. The round gold pads are via connected to the rectangle gold pads. Indium solder balls are soldered on top of the round gold pads of the clamp, and further the PCB is cut to get individual clamp pieces as shown in rightmost image of Fig. 4.9(a) . These indium on pcb is pressed to the contact pads on the device substrate and the clamps are fixed by screwing it to the counterpart. **(b)** Fabricated device after electrical clamping. The pins further make the connection to electrical lines in dipstick and from there to the measurement electronics.

The connector pins are soldered to the rectangular gold pads on the electrical clamp, which can then be plugged into the socket in the dipstick to establish

connections with the measurement electronics. In the other direction, the contact pads on the substrate are connected to the devices through on-chip metallic lines. The electrical clamps desgined are shown in Fig. 4.9. Since the setup has 12 lines for electrical mesurements, thus 12 electrical contacts are available for device junctions to be designed, including the gate electrodes.

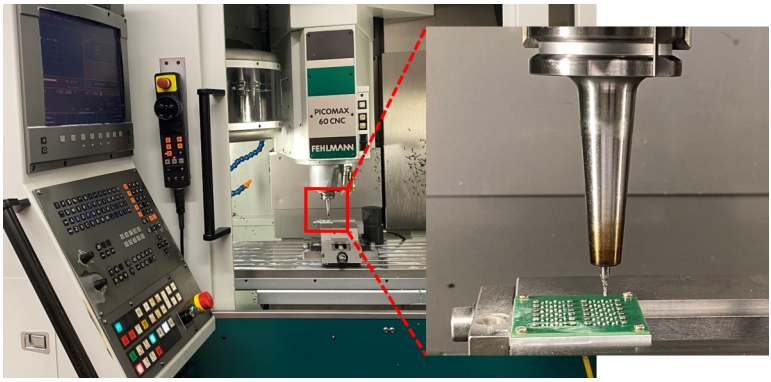

Figure 4.10 Mechanical cutting tool to cut out the electrical clamps. The coordinates from the design file for the pcb board with electrical clamps can be loaded in this system and the cutting procedure is automated.

4.6 Isolating high voltage piezo driving signal from the electrical lines to sample

In the initial measurements with strain setup II, the devices fabricated were not successfull to finish a strain cycle as the device exploded. The blow up happens when the shear piezo is driven to bend the substrate. The sample junctions are kept grounded while driving the shear piezo stack. Thus a solution to this problem is necessary for successfull measurement in the setup. The sample lines are grounded through breakoutbox to the main ground of the cryostat.

Possibilities for electrical damage to the device

Some of the issues observed which can be a possible reason for the electrical explosion of device are as follows :
(a) Absence of better shielding of the high voltage lines to the piezo walkers, starting from the top fischer connector to the strain setup towards the bottom

of dipstick.
(b) Absence of better shielding of the components in the strain setup around the region where substrate is mounted.

(c) The thermalising unit(see Fig. 4.11) of three cylindrical copper pieces were not grounded, where all the electrical lines are wound around these copper pieces for thermalisation.

(d) The bottom cylindrical cage holding the whole attocube piezo stack was isolted from ground by design of the attocube system.

Shielding and Grounding required for strain setup II

(a) Piezo motor controller (PMC) delivers the sawtooth voltage signal to piezo walkers. The two lines from the PMC continue along the dipstick to the piezo walkers via the connection through fischer cable at the top of dipstick. One line is ground and other carries the sawtooth voltage signal. These high voltage lines to the piezo walkers are replaced from the insulated copper cables to flexible coaxial cable for achieving better shielding. The inner line of coaxial cable carries the sawtooth voltage signal and the outer shield is the ground line.

(b) The components of the strain setup including the outter titanium cage, central wedge are grounded.

(c) The thermalising unit (see Fig. 4.11) of three cylindrical copper pieces are further grounded to minmize the coupling between the electrical lines to sample and high voltage lines. Also, bottom cylindrical cage (shown in Fig. 4.2(a)) holding the the whole attocube piezo stack is grounded.

(d) In Fig. 4.3(b), the pins to the capacitor plates are shown and the ground line is connected to the set of pins on the top side, so that pins corresponding to the opposite plates of capacitors connected with the sawtooth signal are away from the device. This is carried out to minimize the coupling between piezo drive signal and electrical lines to the sample or directly to the sample.

(e) The ground of the electrical lines to the sample had to be changed from the main ground of cryostat with that of the ground line from PMC. This is an important step, as it helped to avoid the electrical explosion. During the piezo drive of the walkers, it seems that ground to the sample lifts up in potential and it can be that diferent electrical lines get lifted up in potential slighlty different causing a voltage drop across the sample and resulting in the explosion by driving large current. After choosing ground line of PMC as the ground for sample, the issue seems to get resolved.

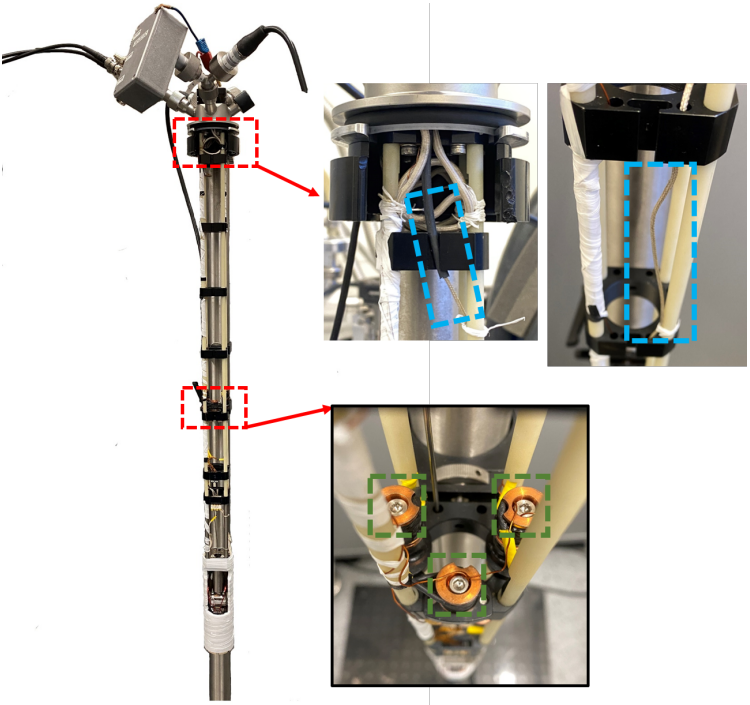

Figure 4.11 Shielding, grounding in the setup. The image on left is dipstick of the setup, the two red box regions are zoomed in to show the coaxial cable to piezo walkers and the thermalisation unit in the dipstick. The top image on right side : Blue dashed box shows the coaxial cable coming from the Fischer connectors at the top of dipstick, further continues along the dipstick to the piezo walkers towards the bottom of dipstick. The coaxial cable that carries the high voltage lines to the piezo walkers in strain setup. The bottom image on right side : The three copper pieces(marked with green dashed box) are connected to ground to minimize the coupling between high voltage lines and electical lines to the sample. The electrical wires that comes from the fischer cables at the top of dipstick is wound around these three copper pieces for thermalisation.

4.7 Measuring the distance moved by outer titanium cage (Δz) to bend/unbend the substrate

The distance moved by outer titanium cage with respect to central wedge in strain setup II is represented by Δz (equivalent to the distance moved by central wedge to bend the substrate in strain setup I,Ch. 3). At room temperature when the dispstick is outside, Δz can be measured directly for different bending of the substrate with the help of photographs for each state of substrate bending, like in Fig. 4.4(b),(c). However once it is loaded inside the fridge, Δz cant't be measured directly anymore. In order to measure Δz at low temperature,the idea is to implement a capacitor sensor in strain setup II that tells how much distance outer titanium cage moved with respect to central wedge. One of the capacitor plate is fixed to the outer titanium cage and the other to the central wedge. Both the plates are isolated using teflon tape from the electrically grounded outer titanium cage and central wedge.

4.7.1 Dependance of measured capacitance to Δz

In this section we try to establish a way to read out Δz from the capacitance measured. Fig. 4.4(b) shows the capacitor plates,within the green dotted box but not that clearly visible in the picture. If one carefully look it is also in Fig. 4.4(c) in front of the wedge with a larger seperation distance between the plates compared to that in Fig. 4.4(b).

A 1 V signal with a frequency (f) 10 kHz is applied to the capacitor plate fixed at the central wedge and the current from the other plate is read out at the lock-in amplifier using an I/V converter. The Y component of the lock-in signal (V_y) is monitored with the bending as it is the capacitive signal with a phase shift of 90°, ideally with respect to the input voltage signal (V_{ap}). In the callibration carried out, phase shift of the signal measured in the lockin is between 85-86°. The gain (IV_g) in the I/V converter used is 10^6 V/A. For the optimised setting of the pre-loader, Δz is measured at room temeprature with help of photographs taken at each bending step and the corresponding V_y in lockin is recorded. The plot below shows capacitance(C) from the measured capacitive current (I_m) versus Δz for two bending and unbending cycles at room temperature.

$$C = \frac{I_m}{2\pi f V_{ap}} = \frac{V_y \times IV_g}{2\pi f V_{app}} \tag{4.1}$$

To determine Δz at low temperature, we assume that at low temperature the change in V_y for the same Δz remains constant. But there will be an offset in the V_y with the temperature change and environment change once when the dipstick is placed inside the fridge. So subtracting this offset from the room temperature callibration curve of C versus Δz gives the one at low

temperature. As the substrate is bend, the capacitor plate attached to outer titanium cage moves down along with it and the distance increases between the plates (the plate atatched central wedge reamins at the same position). This leads to decrease in capacitance with increase in Δz, as shown in Fig. 4.12. Thus, monitoring the capacitance (C) with bending at low temperature, an estimate for the Δz can be made. Apart from knowing Δz, it is important to

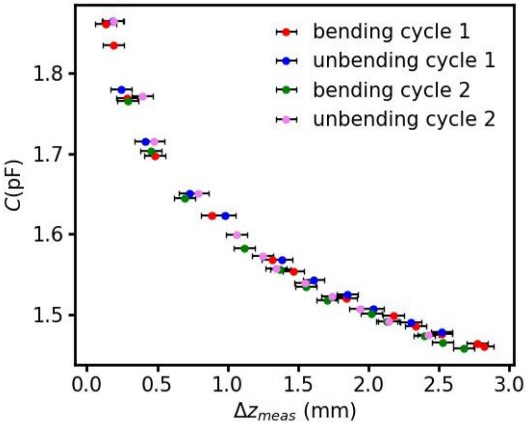

Figure 4.12 Capacitance(C) versus Δz. Plot of capacitance(C) calculated with I_m using Eq. 4.1 versus Δz (bending distance) measured for two complete bending cycles at room temperature outside the cryostat from the capacitor sensor.

know whether the bending process occurs at low temperature because there is no other way to detect it. Thus, the capacitor sensor implemented is very useful tool to monitor Δz and whether the strain setup itself is working or not at low temperature.

4.8 Mathematical form for the bending achieved in the setup

This section discusses the bending profile obtained in strain setup II for the substrate by looking at the best fit polynomial that can describe the profile.

By knowing the bending curvature of the substrate, one can estimate the tensile strain on the top surface of the substrate. With the help of photographs of the bend substrate, polynomial form for the bending profile of the substrate can be deduced. The midline points along the thickness (points at the middle of substrate along the thickness direction) of substrate is used as the data

points to extract the form of bending through polynomial fit. The bending profile from the fit as shown in Fig. 4.13 with quadratic(w_q), cubic(w_c) and biquadratic(w_{bq}) polynomials are:

$$w_q(x) = -0.05314x^2 - 0.00021x + 3.05062 \tag{4.2}$$

$$w_c(x) = 0.00009x^3 - 0.05314x^2 - 0.00138x + 3.05032 \tag{4.3}$$

$$w_{bq}(x) = 0.00082x^4 + 0.00007x^3 - 0.06803x^2 - 0.00096x + 3.14867 \tag{4.4}$$

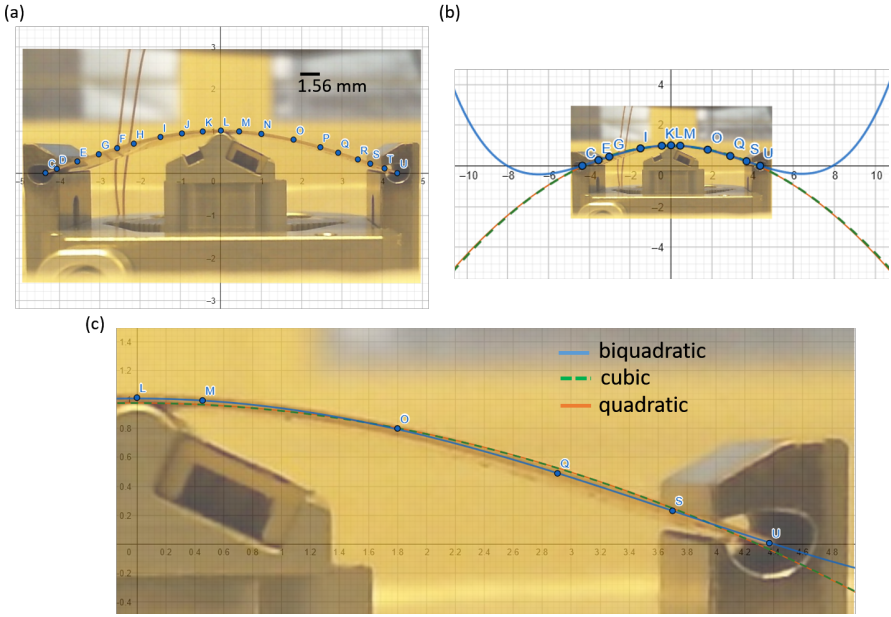

Figure 4.13 Polynomial form for bending of substrate. **(a)** Substrate bend under freely clamped boundary condition at either ends. The blue marked points tracks the midline along the thickness of substrate. **(b)** Polynomial fit through the midline points using quadratic(orange solid line),cubic(green dashed line),biquadratic(fourth power polynomial,blue solid line) functions. It looks like all the three forms well describe the bending profile but that's not the case. **(c)** Zoom in to the right side of the polynomial bending fit in Fig.**(b)**. Its clear that biquadratic polynomial function follows the bending profile better compared to cubic and quadratic functions.

From Fig. 4.13(c), the biquadratic (fourth order) polynomial provides the best

fit compared to cubic and quadratic, in tracing the bending profile especially towards the clamping region where the slope of the bend substrate is not followed by cubic and quadratic polynomial forms. Ideally, the bending should be symmetric about the central wedge but the odd power terms in the polynomial fit indicates the asymmetry. The asymmetric terms are very small as can be seen in Eq. 4.4. The constant term in each of the polynomial form indicates the maximum bending deflection at the center, measured from the vertical position of the end of substrate. But in the equation for bending of plates, the maximum deflection is the height measured from the point of clamping. Taking this to consideration, the maximum bending deflection at the center in Fig. 4.13 is $\sim$ 2.84 mm.

The bending profile derived in subsec. 2.4.3 considered load in the form of delta function at the either end of substrate with simply supported boundary condition. The bending profile with this load distribution is cubic polynomial. But from the fit fourth order polynomial is better in describing the bending profile in the setup compared to the cubic. In all the polynomial forms from the fit as well as the one derived in Eq. 2.86 qudratic term are atleast two order of magnitude larger than cubic or fourth order term.

4.8.1 Estimate of tensile strain on top surface of substrate

The tensile strain along x direction as given in Eq. 2.64,

$$\varepsilon_{\mathrm{xx}} = -\mathrm{z}\frac{\partial^2 \mathrm{w}}{\partial^2 \mathrm{x}} \tag{4.5}$$

For the top surface of the substrate $z = h/2$ where h is the thickness of substrate. A comparison can be made between the the tensile strain estimated from : (i) biquadratic polynomial fit(subsec. 4.8) and (ii) the cubic polynomial derived in subsec. 2.4.4. At the center of substrate, x= 0 :
(i) Using biquadratic polynomial fit, Eq. 4.4 : ε_{xx} = -h/2×(-0.06803) $\sim$ 0.68% tensile strain.
(ii) Using Eq. 2.86, $\varepsilon_{xx} = 12hw_{max}/2L^2 \sim$ 0.53% tensile strain for w_{max} = 2.84 mm , L is the length of substrate between the mechanical clamps(= 24 mm)

Both estimates show that the tensile strain at the top of substrate from the maximum bending in strain setup II is less than 1%. The tensile strain at the top of the substrate is transferred to the edge contacted device junction. On top of the phosphor bronze substrate lies a layer of polyimide polymer ($\sim$ 5 μm thick) and further gold contact pads. The amount of strain transferred from substrate to the polyimide layer is not known, but deducing the strain in graphene device junction using Raman spectroscopy gives an idea about how

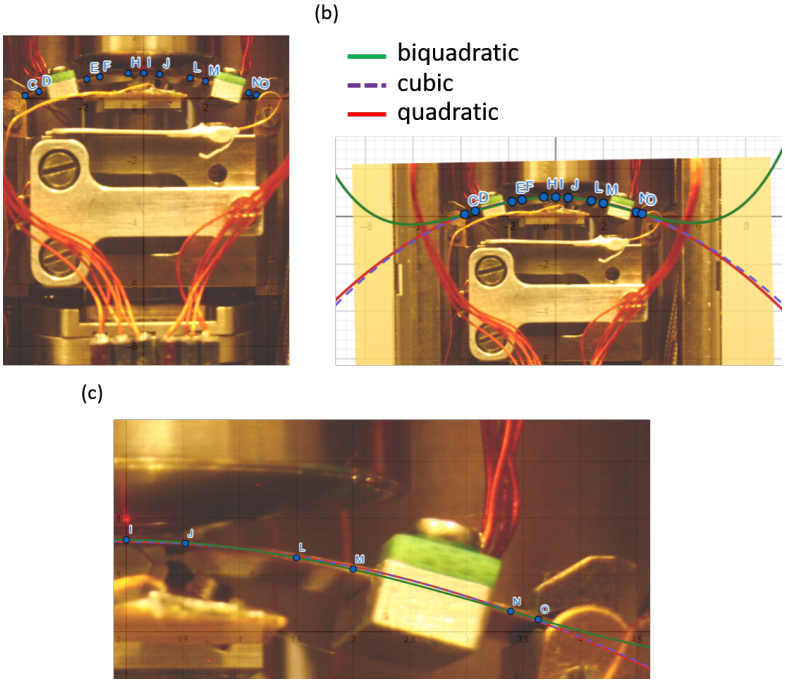

Figure 4.14 Bending profile after complete integration of setup in the attocube system. **(a)** Bending of substrate after fully integrating to the attocube system with electrical contacts on the substrate.**(b)** Fitting the bending to different polynomial types : quadratic(red solid line), cubic(violet dashed line), biquadratic(green solid line). **(c)** Zoom in to the right side of the bend substrate. The presence of electrical contact clamps didn't made a big change as the biquadratic polynomial still describes bending profile the best.

much fraction of the strain could be transferred from the substrate to edge contacted graphene junction. The strain attained in the graphene junction will be discussed in coming section, subsec. 4.9.1.

4.9 Strain Characterization in graphene device junction with strain setup II

This section demonstrates strain characterization in edge contacted graphene device with strain setup II at low temperature (1.6 K).

As mentioned in subsec. 2.5.3, tunable tensile strain in these devices are characterised using saptial Raman mapping of peak position of 2D (ω_{2D}) raman band in graphene. Fig. 4.15(a) shows the spatial map of ω_{2D} for different bending distance(Δz) in a square shaped device junction at low temperature (1.6 K). As Δz increases, the spatial map turns to darker side of colorbar indicating red shift of ω_{2D}. The red shift in ω_{2D} indicates the increase of tensile strain in graphene in the device junction, also shown previously in Ref. [25] for edge contacted device junctions. The mechanics happening here is that upon bending the substrate, the edge contact pulls on either end of the device junction and results in the tensile strain. At $\Delta z = 0$ mm in Fig. 4.15(a), the variations in ω_{2D} is clearly visible which can be a result of in built strain variation from stacking or a different dopant concentration [100].

The shift of spatial average of $\omega_{2D}(\bar{\omega}_{2D})$ with Δz is used as a measure to quantify the tensile strain(ε) using $\frac{\partial \bar{\omega}_{2D}}{\partial \epsilon}$ = -54 cm^{-1}/% strain [74]. Fig. 4.15(b) shows two sets of plots : (i) left axis : $\bar{\omega}_{2D}$ versus Δz (ii) right axis : ε versus Δz , for unbending and bending cycle. The shift in $\bar{\omega}_{2D}$ with Δz seems linear , also reversible in bending and unbending cycles. The mismatch of reversibility in unbending and bending cycle is around $\sim$ 0.9 rel.cm^{-1} for $\Delta z < 1.3$ mm and towards higher $\Delta z > 1.3$ mm the mismatch reduces to 0.5-0.6 rel.cm^{-1} , it can be due to the hysteresis in the bending setup or at the edge contacts in the bending and unbending cycles . The spectrometer resolution comes around $\sim$ 0.3-0.5 rel.cm^{-1}. The blue dotted line in Fig. 4.15(b) is the linear fit to ε versus Δz in the unbending and bending cycles. The magnitude of slopes in the two cycles are 0.057%/mm and 0.051%/mm, thus on an average by bending the susbtrate 1 mm generates a tensile strain of 0.054% in the graphene device junction. The maximum strain attained in rectangular/square device junction is around $\sim$ 0.14% for $\Delta z = 2.5$ mm in strain setup II.

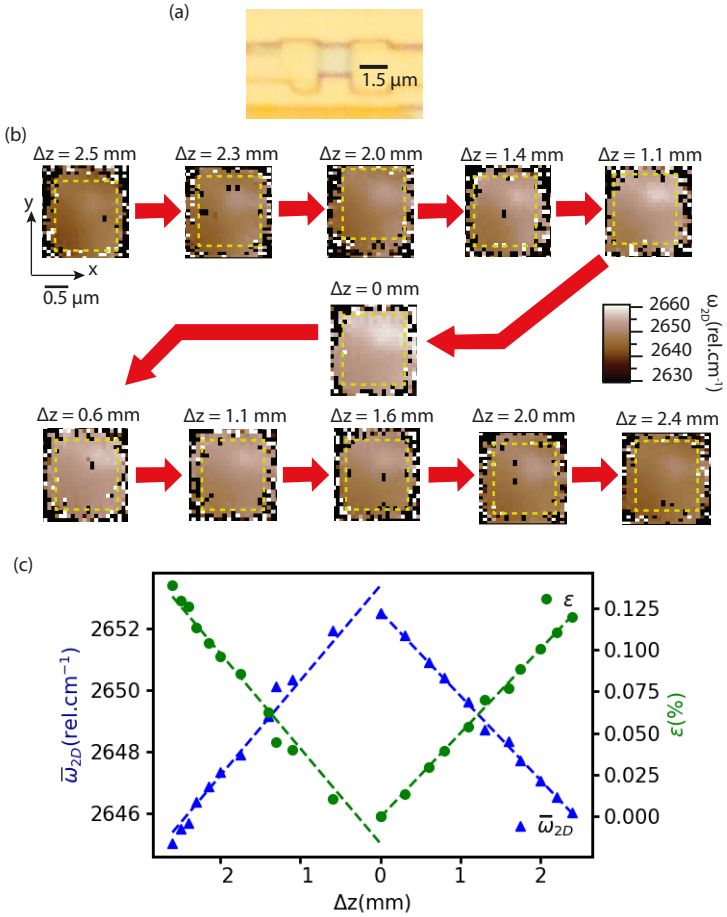

Figure 4.15 Spatial Raman mapping in square device geometry (a) Optical image of the two terminal square device junction **(b)** Saptial map of ω_{2D} for different Δz. The yellow dotted line marks the boundary of device junction. Higher Δz results in red shift of ω_{2D} and the map changes towards darker side of color scale. **(c)** Left axis :Spatial average of $\omega_{2D}(\bar{\omega}_{2D})$ versus Δz for unbending and bending cycle. The blue dotted line is a linear fit to the plot. Right axis : Estimated tunable strain(ε) versus Δz using $\frac{\partial \omega_{2D}}{\partial \epsilon}$ = -54 $cm^{-1}/\%$. The green dotted lines are linear fit to ε for the unbending and bending cycle.

4.9.1 Estimate for the strain transffered from substrate to graphene device

In sub sec. 4.8.1 an estimate for the upper limit of tensile strain in the top surface of substrate is discussed and for $\Delta z = 2.5$ mm its in the range of 0.48 - 0.6 %. This is under the assumption that midplane of substrate is not under stress and strain but towards large bending distance this assumption breaksdown. The maximum strain attained in graphene device junction is $\sim$ 0.14 % for $\Delta z = 2.5$ mm in strain setup II from above. This gives a lower limit of around one-fourth of the tensile strain transferred from the top of substrate to graphene device junction. It can also be possible that part of the strain is relaxed in the polyimide layer in between the top surface of substrate and edge contacts.

4.10 Summary

In conclusion,the design and integration of strain setup for cryogenic temperature based on piezo walkers is demonstrated. Shielding the electric lines to device from the high voltage lines to the piezo walkers as well as providing a proper ground to the sample during when piezo walkers are actuated are important for the safety of the sample in such sytem. The sucessful implementation of a capacitor sensor using metal plates to estimate Δz (the bending distance) at low temperature is further demonstrated. Not only as a sensor but it is also a necessity in such systems to know whether the bending itself is working at low temperature as no other gauge is present in system. Based on the bending profile obtained from the setup and the strain characterised with Raman spectroscopy in graphene junction shows that upto a lower limit of one-fourth of the strain is transferred from substrate to the device. The maximum strain obtained in the graphene device junction is $\sim$ 0.14%. It is also possible that part of the strain from the top surface of substrate get relaxed in the polyimide layer in between the substrate and the edge contacted device junction.

The setup built combines optics, charge carrier transport and strain engineering at cryogenic temperature with a high magnetic field upto 9 T. The parameter set one has in such a setup is large giving options to explore wide range of properties of a material. The requirement of high voltage to drive ($\pm$380 V) the piezo walkers at low temperature is a drawback of strain setup with such a design. The strain setup design can be further optimised to reduce the requirement of high drive voltage by including more shear piezo stack/walker units so that the mechanical load to bend the substrate is shared by more piezo stacks. The distance outer titanium cage can move(Δz) is limited to $\sim$ 2.5 mm by the availability of space in the attocube system for the strain setup.

As the edge contacts to the graphene junction didn't break even after bending by $\Delta z = 2.5$ mm at low temperature, so it is possible to generate more strain in such a setup by bending more but we are limited by the space. How one can generate more strain for same Δz will be discussed in Ch. 8.

5 Strain effects on edge contact characteristics

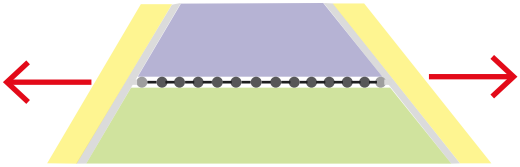

In this chapter we investigate in some detail how our bending experiments affect the edge contact[1] characterisitcs of encapsulated graphene devices. These effects are probably not due to the strain in graphene, but some changes in the edge contact, like bond lengths, energy alignment of states near the contacts. The edge contact to the device serves the two roles of transmitting charge carriers into the graphene junction region and of transmitting the mechanical force that generates strain in the graphene. For too large strain, metal-graphene contact interface breaks up mechanically, which also breaks the electrical contact. For tensile strain values below this breaking limit, two terminal conductance increases with increasing strain. In general in our strain experiments we measure a two terminal differential conductance either in a two or four terminal geometry. While we believe that the latter is only sensitive to the bulk and edge properties between the voltage probes, we find that the two-terminal experiments also contain the contact resistances of the involved contacts, so that they can be used to investigate the contact characteristics when under a mechanical deformation - similar to break-junction experiments [5, 6]. As we show at the start of this chapter, the contact resistance as read off from the large gate voltage limit, decreases with increasing strain, an effect that is found in the two-terminal experiments. We then use two different models to extract the contact characteristics, one in which we assume a ballistic graphene layer, and one in the diffusive limit. Both models show consistently that the transmission between the reservoirs and the graphene increases with increasing strain, a finding that is rather unintuitive, so that we can only speculate about the reason.

[1] Schematic of a cross section of hBN encapsulated graphene with edge contacts exerting force at the interface.

5.1 Introduction

The technique of edge contacting the graphene results in lower contact resistances [33, 101, 102]. The graphene is edge contacted with Cr/Au which seems to be the best metal for edge contacting graphene [33]. The edge contacts(Cr atoms) in graphene form σ bond with C atoms whereas surface contact overlaps with the p_z orbital resulting in a weaker van der Waals type interaction. Tensile strain has been shown to improve the mobility in graphene by reducing the strain fluctuations in samples of low mobility [53]. In addition to strain changing the channel properties, it can also change the metal-graphene contact properties. In the extreme case, higher tensile strain will lead to mechanical failure of contacts. We believe that in this mechanical breaking, the chemical bonds get significally elongated, with a corresponding reduction in the wavefunction overlap and a strong reduction of the conductance. This is the regime that is easily understood intuitively. Here we aim to investigate effects in the contact characteristics before the mechanical breakdown.

This chapter discusses the effect of bending the substrate on the electrical contact characteristics. It is followed by a brief discussion on the possible mechanism for the increase in two terminal conductance with strain before the breaking limit of metal-graphene junction.

5.2 Conductance change with bending

The changes observed in two terminal differential conductance (G_{2t}) of graphene junction with back gate voltage (V_{bg}) for different Δz (distance moved by wedge to bend the substrate, illustrated in Fig. 3.8) will be discussed in this section. The edge contacted graphene is strained with bending of substrate as discussed in Ch. 3. From Eq. 2.31, the total conductance of the two terminal device junction saturate to a value fixed by the contact resistance towards higher carrier density (n). The two terminal differential conductance measurements carried out in a square shaped junction (Device1) will be discussed in the following.

5.2.1 Device 1

In this device graphene junction is 3 µm by 3 µm in size. Fig. 5.1 shows the plot of G_{2t} versus V_{bg} for different Δz with a bending step size of 0.4 mm. The linear part of the curve around the charge neutrality point(CNP) appears identical on this scale, though there are changes that we discuss in Ch. 6 and we attribute the development of a scalar potential with strain. However, in Fig. 5.1 we find large changes with strain at large carrier densities, a regime in which resistance is typically dominated by the contact resistance, here roughly

from $|V_{bg}| \sim 1$ V . The inital part of the curve around CNP will be further analysed in the upcoming section to extract the field effect mobility. The dip feature in the hole side at $V_{bg} \sim$ -1.3 V vanishes with tensile strain (ε_{xx}) and is reproducible in strain, can be seen in the straining and unstraining cycle in Fig. 5.1(a),(b). This latter effect we tentatively attribute to local strain fluctuations which might result in a different offset doping and can be tunable with strain. The effect observed from $|V_{bg}| \geq 1$ V seems independent of this feature.

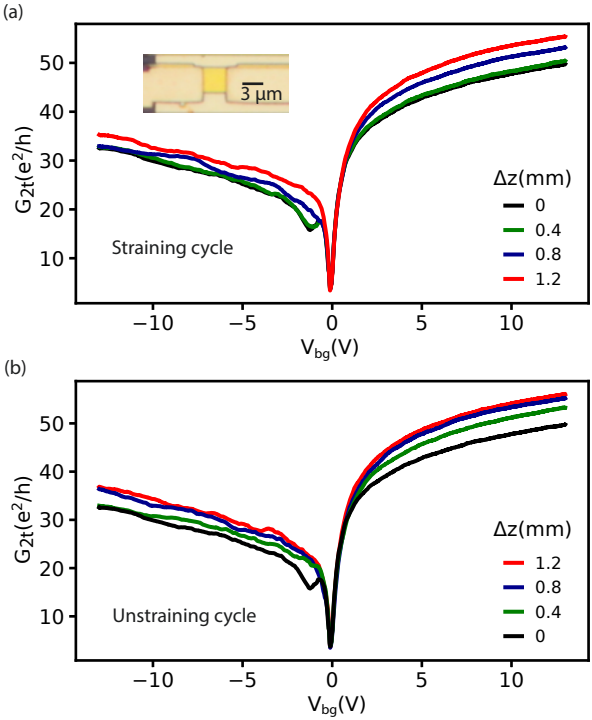

Figure 5.1 G_{2t} versus V_{bg} for different Δz. (a) G_{2t} versus V_{bg} measurement of straining cycle(bending) in Devcie 1. The inset shows the optical image of device junction with hBN encapsulated graphene channel which is edge contacted at the source and drain contacts. Towards higher gate voltage,G_{2t} increases with Δz. **(b)** G_{2t} versus V_{bg} measurement of unstraining cycle(unbending) in Device 1.

The G_{2t} shows 20-30% increase at higher V_{bg} with bending distance (Δz) of

around 1.2 mm. The change in G_{2t} with Δz is reversible as can be seen in both straining and unstraining cycle (Fig. 5.1(a),(b)). On comparing the straining and unstraining cycle, the change in G_{2t} between $\Delta z = 0$ and $\Delta z = 1.2$ mm is similar within 1-2% change. In Fig. 5.1(a),(b) at intermediate bending steps it can be seen that the curves corresponding to same Δz in the bending and unbending cycle differ from each other and can be due to the mechanical hysteresis at the edge contact or the hysteresis with the bending of substrate.

Mechanical breaking of Graphene-metal contact

Beyond a certain bending distance, the forces on the edge contacts results in mechanical failure, which we characterised seperately in Raman experiments, in which a sudden relaxation to the unstrained Raman signal occured [91]. In another strain cycle of measurement in Device 1 shown in Fig. 5.2, the device junction upon bending by $\Delta z = 1.8$ mm lead to suppression in conductance at $V_{bg} > 1$ V compared to the curve at $\Delta z = 1.6$ mm. Further at $\Delta z = 2$ mm the device junction stopped conducting. The initial suppression in conductance at $\Delta z = 1.8$ mm can be an indication that the metal-graphene bond started to slip, with the precursor of a reduced conductance even before the device failure and followed by the complete mechanical breaking of metal-graphene junction at $\Delta z = 2$ mm. We believe that in this mechanical breaking up, the chemical bonds get significally elongated, with a corresponding reduction in the wavefunction overlap and a strong reduction of the conductance. This is the regime that is easily understood intuitively. However, this regime is rather hard to stabilize in the experiments and larger hysteresis occur. In the following, we will only investigate clearly smaller bending and strain values to avoid such problems.

Comparing two terminal and four terminal differential conductance

The change observed in Device 1 towards higher gate voltage, we consider it an effect from the edge contacts. Device 1 is a two terminal junction, so we cannot compare it to the four terminal measurement in the same device to see whether it's really an effect from metal-graphene edge contact. Fig. 5.3(a),(b) compares the two terminal and four terminal differential conductance in a bilayer graphene (BLG) hall bar device. The inset of Fig. 5.3(a) shows the optical image of the device. The two terminal conductance is measured by passing a current from contact 1 to 4 and measuring voltage between contact 1 and 4. The four terminal conductance is measured by passing a current from contact 1 to 4 and measuring voltage between contact 2 and 3. Eventhough BLG is different from single layer graphene in terms of bandstructure, towards higher carrier density the two terminal differential conductance saturates to

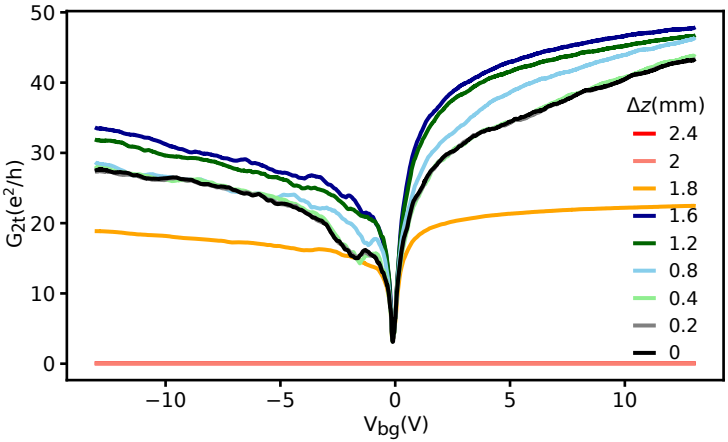

Figure 5.2 Mechanical breaking of edge contact at higher Δz. At Δz larger than 1.6 mm the contacts started to become more resistive ,most probably from the start of slipping of edge contacts and at Δz = 2 mm the contacts have mechanically detached.

the value of contact resistance. In Fig. 5.3(a), towards higher gate voltage there is an increase in two terminal conductance with Δz, a similar effect observed in Device 1. In four terminal measurement, shown in Fig. 5.3(b), most of the curves almost overlapp each other but few show changes which are not monotonic in Δz. The black curve at Δz = 0 almost lie on top of red curve at Δz = 1 mm. Thus it seems the changes observed at higher gate voltage in two terminal measurements is related to the effect of strain on source/drain metal - BLG edge contact than in the bulk of BLG. So we consider the effect at higher gate voltage with Δz to be also the same in graphene.

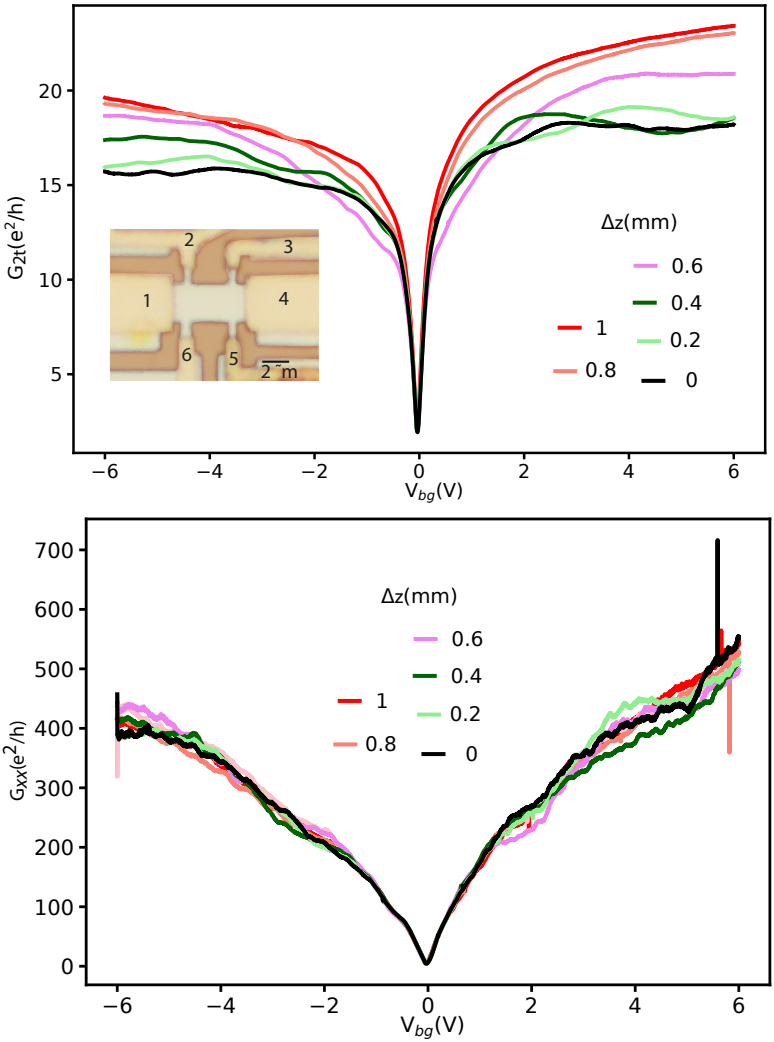

Figure 5.3 Comparison of four terminal and two terminal mesurement in a bilayer graphene hall bar device.(a) Two terminal differential conductance versus back gate voltage(V_{bg}) in bilayer graphene hall bar device. The inset shows the optical image of the device. **(b)** Four terminal differential conductance versus back gate voltage(V_{bg}) in bilayer graphene hall bar device.

5.3 Modeling the conductance change

To understand the changes in G_{2t} at higher V_{bg}, two models will be discussed in the following based on diffusive and ballistic transport. The same procedures in the model can be followed for the analysis of hole and electron side of the G_{2t} versus V_{bg} plot. For the following discussion electron side ($V_{bg} >$ 0 V) of the measurement of Device 1 will be looked with diffusive and ballistic model. These two models describe transport in two different regimes, account differently for low-density conductance, but make no difference for large density. At last both models will result in a similar interpretation.

5.3.1 Diffusive model

The total resistance of two terminal graphene junction can be written as ,

$$R_{total} = R_{gr} + R_s \tag{5.1}$$

$$R_{total} = 1/G_{2t} \tag{5.2}$$

$$R_s = R_{Gr-M} + R_{line} \tag{5.3}$$

where G_{2t} is the measurement data(plotted in Fig. 5.1(a)), R_{gr} is the graphene channel resistance, R_s is the series resistance that includes the resistance from graphene-metal contact resistance(R_{Gr-M}) and the line resistance(R_{line}) of the cryostat. The line resistance from the strain setup I is, $R_{line} \approx 380\ \Omega$ with an uncertainity due to temperature gradient in the cryostat. In the diffusive limit, the graphene conductance can be written as

$$G_{gr} = \frac{\sqrt{(n^2 + n_0^2)}e\mu}{\alpha_g} \tag{5.4}$$

$$n = c_g(V_{bg} - V_{cnp}), \tag{5.5}$$

where n_0 is the residual density, $\alpha_g = L/W$ accounts for the device geometry, $c_g = C/A$ (Eq. 2.28) is the geometrical gate capacitance per unit area, μ is the field effect mobility and V_{cnp} is charge neutrality point (CNP) in V_{bg} axis at which G_{2t} is minimum. In G_{2t} versus V_{bg} curve in Fig. 5.1, the initial linear part of conductance around V_{cnp} indicates constant mobility from Drude model of conductivity as discussed in subsec. 2.3.2. The conductance in this linear regime is dominated by graphene channel as at low carrier density graphene resistance is high.

The zoom in of the curve shown in Fig. 5.4(b),(c) shows the minimum conductance region exhibits conductance oscillations. The transport around the CNP for $n < n_0$ is dominated by charge puddles [50] and interpolated by the square root expression. The oscillations can be an effect of scattering resonances from

such disorderd potential energy landscape. The presence of conductance oscillations around CNP makes the mobililty fit difficult as Eq. 5.4 doesn't account for it. In the following two methods used to estimate μ is discussed and further can be used to make a comparison for the R_s obtained using μ extracted from both methods.

$$R_s = R_{total} - R_{gr} \tag{5.6}$$

In the diffusive model, a constant mobility independent of charge carrier density is assumed for graphene device junction.

Method 1

The fit for conductance around V_{cnp} with Eq. 5.4 is used to estimate μ and n_0. Fig. 5.4(b) shows the fit to the data at $\Delta z = 0$ mm. The fit parameters μ and n_0 obtained for different Δz is shown in Fig. 5.5. The V_{cnp} from the minimum position of G_{2t} in V_{bg} axis , shifts more to the negative V_{bg} with increasing Δz which can be attributed to the strain induced scalar potential and it will be discussed in detail in Ch. 6.

Method 2

The presence of conductance oscillations at CNP makes the fit for μ difficult with Eq. 5.4. So the region close to CNP but away from the oscillations is chosen to make a linear fit to obtain μ.

$$G = c_g(V_{bg} - V_{off})e\mu + G_{offset} \tag{5.7}$$

where $G_{offset} = 7.8$ e^2/h, is the offset in conductance above which the linear fit is made with Eq. 5.7. The lever arm of the device junction, $\mathrm{c_g} = 2.24 \times 10^{15}$ $\mathrm{CV^{-1}m^{-2}}$. Fig. 5.4(c) shows the fit (green dashed line) to the linear section above the region of oscillations, $G_{2t} > 7.8$ $\mathrm{e^2/h}$. V_{off} is defined to be the V_{bg} at which G_{2t} is above the oscillaton region. The V_{off} lies around 0.022 V for all the curves within the range of $\pm$ 3 mV except for the curves at $\Delta z =$ 0.6 mm, 0.8 mm where V_{off} lies around 0.035 V. The electron density(n) at these respective V_{off} is larger than the residual density from the electron-hole puddles (n_0), where $n_0 \sim 1.35 \times 10^{10}\mathrm{cm^{-2}}(\pm\ 1\times\ 10^{9}\mathrm{cm^{-2}})$ from method 1.

Fig. 5.5(a) compares the mobility(μ) extracted from both the above methods and these two sets are used to obtain series resistance(R_s) using Eq. 5.6.

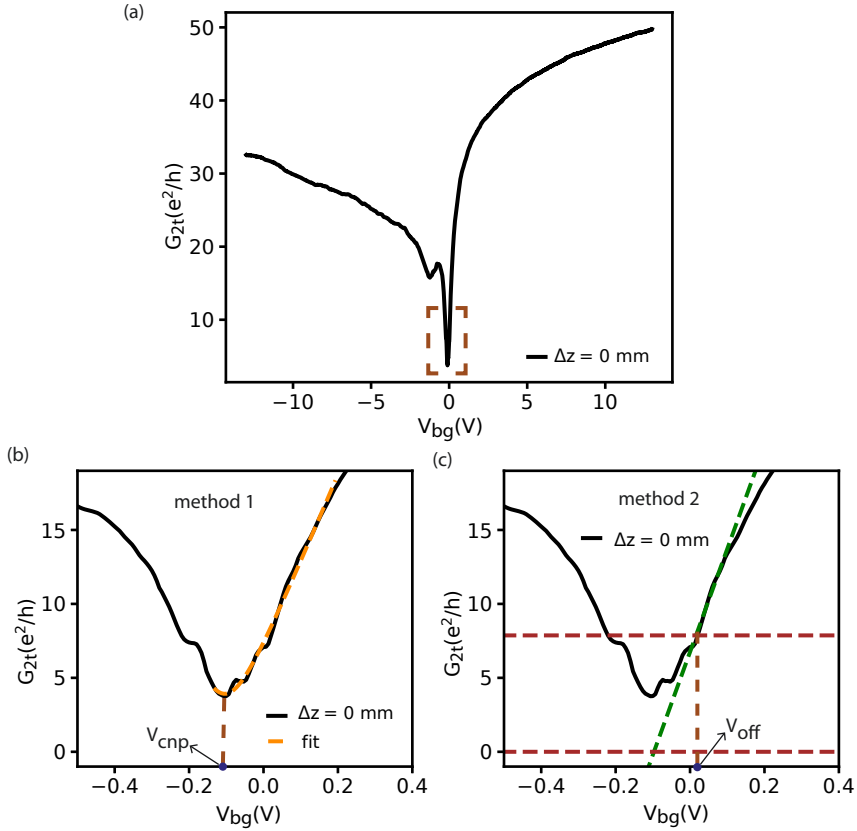

Figure 5.4 Extracting field effect mobility (a) G_{2t} versus V_{bg} for Δz = 0 mm. The initial linear part of the curve is fitted with two methods as shown in the zoom in of the curve in brown dotted box. **(b)** Fit with method 1 discussed using Eq. 5.4. **(c)** Fit with method 2 using Eq. 5.4. The linear part of the curve after the conductance oscillation is fitted for $G_{2t} > 7.8$ e^2/h.

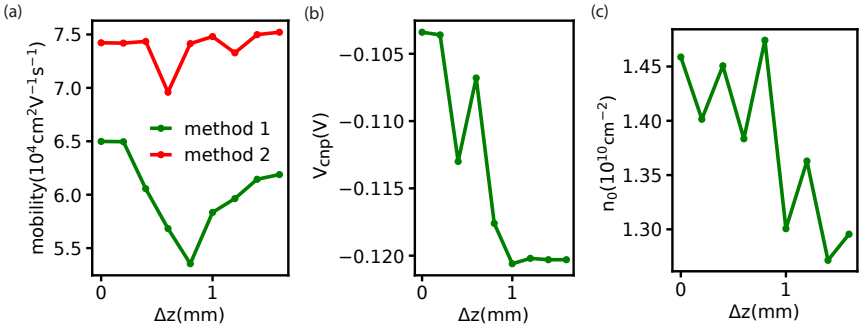

Figure 5.5 Fit parameters in the diffusive model (a) Plot compares the mobility extracted from method 1 and 2 for different Δz. The presence of conductance oscillations around CNP makes the slope of the fit smaller in method 1 compared to that extracted for the linear part after the oscillations in method 2. **(b)** V_{cnp} from the minimum position of G_{2t} in V_{bg} axis. Overall V_{cnp} shows a decrease with Δz. **(c)** The residual density, n_0 from the fit with method 1. The conductance oscillations around CNP makes the fit around it to be not good and affects the extraction of n_0.

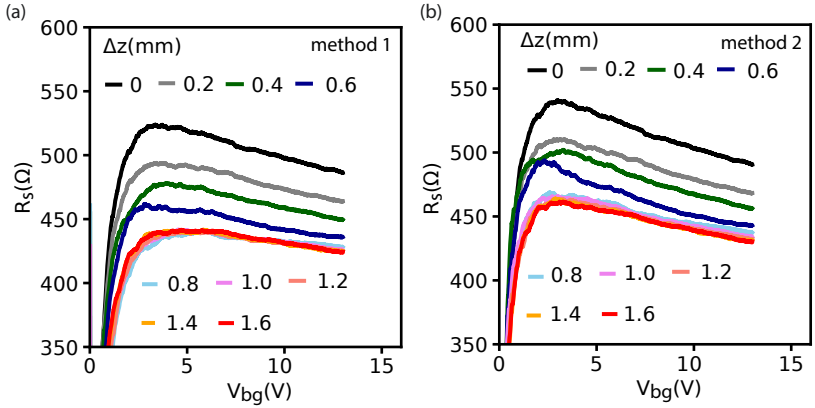

Figure 5.6 Series resistance,R_s (a) The series resistance(R_s) obtained with Eq. 5.6. $R_{gr} = 1/G_{gr}$ (Eq. 5.4) calculated for $V_{cnp} < V_{bg} < 13$ V with μ and n_0 obtained from the fit around CNP in method 1. **(b)** The series resistance(R_s) obtained with Eq. 5.6 using $R_{gr} = 1/G$ (Eq. 5.7) with μ from fit in method 2. R_{gr} is calculated for $V_{off} < V_{bg} < 13$ V with μ from the linear fit above V_{off}.

Series resistance(R_s) from method 1 and method 2

The series resistance, R_s is obtained using Eq. 5.6, $R_s = R_{total}$ - R_{gr}, where $R_{total} = 1/G_{2t}$ (G_{2t} is the measured data).

For method 1, $R_{gr} = 1/G_{gr}$ (Eq. 5.4) is calculated for $V_{cnp} < V_{bg} < 13$ V with μ and n_0 obtained from the conductance fit around CNP in method 1(subsec. 5.3.1). For method 2, $R_{gr} = 1/G$ (Eq. 5.7) is calculated for $V_{off} < V_{bg} < 13$ V with μ obtained from linear fit in method 2.

Fig. 5.6 shows R_s versus V_{bg} from method 1 and method 2. In both the cases R_s decreases towards higher V_{bg}. Also R_s decreases with Δz. We find that we need parameters to describe the curves reasonably accurately, so we introduce dependence in the spirit of a Taylor expansion in V_{bg} of the initial properties. On Taylor expanding R_s in V_{bg} for method 1 and method 2 described above we get,

$$\begin{aligned} R_s &= R_{s0} + a \cdot (V_{bg} - V_{cnp}) \quad (for \;\; method1) \\ R_s &= R_{s0} + a \cdot (V_{bg} - V_{off}) \quad (for \;\; method2) \end{aligned} \tag{5.8}$$

where "a" is the coefficient of Taylor expansion for the dependance in V_{bg}, V_{cnp} and V_{off} are offsets in V_{bg} which are taken correspondingly from method 1, method 2 described above in subsec. 5.3, R_{s0} is the intercept on the y-axis in the plot. Fig. 5.7(a),(b) shows the linear fit to R_s using Eq. 5.8 for different Δz (distance moved by wedge to bend the substrate, illustrated in Fig. 3.8).

The inset of Fig. 5.7(c),(d) shows the comparison of R_{s0} and "a" obtained from method 1 and method 2. R_{s0} decreases with Δz as well as the magnitude of slope "a" decreases with Δz. The decrease of slope a with Δz implies that series resistance becomes less dependent on V_{bg}. Upto Δz = 1 mm, both R_{s0} and "a" show large change and for Δz > 1 mm there is no significant change in both parameters. This is captured by the plot of ΔR_{s0} versus Δz and Δa versus Δz in Fig. 5.7(c),(d). The description for ΔR_{s0}, Δa is given below:

The change in R_{s0}, $\Delta R_{s0} = R_{s0}(\Delta z)$ - $R_{s0}(\Delta z = 1.6$ mm) is plotted against Δz in Fig. 5.7(c). It shows that change in R_{s0} saturates towards Δz > 1 mm. The change in a, $\Delta a = a(\Delta z)$ - $a(\Delta z = 1.6$ mm) is plotted against Δz in Fig. 5.7(d). It shows that the slope a saturates towards Δz > 1 mm and the series resistance R_s becomes more independent of V_{bg}. The series resistance R_s, described in subsec. 5.3.1 includes graphene-metal contact resistance(R_{Gr-M}) and the line resistance(R_{line}) of the cryostat. R_{line} is $\approx 380\ \Omega$, is a constant. So the changes observed in R_s, we consider it to be in R_{Gr-M}.

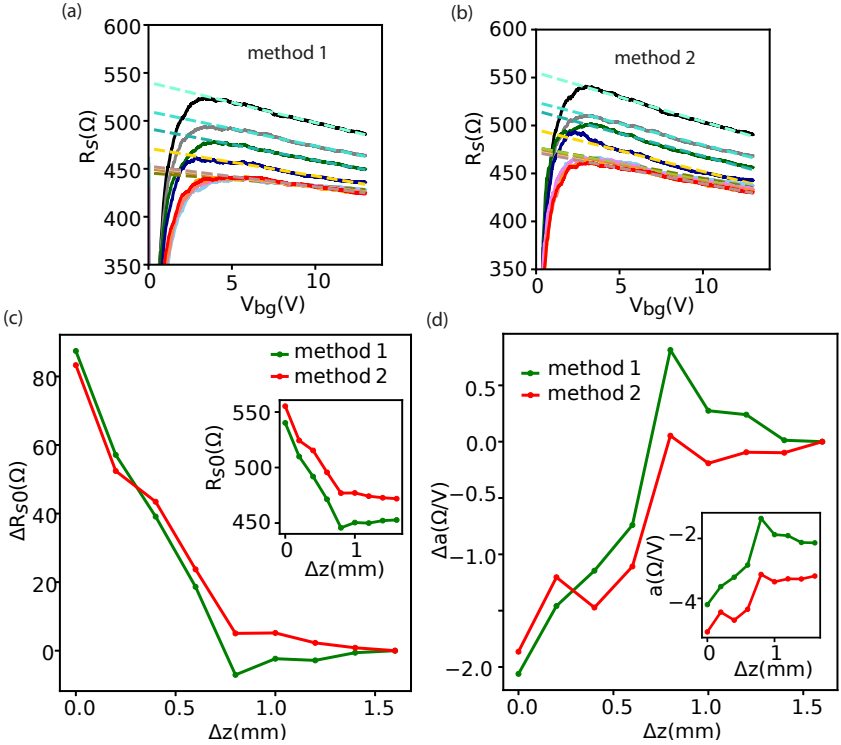

Figure 5.7 Linear fit to R_s. (a),(b) R_s obtained from both method 1 and 2 decreases with V_{bg} and is linear in the range 5 V < V_{bg} < 13 V. The dashed lines on top of the curves are the corresponding linear fit to it. The solid lines corresponds to the same data plotted in Fig. 5.6. **(c)** The inset shows intercept (R_{s0}) of the fit along the axis of R_s plotted against Δz. The change in R_{s0} is plotted against Δz where $\Delta R_{s0} = R_{s0}(\Delta z)$ - $R_{s0}(\Delta z = 1.6$ mm). **(d)** The inset shows the slope of the linear fit, "a" versus Δz for both method 1 and 2. The change in slope , Δa is plotted against Δz where $\Delta a = a(\Delta z)$ - $a(\Delta z =$ 1.6 mm).

Upon increasing Δz, that is increasing strain in the device, R_{Gr-M} decreases and also it becomes less dependent on V_{bg}. The change in R_{Gr-M} with strain can be an effect on the chemical bonds at the metal-graphene interface but not conclusive enough.

5.3.2 Ballistic model

The mean free path (l_{mfp}) of the system with the mobility (μ) estimates from diffusive model (subsec. 5.3.1) reaches around 0.5 μm at $V_{bg} \sim 2$ V, using $l_{mfp} = (\hbar\mu\sqrt{n\pi}/\mathrm{e})$. The width of the junction in Device 1 is, $W = 3$ μm. Thus at higher carrier density l_{mfp} becomes more closer to W and the charge carriers can exhibit ballistic transport in the device. In this section we introduce a ballistic transport model to model the effect of Δz (distance moved by wedge to bend the substrate, illustrated in Fig. 3.8) on the two terminal differential conductance (G_{2t}).

In ballistic transport [103], transmission probability for a channel (T) is the factor that accounts for scattering or reflections occuring at contacts as the channel itself have zero resistance as discussed in subsec. 2.3.3.

$$G_{2t} = \frac{1}{\frac{1}{G_{bal}} + R_{line}} \tag{5.9}$$

where R_{line} is the line resistance of the cryostat, $R_{line} \approx 380\ \Omega$.

$$G_{bal} = \frac{4e^2}{h} T \cdot W \cdot M \tag{5.10}$$

where M is the number of modes, given by $M = \sqrt{n/\pi}$ and n is the charge carrier density. Each mode is 4-fold degenerate from spin and valley degeneracy in graphene, discussed in Ch. 2. The conductance model discussed in subsec. 2.3.3 for ballistic transport considering finite temperature in the reservoirs and the ballistic conductance from Eq. 5.10 gives same plot for G_{bal} versus V_{bg} for a given transmission (T), T_{bath}(temperature) = 4.2 K and $W = 3$ μm as shown in Fig. 2.4. The transport experiments are carried out at 4.2 K, so Eq. 5.10 is good enough to quantify the ballistic conductance at 4.2 K for such wide junctions.

$$n = c_g(V_{bg} - V_{off}) \tag{5.11}$$

where V_{off} is the same as used in Method 2 of diffusive model, $W(= 3\ \mu\mathrm{m})$ is the geometrical width of junction and n is the charge carrier density.

In Eq. 5.9, T is the only fit parameter and the fit for G_{2t} versus V_{bg} curve is not good, as shown in Fig. 5.8(a). The fit doesn't follow the slope of G_{2t} in

V_{bg}, especially at higher V_{bg} (> 5 V). With introducing a gate voltage dependent transmission: $T = T_0 + \alpha(V_{bg} - V_{off})$, the ballistic model fit becomes better with T_0 and α as the fit parameters, see Fig. 5.8(b),(c). Ballistic model fit fails at low carrier density in graphene as the model suggest an infinite slope of the conductance curve around charge neutrality point(CNP). The conductance around CNP is more like in the diffusive regime where the ballistic model doesnot fit well.

We perform such a fit for each curve seperately for a series of bending or strain values, with two examples shown in Fig. 5.8. The fit parameters T_0 and α obtained from the fit for each Δz is plotted in Fig. 5.9(a),(b). The line resistance of the cryostat, $R_{line} \approx 380\ \Omega$. Also, plotted T_0 and α from the fit with R_{line} deviating about $\approx 380\ \Omega$. But the dependance of T_0 and α on Δz remains same eventhough the absolute value changes. T_0 shows an overall increase with Δz except it slightly deviates around $\Delta z = 0.5$ mm. The gate voltage dependance of T, that is α increases initially with Δz and further saturates towards $\Delta z > 0.5$ mm. So, T increases with Δz which indicates the transmission of carriers at the metal-graphene edge contact interface increase with strain. The increase in transmission can be an effect of strain on the bonds at the metal-graphene edge contact but not conclusive to avoid other strain affects at the contacts that might be present.

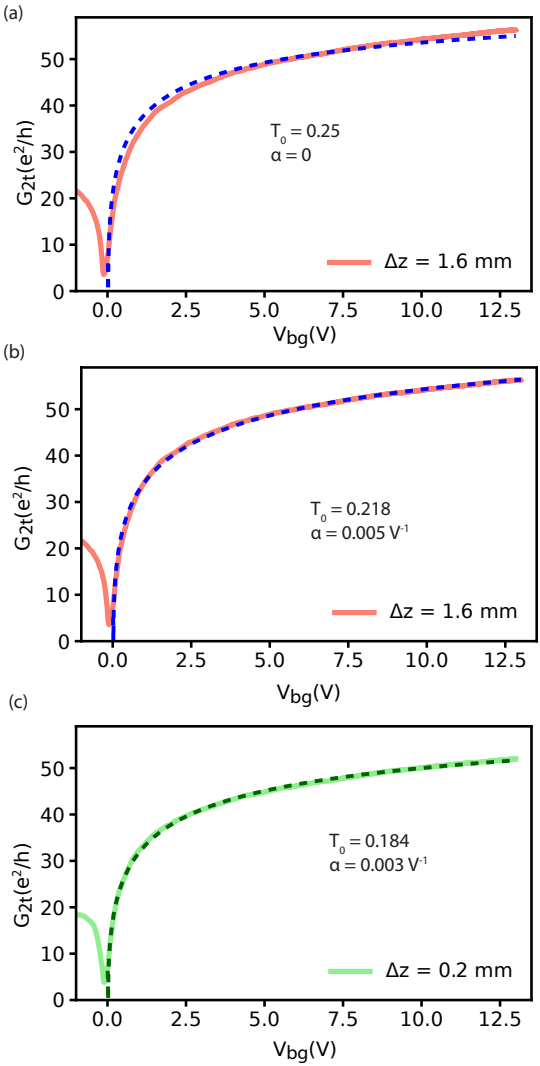

Figure 5.8 Fit with ballistic model. The solid lines are the data and the dashed line on top is the fit curve. **(a)** Ballistic model fit using Eq. 5.9 with T as the only fit parameter for the data at bending distance $\Delta z = 1.6$ mm.**(b)** Ballistic model fit with parameters T_0 , α for the data at $\Delta z = 1.6$ mm.**(c)** Ballistic model fit with parameters T_0 , α for the data at $\Delta z = 0.2$ mm.

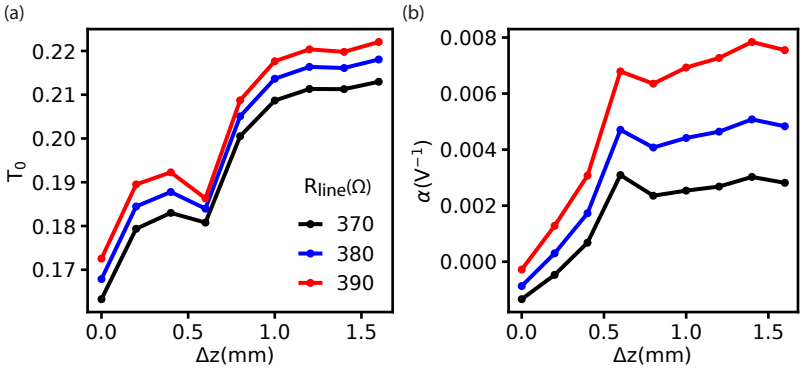

Figure 5.9 Fit parameters in ballistic model. (a) T_0 extracted for different Δz from the ballistic model fit shown in Fig. 5.8. The line resistance(R_{line}) of the system from measurement is $\sim 380\ \Omega$. T_0 versus Δz for slight deviations from R_{line} is also plotted. **(b)** The factor for the gate voltage dependance of transmission, α extracted from ballistic model fit for different Δz. Also α versus Δz for slight deviations from R_{line} is plotted, the color of each curve corresponds to the same R_{line} in (a).

5.4 Discussion

The increase in G_{2t} with Δz is accounted by decrease in contact resistance (R_{Gr-M}) in the diffusive transport model and by an increase in transmission (T) in the ballistic transport model. In this section we will look into the effects strain can have on a graphene device junction and see if it can explain the observations from the diffusive and ballsitic model.

5.4.1 Strain effect on geometry

Strain changes the lattice dimensions, thus length (L) and width (W) of the device depends on strain (ε). The effect of these geometrical changes in diffusive and ballistic model will be discussed in this section.

In the diffusive model, geometric factor $\alpha_g = L/W$ can change with ε. For ε acting along the length of junction,

$$\alpha_g(\varepsilon) = \frac{\mathrm{L}(1+\varepsilon)}{\mathrm{W}(1-\nu\varepsilon)} \tag{5.12}$$

where ν (=0.16) is Poisson ratio of graphene [104]. We extract the parameters in the diffusive model (data : yellow curve and fit : blue dotted line)

for conductance data at $\Delta z = 0$, see Fig. 5.10. The geometric factor, α_g corresponding to $\varepsilon = 1\%$ is calculated with above equation and along with parameters obtained from the fit for conductance at $\Delta z = 0$ is used to plot the green dotted line curve, almost identical to data and fit at $\Delta z = 0$. The red curve is the data at $\Delta z = 1.6$ mm, that is at a higher strain than at $\Delta z = 0$. This concludes that changes in α_g doesn't account for the change in conductance observed upon increasing Δz.

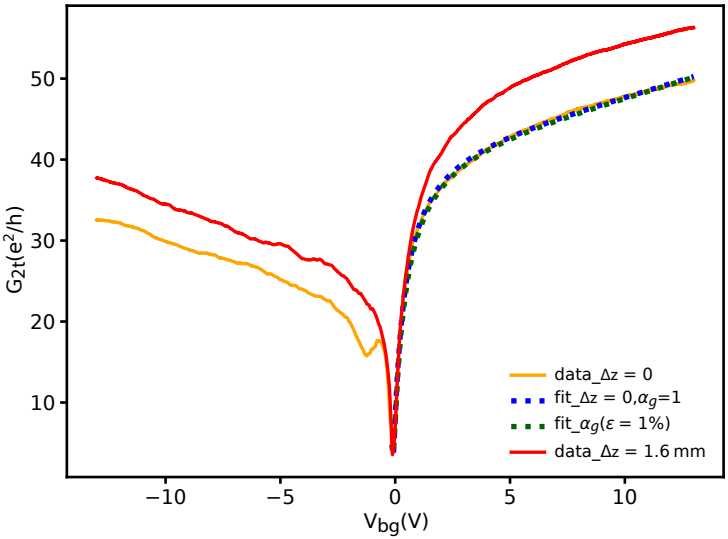

Figure 5.10 Strain effect on geometry in the diffusive model. Considering 1% strain in the graphene junction, geometrical factor α_g changes by 1.16%. The orange and red curve are the data at bending distance $\Delta z = 0$, 1.6mm. The blue dotted curve is the fit to orange curve and the green dotted curve is the fit function plotted with $\alpha(\varepsilon$=1%). The change in α_g alone doesn't bring the effect to reach the G_{2t} versus V_{bg} curve at $\Delta z = 1.6$mm.

In ballistic model, geometry of the junction enters via the width (W) of the junction (Eq. 5.9). Uniaxial tensile strain (ε) along the junction length can decrease W : W(ε) = W(1-$\nu\varepsilon$) as discussed in Eq. 5.12. But the effect due to it is small and also the decrease in W with ε should decrease G_{bal} and thereby the total G_{2t}. So the increase in G_{2t} with Δz observed doesn't seem to orginate from geometrical change also in ballistic model.

5.4.2 Strain effects at metal-graphene interface

There can be changes in graphene by strain, in the metal-graphene interface, and in the metal. The changes in graphene with strain include change in mobility(μ), geometry change, aslo the strain effects in graphene(discussed in Ch. 2) : Fermi velocity anisotropy, scalar potential, magnetic vector potential. Overall mobility didn't changed much on comparing between $\Delta z = 0$ and $\Delta z = 1.6$ mm (Fig. 5.5). The effect of strain on geometry also doesn't lead to an observable change in conductance as shown above. Also we are not in the regime where bond elongation becomes very strong which might lead to plastic deformations. This leaves us with metal-graphene interface.

Possibility of barriers at metal-graphene interface

In diffusive model, R_s shows dependance on V_{bg}, shown in Fig. 5.6. Also V_{bg} dependant T makes the fit better in ballistic model, Fig. 5.8. The dependance of R_s and T on V_{bg} can be an effect from :

(a) tunnel barrier between the graphene and metal Cr/Au forming the edge contact [105]. In the process of fabricating edge contacts, mixture of CHF_3 and O_2 gas is used for plasma etching of hBN/Graphene stack which can lead to edge contact to get terminations from O, F atoms [106].

(b) a potential barrier at the contact region can arise between graphene close to contact and in the bulk [107]. The work function difference between Cr/Au and graphene can lead to transfer of charge carriers at the interface to equilibriate the fermi level of the two system. The presence of such potential steps can make conduction in electron and hole side asymmetric [108]. Asymmetry in the conductance of electron and hole side observed in Device 1 (Fig. 5.1), can be due to the existense of such potential barriers at the contact region.

Effect of strain on barriers at the metal-graphene interface

The effect of strain on such barriers can come through :

(a) From the effect of strain induced scalar potential, discussed in Ch. 2 (will be discussed in detail in Ch. 6), might result in a change in the potential step at the metal-graphene interface, which in turn might result in changes in the contact resistance or transmission at the interface.

(b) Momentum mismatch along the interface of the barrier [39, 78] can also control the transmission across the interface. Strain in graphene can result an effective magnetic vector potential which can change the Fermi surface overlap

between the graphene near the contact and in the channel, thereby can change transmission [78].

Effect of strain on the chemical bonds at the interface

It can also be an effect from the chemistry of orbital overlap at the metal-graphene interface. Increasing the bond distance between atoms at the interface results in reduced orbital overlap. Beyond a certain distance from equilibrium the transmission decreases exponentially, approaches a tunnel barrier behaviour, reported in Ref. [105]. But we are far below the mechanical break limit. Or it can be that with strain, states which were gapped at interface before might come closer as strain decreases the interaction between atoms and make available more states for tunneling or conduction at the interface before the mechanical break limit. Effect of stretching bonds resulting in increased coductivity observed in some break junction based devices is repored in Ref. [109], based on the rearrangement of energy levels.

5.5 Summary

The effect of increase in two terminal conductance with bending is discussed. The bending induced monotonic changes at higher gate voltage are present in two terminal junction, absent in four terminal device junction implying the changes are from the metal-graphene interface. Under the assumption of a constant mobility independent of charge carrier density, the change observed corresponds to the change in contact resitance in the diffusive transport model or transmission of the Cr/Au-graphene interface in ballistic transport model. The contact resistance decrease with bending in the diffusive transport model whereas transmission increase with bending in the ballistic transport model. Both model suggest less interface resistance with more bending. This is counter intuitive, but we are far from the mechanical break limit of the interface, so that other effects might dominate. We propose that changes in the graphene potential are the dominant factor in this regime, possibly related to the scalar potential, which might result in a change in the interface potential step. Alternatively, a momentum mismatch at a potential barrier can also lead to changes in transmission. Can chemistry of the bonds at the interface play a role in decreasing the interface resistance is still a question?. So,the exact mechanism responsible for the effect is not known yet other than the speculations.

The effects related to metal-graphene interface appearing in two terminal measurements only dominate at higher gate voltage and the effect of it at the low gate voltage (around charge neutrality point (CNP)) features in conductance can be neglected where the graphene or bilayer graphene channel conductance play the dominant role. Also in four terminal measurements, bending induced

effect on source/drain metal-graphene interface observed below the mechanical break limit will not affect it as it probes the bulk of graphene or bilayer graphene away from the source/drain contacts.

6 Scalar potential

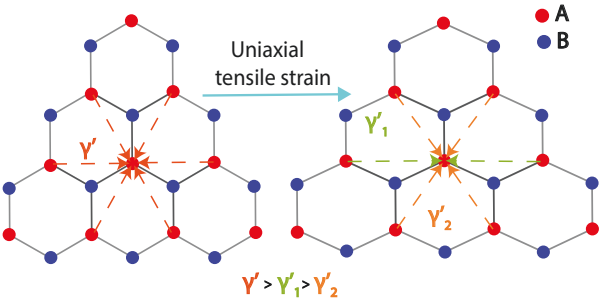

This chapter discusses the scalar potential induced by strain in graphene and similar effects observed in bilayer graphene. The scalar potential describes the changes happening in the next nearest neighbour (nnn) hopping[1] which is equivalent to change in an on-site energy on the same sublattice because nnn connects crystallographically equivalent sites. Further, we define scalar potential constant (s_0) that describes how much the energy of the system decreases with a change in tensile strain. In principle this is a general effect of strain and should also be observable in other crystal lattices. The first section follows our published work [35] on the strain induced scalar potential in single layer graphene. The next section discusses the similar related effects in bilayer graphene.

[1] Schematic illustration of changes in next nearest neighbour hopping under uniaxial tensile strain in graphene.

6.1 Introduction

Hopping parameters in the tight binding bandstructure calculations are sensitive to bond distance between the atoms [36]. Upon straining the crystal lattice in a controlled way can potentially control the hopping amplitude. In graphene lattice, Fermi velocity (v_f) of charge carriers is directly related to nearest neighbour hopping (γ_0). Under uniaxial tensile strain, v_f becomes anisotropic [110]. In terms of the energy band structure it appears as an effect of changing the fermi surface of graphene from circular to elliptical [111].

At the same time, next nearest neighbour hopping (γ') is also modified with strain and the hopping is between the same sublattice type A-A, B-B. The new dispersion relation with next nearst neighbour hopping included reads [43],

$$E_{\pm}(\vec{k}) = 3\gamma' - (\frac{9\gamma' a^2}{4} \pm \frac{3\gamma_0 a^2}{8}\sin(3\theta_k))\hbar^2|k|^2 \pm \hbar v_{\mathrm{F}}|\vec{k}|, \tag{6.1}$$

where $\theta_k = tan^{-1}(\frac{k_x}{k_y})$, is the angle in momentum space. In addition, γ' makes the dispersion electron-hole asymmetric because at $k = 0$ it can be seen that dirac point is shifted in energy by the term $3\gamma'$. As γ' reduces with tensile strain, the dirac point downshifts as can be seen from Eq. 6.1. This shift is reffered to as strain induced scalar potential and can be understood as a reduction in on-site energy of sublattice atoms.

Bilayer graphene (BLG) is an exciting system in which the interlayer interactions play a important role in its band structure. The band structure is parabolic at lower momenta values [40]. This results in charge carriers to have mass in BLG which is absent in graphene. BLG can potentially be more sensitive to strain due to the interlayer interaction, as the bandstructure is sensitive to it. The effect of scalar potential should also be observable in BLG as it is a general effect of strain acting on a lattice.

In this chapter we will discuss the effects of strain induced scalar potential in graphene [35] and bilayer graphene followed by an estimate for scalar potential constant in the two systems.

6.2 Strain induced scalar potential in graphene

This section presents the findings based on the measurements carried out in two terminal graphene junction of square geometry under tensile strain. We have published the results discussed in this section in Ref. [35]. The transport measurements were carried out in strain setup I described in detail in Sec. 3.2. The strain in this device is first characterised with bending setup for Raman

spectroscopy (subsec. 3.2.2) at room temeprature. More on the details of the spatial Raman mapping on graphene device junction is discussed in Ch. 8. The strain callibration with the distance moved by wedge to bend the substrate (Δz) for the device is shown in Fig. 6.1. The bending of the substrate is schematically illustrated in Fig. 3.8 with Δz labelled. Increasing Δz will lead to increase in average tensile strain ($\bar{\varepsilon}$) over the junction. Upon bending the substrate by Δz = 1 mm resulted in a redshift of 14.2 rel.cm^{-1} of the average 2D Raman peak position ($\bar{\omega}_{2D}$) over the square device junction,shown in Fig. 6.1(a). Further this shift rate is converted in terms of strain as discussed in subsec. 2.5.3 using $\frac{\partial \bar{\omega}_{2D}}{\partial \bar{\varepsilon}}$ = -54cm^{-1}/% strain [74]. From this, Δz = 1 mm corresponds to $\bar{\varepsilon}$ = 0.265%, see Fig. 6.1(b). The same callibration curve is used to estimate strain in the device junction for the low temperature transport measurements with strain as tuning knob. The two terminal differential conductance (G_{2tml}) as a function of gate voltage (V_{bg}) is recorded for different Δz (or $\bar{\varepsilon}$) in the graphene junction as shown in Fig. 6.2. The linear fit around

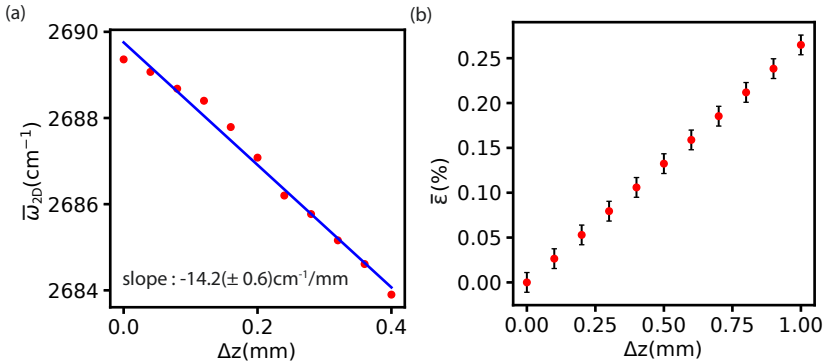

Figure 6.1 Strain characterization in graphene device junction. (a) Spatial average of 2D peak position($\bar{\omega}_{2D}$) shift in the Raman spectrum with bending distance(Δz). Upon bending, graphene junction gets tensile strained and results in a red shift of ω_{2D}. **(b)** Average tensile strain ($\bar{\varepsilon}$) in the junction plotted against Δz. This plot serves as a link between Δz and $\bar{\varepsilon}$ for strain setup I. The conversion of change in ω_{2D} to $\bar{\varepsilon}$ is described in the text above.

charge neutrality point (CNP) as described in subsec. 5.3 (using Method II) gives field effect mobility of $\sim$ 100,000 cm^{2}V^{-1}s^{-1} suggesting that device quality is high. The conductance curves look similar for subsequent steps in strain but the zoom in around the charge neutrality point(CNP) shown in Fig. 6.2(b) shows the changes clearly. The CNP is at positive V_{bg} indicating that the graphene is p-doped.

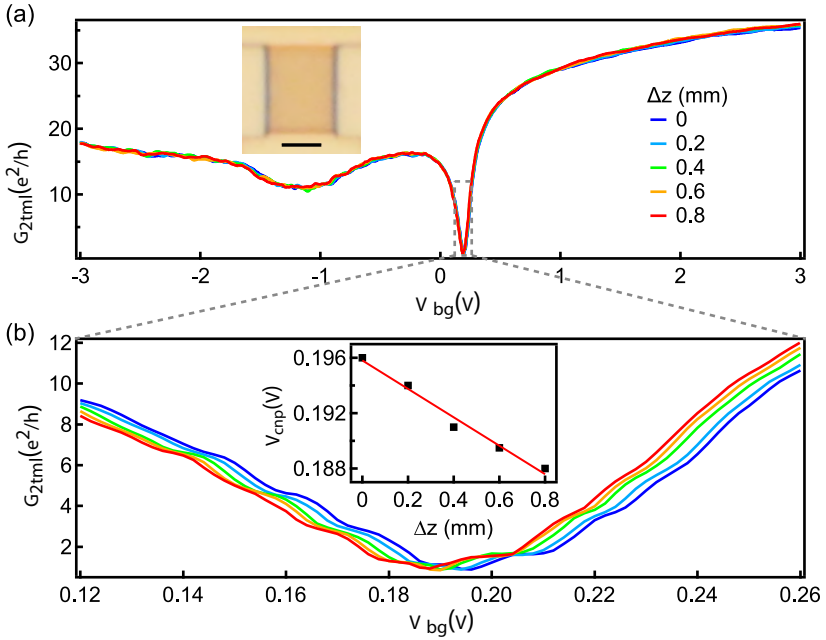

Figure 6.2 Strain induced scalar potential in graphene.(a) G_{2tml} vs V_{bg} curve for different Δz. Inset shows optical image of device, scale bar : 2μm. **(b)** Zoom in to the CNP region of G_{2tml} vs V_{bg} curve. With increase in Δz(increase in strain) V_{cnp} shifts to lower V_{bg}. The inset shows the plot of V_{cnp} vs Δz, V_{cnp} is taken from the position of the minima of G_{2tml} on V_{bg} axis. Figure adapted from our publication,Ref. [35]

The conductance step features seen can be the Fabry-Perot resonances resulting from back scattering at the contact region due to slightly different doping there compared to the bulk of the device junction. The details of the estimation of cavity length is discussed in the supplementary information of Ref [35].

A systematic shift of the CNP towards negative V_{bg} is observed with straining and with repetition of straining cycles the effect remains. The inset of Fig. 6.2(b) shows V_{cnp} plotted against Δz, where V_{cnp} is extracted from the value of V_{bg} corresponding to the minima in G_{2tml}. The tensile strain is low enough ($\bar{\varepsilon} < 0.5\%$), so the change in V_{cnp} can be considered linear in $\bar{\varepsilon}$ as Δz is linear with $\bar{\varepsilon}$ from Fig. 6.1. A linear fit through the points in the inset of Fig. 6.2(b) gives a line of slope $\sim$ 10 mV/mm. We attribute this shift to a change in the scalar potential which we discuss in the next section,susbsec. 6.2.1. In contrast we can exclude a change in gate capacitance (c_g) which would result in a gate voltage dependent shift of conductance curve along the V_{bg} axis which is not the case observed here. A comparison study between suspended graphene device and encapsulated on-substrate graphene device is carried out in Ref. [25] which shows such bending induced changes in gate capacitance is absent in on-susbtrate devices, making the device design suitable for studying strain effects on the charge carrier transport.

6.2.1 Estimation of scalar potential constant in graphene

In this section we try to understand the shift of V_{cnp} observed with Δz (distance moved by wedge to bend the substrate). The strain in the device is proportinal to Δz, as shown in Fig. 6.1. The graphene junction is uniaxially tensile strained (ε_{xx}) in the experiment along the x axis in Cartesian coordinates. The spatial average of the strain over area of the device junction estimated from the shift in $\bar{\omega}_{2D}$ is taken as the effective tensile strain value($\varepsilon_{xx} = \bar{\varepsilon}$) for a given Δz. As introduced in Eq. 2.90 and Eq. 2.91 the total strain for uniaxial tensile strain case is $\varepsilon_t = \varepsilon_{xx} + \varepsilon_{yy} = \bar{\varepsilon}(1\text{-}\nu)$, where ν is the Poisson ratio of graphene [104].

From the $\bar{\varepsilon}$ versus Δz plot in Fig. 6.1(b), Δz = 0.8 mm corresponds to $\varepsilon_t = 0.21\%$. The energy level diagram of graphene device junction at a back gate voltage V_{bg} is shown in Fig. 6.3. The graphene is grounded via the metallic edge contacts and thus fermi level of graphene(E_f) remains same throughout the experiment of straining the device junction. The fermi level of the metallic back gate is denoted by E_f^m. The difference between the electrochemical potential of metallic back gate and grounded graphene junction reads,

$$E_f^m - E_f^{gr} = -eV_{bg} \tag{6.2}$$

The work function difference between metal (W_M) and undoped graphene (W^0_{gr}) results in an electrostatic potential difference (ϕ) with a corresponding charge carrier density in graphene. The low density of states in graphene makes it crucial to take into account the kinetic energy in terms of finite chemical potential (μ_{gr}) and it is measured from dirac point energy (E_D) given by

$$\mu_{gr} = E_D - E_f \tag{6.3}$$

For the unstrained case as shown in Fig. 6.3(a), the quantities can be connected by

$$W_M - eV_{bg} = W^0_{gr} - \mu_{gr} - e\phi \tag{6.4}$$

Upon straining, the dirac point shifts down in energy as shown in Fig. 6.3(b) and the quantities that changed are denoted by a tilde symbol. The shift in E_D lead to an increase in intrinsic work function of undoped graphene from W^0_{gr} to $\widetilde{W}^0_{gr}$. The change in work function of graphene with strain [34, 112, 113] is a direct measure of strain induced scalar potential (S). The two effects in the graphene device due to this are : (a) shift in chemical potential (b) shift of electrostatic potential difference. This in effect causes change in charge carrier density and can be detected in transport experiments. The band allignment quantities for graphene under strain at a gate voltage $\widetilde{V}_{bg}$ is related by

$$W_M - e\widetilde{V}_{bg} = \widetilde{W}^0_{gr} - \widetilde{\mu}_{gr} - e\widetilde{\phi} \tag{6.5}$$

The work function of metals are assumed to remain constant upon straining as it have large density of states. Thus for determining the change in intrinsic work function of undoped graphene, a particular conductance feature is tracked with straining. Here the conductance minima at CNP of graphene can be taken as the feature. For a feature at a given charge carrier density (n), $\widetilde{\mu}_{gr} = \mu_{gr}$ and $\widetilde{\phi} = \phi$ under the assumption that straining doesn't change the back gate capacitance (c_g) as the device junction is strained on-substrate, also discussed above in Sec. 6.2. Upon considering a plate capacitor model between the metallic back gate and graphene with only perpendicular electric field between the capacitor plates, the electrostatic potential difference remaining same for a given n follows from the Gauss law and is given by

$$\int_A D\, dA \; = \int n\, dA \tag{6.6}$$

$$D = \epsilon_0 \epsilon_r E \tag{6.7}$$

$$\phi = \int_0^d E\, dz \; = nd/\epsilon_0\epsilon_r \tag{6.8}$$

where D is the displacement field , E is the effective electric field, d is the back gate dielectric thickness, dA is the small area element of the gaussian surface(considered a cylindrical Gauss box), ϵ_0 and ϵ_r are the free space permittivity and relative permittivity of the medium(hBN dielectric in this case). Thus for a given feature, n remains constant which results in ϕ to be also constant(from Eq. 6.8) and μ_{gr} also remains same as it is directly a measure of n. Upon taking difference of Eq. 6.5 and 6.4 lead to,

$$-(\widetilde{W}^0_{gr} - W^0_{\mathrm{gr}}) = e(\widetilde{V}_{cnp} - V_{cnp}) \tag{6.9}$$

where $\widetilde{V}_{cnp}$ and V_{cnp} are the back gate voltage corresponding to CNP in unstrained and strained case. The strain induced scalar potential(S) is defined as, $S = e(\widetilde{V}_{cnp} - V_{cnp})$. Thus the scalar potential(S) from the experiment is,

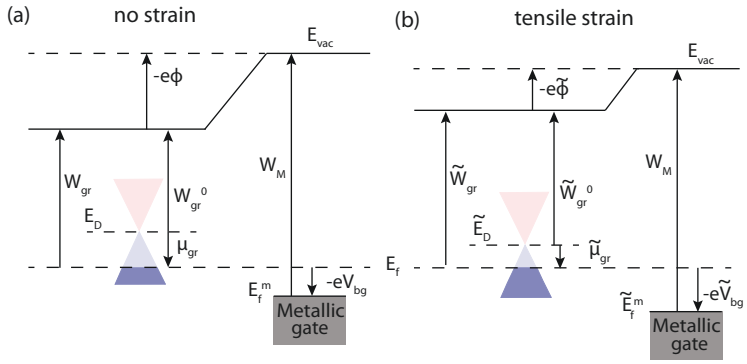

Figure 6.3 Band allignmet schematic for graphene and metallic gate.(a) Band allignment for graphene at a gate voltage V_{bg} with metallic back gate with graphene not strained. **(b)** Band allignment for graphene under tensile strain at a gate voltage $\widetilde{V}_{bg}$ with metallic back gate. Figure adapted from our publication,Ref. [35]

$$S = e(V_{cnp}^{\Delta z=0.8mm} - V_{cnp}^{\Delta z=0mm}) = 8meV \tag{6.10}$$

The scalar potential constant s_0 is defined as,

$$s_0 = -S/\varepsilon_t \tag{6.11}$$

From the experiemnt it results in, $s_0 \approx 3.8$ eV. The theoretical predictions for s_0 is in the range of 2.5 - 4 eV. The s_0 extracted from the experiment is in the range of the theoretical predictions [34, 112, 114].

6.3 Strain effect on CNP in bilayer graphene

The following section will discuss the strain effects around the CNP (charge neutrality point) of bilayer graphene (BLG), measured in a hall bar device geometry. The optical image of the device is shown in Fig. 6.4(a). Hall bar geometry gives the possibility to compare strain effects in both two terminal and four terminal measurements.

Two terminal measurement

Fig. 6.4 shows two terminal differential conductance (G_{2tml}) vs V_{bg} for different Δz (distance moved by wedge to bend the substrate, illustrated in Fig. 3.8). The increase in G_{2tml} with Δz for $|V_{bg}| > 2$ V is similar to the changes in edge contact resistance as discussed in Ch. 5 for single layer graphene. On comparing the curves between $\Delta z = 0$ - 0.5 mm and $\Delta z = 0.6$ - 1.0 mm, the variations in conductance at $|V_{bg}| > 2$ V appears to be smoothened out with strain especially on the electron side. For 0.5 V $< |V_{bg}| <$ 1.5 V, there is a non-monotonic change in G_{2tml} when Δz changes from 0.4 mm to 0.8 mm with a decrease followed by an increase in conductance in both hole and electron side. The field effect mobility from the linear fit around CNP (using Method II described in subsec. 5.3) gives ~ 67700 cm^{2}V^{-1}s^{-1}. Towards the CNP, the zoom-in shown in Fig. 6.4(b) shows the changes with strain. The conductance around CNP shows an increase with strain, see Fig. 6.4(b). This seems to be an effect not directly related to scalar potential and will be discussed in Ch. 7. The CNP is located slightly to negative side of V_{bg} indicating device junction is slightly n-doped. V_{cnp} downshifts with strain, similar to the shift observed in graphene under tensile strain. V_{cnp} is obtained from the V_{bg} axis corresponding to the minimum in G_{2tml}. Fig. 6.4(c) shows V_{cnp} plotted against Δz. The effect remains after several straining cycle. Fig. 6.7 shows the straining and unstraining cycle plots for V_{cnp} versus Δz and the effect is reversible. V_{cnp} downshifts by ~ 5 mV for $\Delta z = 1$ mm. The scalar potential corresponding to the shifts will be calculated in the upcoming section 6.3.1.

Four terminal measurement

The hall bar geometry makes it possible for four terminal measurements. Fig. 6.5(a) shows the four terminal differential conductance (G_{xx}) as a function of V_{bg}. G_{xx} is measured by passing current from contact 1 to 4 and measuring the voltage drop across contacts 2 and3, $G_{xx} = I_{14}/V_{23}$. The changes in G_{xx} at $|V_{bg}| > 2$ V are non-monotonic with Δz. At electron side, an initial decrease in conductance followed by an increase is observed in steps from Δz = 0.3 mm to $\Delta z = 0.5$ mm and less changes towards higher $\Delta z = 0.7$ mm to 1 mm. The hole side also shows similar changes but less compared to that on

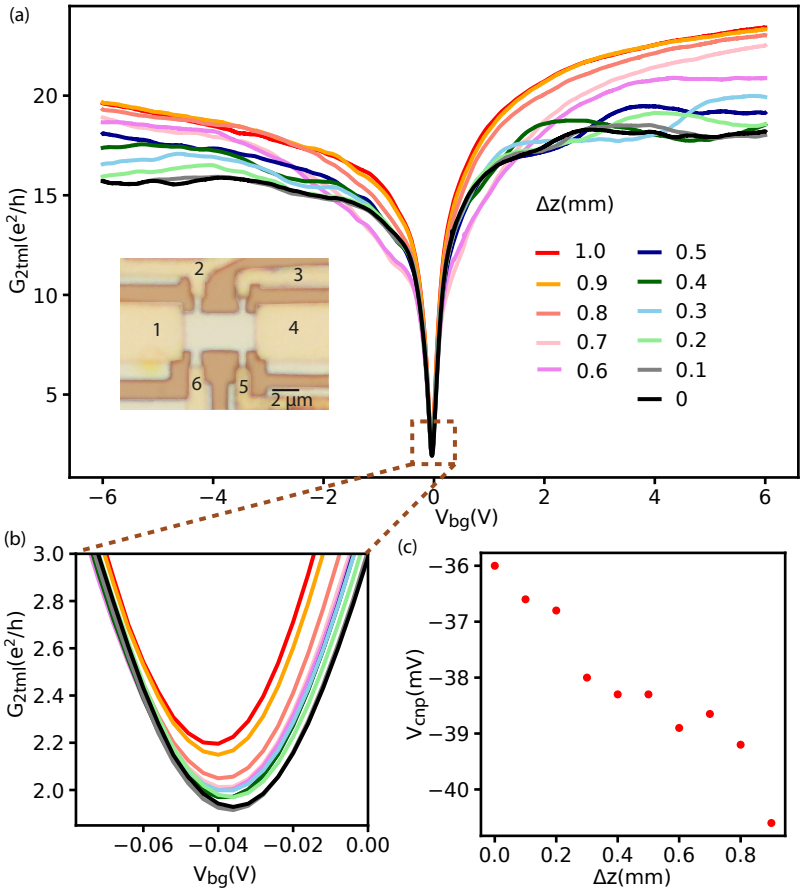

Figure 6.4 Strain effect in two terminal measurement in BLG. (a) G_{2tml} vs V_{bg} for straining cycle of hall bar device. $G_{2tml} = I_{14}/V_{14}$,measured by passing current from contact 1 to 4 and measuring the voltage drop across contacts 1 and 4. **(b)** Zoom in to the CNP region of the plot. The minimum value of G_{2tml} and V_{cnp} are sensitive to strain. **(c)** V_{cnp} versus Δz, downshift in V_{cnp} with strain. It can be the scalar potential induced by strain as in graphene.

the electron side. A similar trend is found in G_{2tml} in the range 0.5 V < $|V_{bg}|$ < 1.5 V. These changes with strain most probably arise from the bulk of the device junction as it is also probed in the four terminal measurement and we attribute them to changes in scattering potential slightly changing with the mechanical deformation either the position of these scaterrers or the strength of disorder potential [53].

We now focus on more systematic changes observed at low carrier densities. The zoom in to the CNP region, Fig. 6.5(b) shows the changes in G_{xx} with Δz. Similar shifts are observed in the minimum conductance of G_{2tml} and CNP position in two terminal measurement, as shown above. V_{cnp} is obtained from the V_{bg} axis corresponding to the minimum in G_{xx}. Fig. 6.5(c) shows the plot of extracted V_{cnp} versus Δz. For Δz = 1 mm, V_{cnp} downshifts by $\sim$ 5.3 mV similar to the shift observed in two terminal measurements in the single layer graphene in Sec. 6.2. The effect is reversible as can be seen in the plot of V_{cnp} versus Δz for straining and unstraining cycle shown in Fig. 6.7.

6.3.1 Estimation of scalar potential constant in BLG

We interpret the shift observed in bilayer graphene (BLG) in a similar way as for monolayer graphene. The two layers in BLG are assumed to get tensile strained equally as both the layers are probably similarly edge contacted and the mechanical coupling of the edge contact to both layers are considered to be the same. The schematic of the cross section of edge contacted BLG device junction is shown in Fig. 6.6(a). Instead of the linear monolayer graphene dispersion relation, we assume BLG dispersion is parabolic at low momenta values as discussed in Eq. 2.26. Our aim now is to explain the observed shift of the CNP with an on-site potential change, similar as the scalar potential in monolayer graphene. For brevity, we also call this potential "scalar potential". This causes the energy of CNP in BLG downshift with tensile strain and results in an increase of the intrinsic work function of the undoped BLG (W^0_{blg}). In a tight binding model, the decrement in the energy of the BLG under tensile strain can be pictured as the decrease in next nearest neighbour hopping parameter with increasing bond lengths. The band allignment for BLG and metallic back gate for the two scenario : (i) BLG under no strain (ii) BLG under tensile strain are schematically shown in Fig. 6.6(b),(c).

The quantities in the band allignment for BLG under no strain at a back gate voltage V_{bg} are related by,

$$W_M - eV_{bg} = W^0_{blg} - \mu_{blg} - e\phi \tag{6.12}$$

The tensile strain causes change in some quantities and are denoted by tilde symbol. The band allignment relation for BLG under tensile strain at back

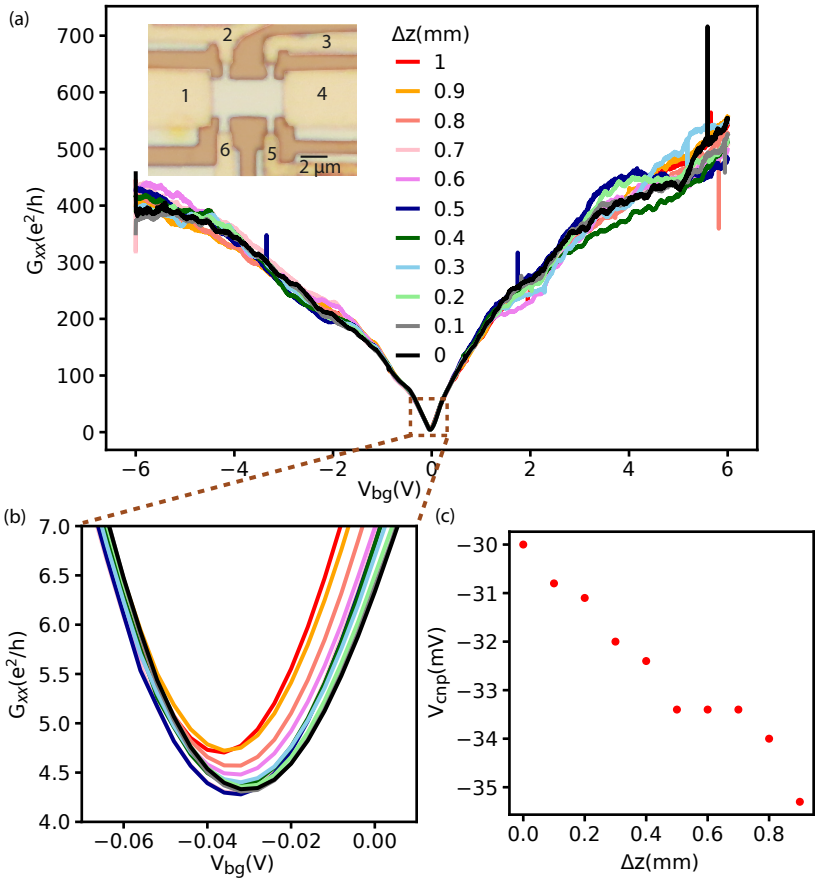

Figure 6.5 Strain effect in four terminal measurement in BLG.(a) G_{xx} vs V_{bg} for straining cycle of hall bar device. $G_{xx} = I_{14}/V_{23}$,measured by passing current from contact 1 to 4 and measuring the voltage drop across contacts 2 and3. **(b)** Zoom in to the CNP region of the plot. The minimum value of G_{xx}, V_{cnp} are sensitive to tensile strain. **(c)** V_{cnp} versus Δz, downshift in V_{cnp} with strain. It can be the scalar potential induced by strain as in single layer graphene.

gate voltage $\widetilde{V}_{bg}$ is

$$W_M - e\widetilde{V}_{bg} = \widetilde{W}^0_{blg} - \widetilde{\mu}_{blg} - e\widetilde{\phi} \tag{6.13}$$

The conductance minima at CNP of BLG is the feature used to track the shift in BLG with tensile strain. A given feature occurs at a fixed charge carrier density (n). At a fixed n, $\widetilde{\mu}_{blg} = \mu_{blg}$ and $\widetilde{\phi} = \phi$ under the same assumptions as made for monolayer graphene in subsec. 6.2.1. Under these conditions, we find the scalar potential in BLG (S_{blg}) as,

$$S_{blg} = -(\widetilde{W}^0_{blg} - W^0_{\mathrm{blg}}) = e(\widetilde{V}_{cnp} - V_{cnp}) \tag{6.14}$$

where $\widetilde{V}_{cnp}$ and V_{cnp} are the back gate voltage at which CNP is reached in unstrained and strained case. Fig. 6.7 shows the comparison between the V_{cnp} shifts with Δz for four terminal and two terminal measurement configuration. The slope of the V_{cnp} versus Δz plot for straining(green line) and unstraining cycle(orange line) for two terminal measurement configuration are $\sim$ -4.60 mV/mm and -3.72 mV/mm. Similarly slopes for straining and unstraining cycle for four terminal measurement configuration are $\sim$ -5.49 mV /mm and -5.24 mV/mm.

6

If the strain is assumed to be not that different for graphene and bilayer graphene for the same Δz in the low temperature setup, then the same calibration curve shown in Fig. 6.1(b) can be used to convert Δz to the average strain ($\bar{\varepsilon}$). Also the other parameters like temperature are the same for all the measurements. The tensile strain attained in the device junction seems to be roughly scale proportional to the inverse of length of the device junction between the edge contacts for the same Δz from the Raman studies in Ref.[25]. The length of bilayer graphene hall bar device is $\sim$ 1.7 times that of the graphene device junction in Sec. 6.2. From the $\bar{\varepsilon}$ verus Δz plot in Fig. 6.1, Δz = 1 mm corresponds to total strain of $\epsilon_t = 0.22\%$ for the graphene junction in Sec. 6.2. So in the BLG hall bar device upon considering the scaling of strain with length of device junction, total strain in the junction is $\epsilon_t^{blg} = 0.13\%$. Following the similar calculation as in graphene for the scalar potential constant in BLG : (a) two terminal measurement gives (3.2 $\pm$ 0.3) eV (b) four terminal measurement gives (4.1 $\pm$ 0.1) eV. Both the values are close to the estimated scalar potential constant for monolayer graphene from experiment(= 3.8 eV).

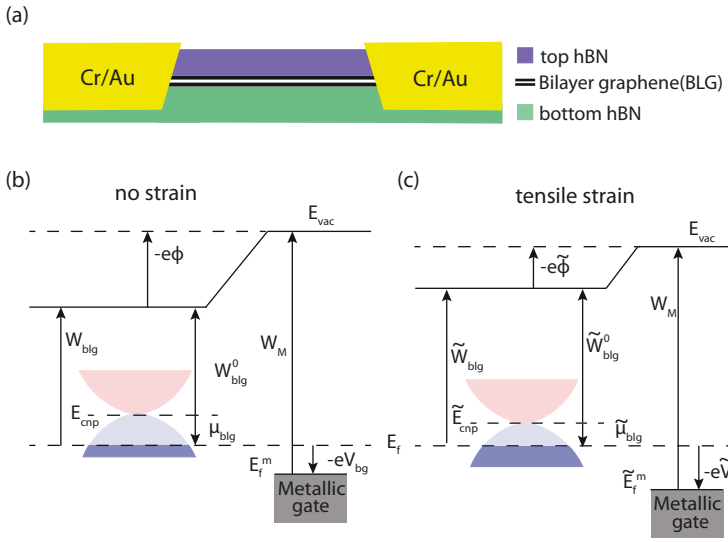

Figure 6.6 (a) Schematic of the cross section of edge contacted BLG device junction encapsulated with hBN. Both the layers of BLG are edge contacted and the mechanical coupling of contacts to both layers of BLG are assumed to be same. Thus one can assume both layers of BLG are equally under tensile strain upon bending of substrate. **(b)** Schematic of band allignment of BLG and metallic back gate under no strain in BLG, at a gate voltage V_{bg}. **(c)** Schematic of band allignment of BLG and metallic back gate when BLG is tensile strained and at gate voltage $\widetilde{V}_{bg}$.

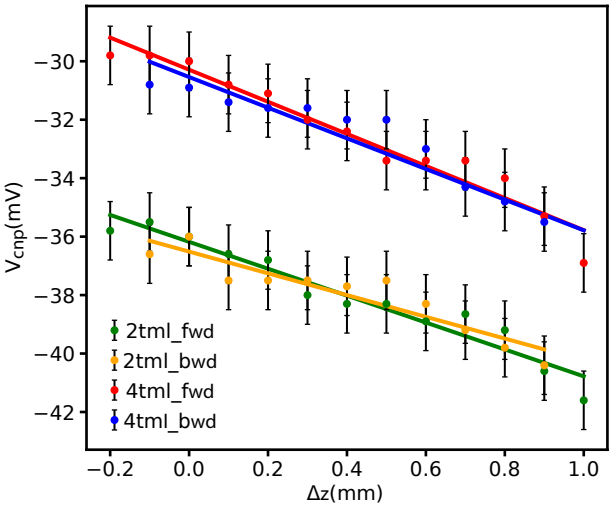

Figure 6.7 V_{cnp} **versus** Δ**z for straining and unstraining cycle.** Comparing straining and unstraining cycles of V_{cnp} vs Δz for two terminal and four terminal measurement configurations. The errorbars (2 mV) are taken as half the measurement step size in V_{bg}. The red and blue data points are for the straining and unstraining cycle for four terminal measurement , similarly green and orange data points are for the straining and unstraining cycle for two terminal measurement. The corresponding coloured lines are linear fit to the data points.

6.4 Summary

The strain induced scalar potential is observable in the transport experiments carried out in graphene and bilayer graphene. Experimentally, we find similar shifts in the conductance curve in the gate voltage under strain for both single and bilayer graphene that seem quite independent of disorder and contact details. We understand these shifts having the same physical origin, namely a bond elongation and a corresponding reduction of next nearest neighbor hopping in each graphene layer individually, that results in a change in on-site energy on a given sublattice. The rate of shift of on-site energy with strain is characterised by scalar potential constant(s_0). The s_0 extracted for graphene is around $\sim$ 3.8 eV and for bilayer graphene $\sim$ 3.2 - 4.1 eV. The estimates for s_0 are in agreement with the theoretical estimates and Kelvin probe microscopy experiments in the Ref. [34, 112, 113]. Scalar potential constant can be dependent on the bond strength in a given material system. In graphene and bilayer graphene, the strongest interaction is the in-plane C-C bond and the tensile strain acts against this stable C-C bond. Similar values from the estimates for s_0 can imply similar bond strength in the material system.

Only features that are reproducible with strain were looked into. In four terminal measurement in bilayer graphene (BLG), the changes observed at V_{bg} (gate voltage) > 1 V doesn't follow a monotonic change with strain which can be related to the slight changes in the disorder distribution or the disorder potential with the mechanical deformation. In the estimation of scalar potential constant for BLG we assumed both layers of BLG to be equally strained but if it is different it can lead to a gradient in scalar potential across the layers in BLG which might can result in a strain induced electric field in the system. In the coming chapter we implement top gate for bilayer graphene device which gives independent control on charge carrier density and electric field in the system. With the additional control with electric field, effects of strain in different transport regime in BLG will be explored in the upcoming chapter.

7 Transport in bilayer graphene under tensile strain

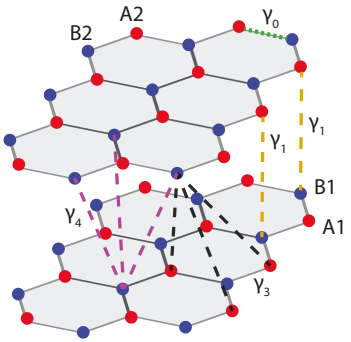

This chapter focusses on the strain effects in bilayer graphene (BLG). BLG exhibits a distinct bandstructure compared to monolayer graphene. The interlayer hopping[1] result in a rough parabolic bandstructure described by an effective mass for the charge carriers in BLG, discussed in Ch 2.1.3. For simplicity, we neglect the emergence of trigonal warping (discussed in Ch. 2.1.3) and other finer structures in the bandstructe of BLG. The first section discusses the change in the conductance around charge neutral point (CNP) of BLG induced by tensile strain. For this, we discuss four terminal differential conductance mesurements in BLG hall bar devices. The possible reasons that can lead to the observed changes are also discussed. In single gated BLG devices, independent control of charge carrier density and electric field is not possible, so we further implemented top gate in BLG system following the recipe described in Ch. 3. The interlayer symmetry in BLG can be broken with an external electric field and whether strain has an effect on transport in this regime is investigated in this section[2]. The last section shows the effect of strain on hBN/BLG moiré superlattices from the transport at the secondary Diac point at finite electric field.

[1] Schematic showing BLG with interlayer hopping terms.
[2] Measurements carried out in collaboration with Szentpéteri Bálint, PhD student, Dept. of Physics, Budapest University of Technology and Economics (BME)

7.1 Strain effect around conductance minimum in BLG

In addition to the strain induced scalar potential shift in BLG discussed in Ch. 6, we also find an increase in minimum conductance with strain (ε). Fig. 7.1(a) and (b) show the four terminal differential conductance (G_{xx}) with back gate voltage (V_{bg}) for different Δz (distance moved by wedge to bend substrate in strain setup I) in two hall bar devices, Hb1 and Hb2. The figures on the right side of Fig. 7.1(a),(b) are the corresponding zoom in to the charge neutrality point (CNP) of the conductance in the two device junctions. The conductance around CNP exhibits a systematic change with strain, can be seen in the zoom in of the respective plots. Fig. 7.1(c) shows the plot of minimum of G_{xx} versus Δz for devices Hb1 and Hb2. In both device junction, the conductance around the CNP increase with Δz. It increases by ~ 0.4 e^2/h for Hb1 and ~ 0.8 e^2/h for Hb2. This increase is not related to the contact resistance changes described in Ch. 5, as the four terminal measurement probes bulk of the device. The changes at larger gate volatge in Hb1 are not monotonic where as in Hb2 the curves almost overlap each other indicating the changes observed around CNP are independent of the features at larger gate voltage.

The mobility (μ) around CNP of the two hall bar devices for Δz = 0 and 1 mm is shown in Fig. 7.2. Near CNP, μ is almost linear in V_{bg} and saturates further at a higher V_{bg} indicating a transition to constant mobility. This indicates the two types of scattering mechanisms, a long range, Coulomb type of scattering that can get screened by a larger electron density, and short range scattering that is independent of n [115]. In both the device junction, the field effect mobility increases with tensile strain around the CNP before mobility reaches the saturation regime, see Fig. 7.2.

The region around charge neutrality point in BLG has electron-hole puddles similar to the observation in graphene [50]. The transport around CNP is dominated by disorder and the conductance at minimum depends on the type of scaterrers present in the system [116, 117]. The minimum conductivity slightly increases with increase in impurity carrier density in long range scatterer limit [116], as the conduction band starts to get filled it leads to increase in screening and thus the conductivity goes higher.

As μ depends linearly on V_{bg} around CNP, it indicates the conductivity gets better with increase in charge carrier density as it help to screen from the disorder potential. Also μ increases around CNP with strain, see Fig. 7.2. The strain fluctuations in the system might have reduced with the tensile strain [53] and resulted in the increase in μ. The charge carrier transport is limited by mobility in this regime around CNP where μ is proportional to V_{bg}. And strain

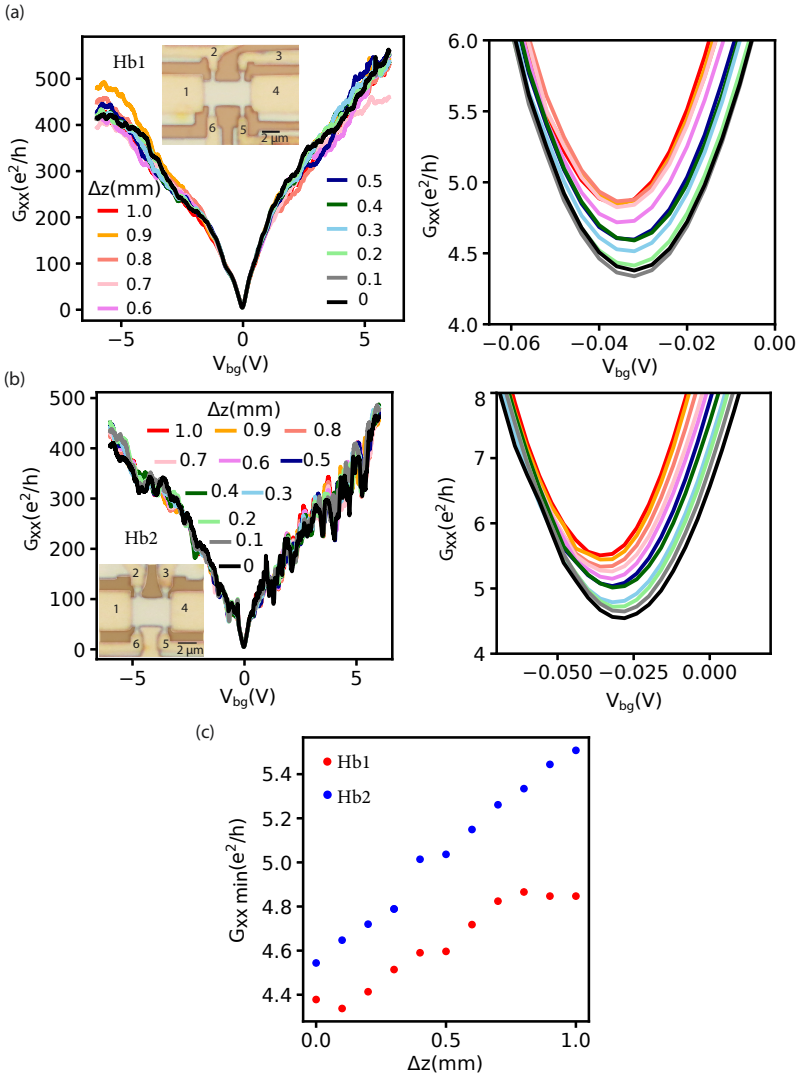

Figure 7.1 Strain effects in four teminal conductance (G_{xx})measurements in BLG. (a) G_{xx} verus V_{bg} in hall bar device Hb1 for different Δz. $G_{xx} = I_{14}/V_{23}$, current send from contact 1 to 4 and voltage probed between contacts 2 and 3. **(b)** G_{xx} verus V_{bg} in hall bar device Hb2 for different Δz. $G_{xx} = I_{14}/V_{65}$, current send from contact 1 to 4 and voltage probed between contacts 6 and 5. **(c)** The minimum of G_{xx} plotted against bending distance Δz for devices Hb1 and Hb2.

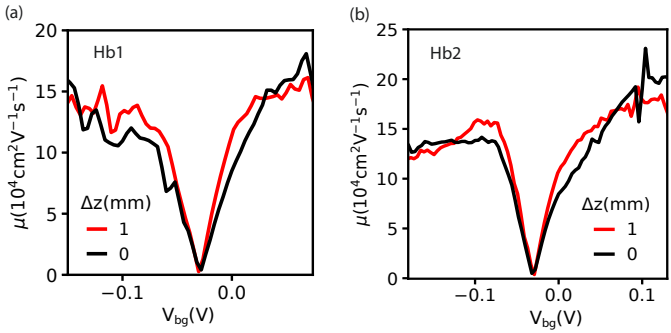

Figure 7.2 Field effect mobility in Hb1, Hb2 under tensile strain. **(a)**,**(b)** The field effect mobility, $\mu = \frac{\partial G_{xx}}{\partial V_{bg}} \frac{L}{W c_g}$ is plotted against V_{bg} for device Hb1, Hb2. Around CNP, μ is linear in V_{bg} and saturates further at a higher V_{bg} for both the devices. The mobility curve for $\Delta z = 1$ mm is adjusted by the shift in CNP due to scalar potential to that of the curve at $\Delta z = 0$ to make comparison for the effect of strain on mobility.

act as a factor to improve the mobility in this regime and this might lead to the increase in the conductance around CNP with strain.

Both devices Hb1 and Hb2 shows different offset in change in minimum conductance for the same bending (see Fig. 7.1(c)), this can be due to the different strain fluctuations present in the devices.

7.2 Strain effects in dual gated BLG

This section will focus on the effect of tensile strain in dual gated BLG. The dual gate is implemented in hBN encapsualted BLG device using the fabrication recipe discussed in subsec. 3.1.3. The total charge carrier density (n) and the electric field in the system can be independently tuned using the top and bottom gate [48]. On electrical gating the BLG device with both bottom and top gate, the corresponding displacement field D_t, D_b are as follows:

$$D_t = \frac{\epsilon_0 \epsilon_t (V_{tg} - V_t^0)e}{d_t} = c_t(V_{tg} - V_t^0) = n_t e \tag{7.1}$$

$$D_b = -\frac{\epsilon_0 \epsilon_b (V_{bg} - V_b^0)e}{d_b} = -c_b(V_{bg} - V_b^0) = -n_b e \tag{7.2}$$

where c_b , c_t are the bottom and top gate capacitance per unit area, d_t and d_b are the thickness of top and bottom hBN dielectric, ϵ_t and ϵ_b are the dielectric constant of top and bottom hBN, ϵ_0 is permittivity of free space, V_t^0 and V_b^0 are the charge neutral point offsets in BLG for the top and bottom gate, n_t and n_b are the charge carrier density induced on top and bottom layers of BLG. The D_t, D_b at the top and bottom layer of BLG will lead to two effects:

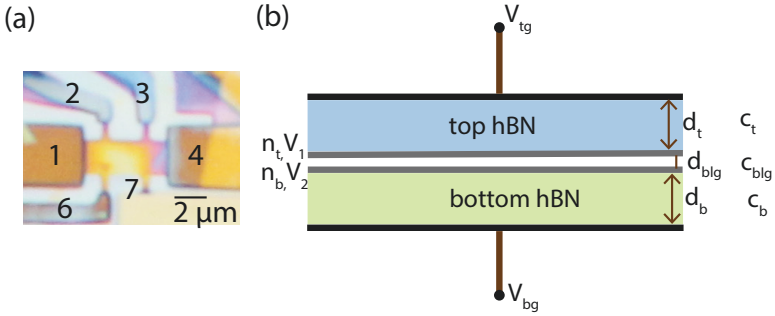

Figure 7.3 (a) Optical image of bilayer graphene(BLG) hall bar device with top graphite gate and bottom Au(gold) gate.**(b)** Schematic of the cross section of dual gated BLG device.

(i) The difference of D_t and D_b, δD = D_t - D_b will induce a net charge carrier doping and will lead to change in chemical potential. For δD = 0 defines the charge neutral point(CNP) in BLG.
(ii) The average displacement field, $D = (D_t + D_b)/2$ breaks the layer inversion symmetry in BLG and result in the opening of a band gap around the CNP [47,

48]. The total charge carrier density induced can be written as,

$$\begin{aligned} n = n_t + n_b &= (c_t(V_{tg} - V_t^0) + c_b(V_{bg} - V_b^0))/e \\ &= (c_t V_{tg} + c_b V_{bg})/e + n_0 \end{aligned} \tag{7.3}$$

The effective average displacement field (D) can be written as,

$$\begin{aligned} D &= \frac{1}{2}(c_t(V_{tg} - V_t^0) - c_b(V_{bg} - V_b^0)) \\ &= \frac{(c_t V_{tg} - c_b V_{bg}) + D_0}{2} \end{aligned} \tag{7.4}$$

where n_0 and D_0 are the offset doping and offset displacement field in the system. Fig. 7.4 shows the four terminal resistivity (ρ_{xx}) map of the dual gated BLG hall bar device in V_{tg} - V_{bg} space, the highly resistive line in the map with negative slope corresponds to the CNP of BLG. The minima of ρ_{xx} should be ideally at (0 V, 0 V) but it can be seen its shifted away from it in both V_{tg} , V_{bg} axis. This offset is represented by V_t^0 and V_b^0 which corresponds to the offset doping in the respective top and bottom gates. The estimation of

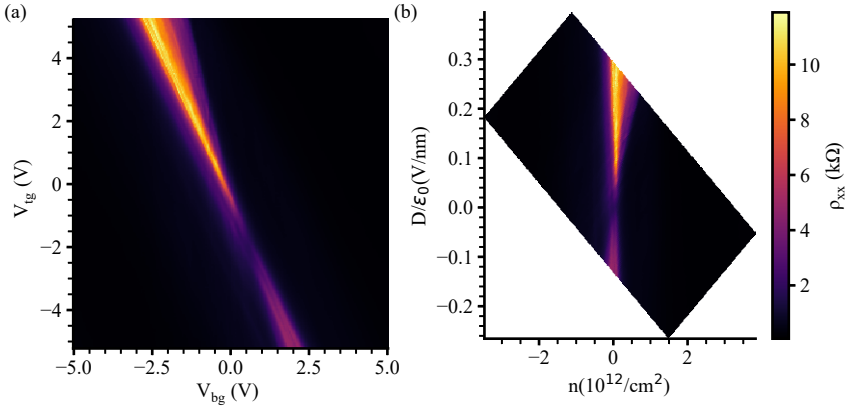

Figure 7.4 Dual gating in BLG. (a) Four terminal resistivity map of the BLG device in V_{tg} - V_{bg} space. **(b)** The resistivity map in V_{tg} - V_{bg} space transformed to $n - D/\epsilon_0$ map using the estimated lever arms in Eq. 7.3,7.4.

back gate and top gate lever arms , c_t and c_b will be discussed in appendix. 2. Using Eq. 7.3 and 7.4 with the estimated lever arms, ρ_{xx} can be plotted in n-D/ϵ_0 space, see Fig. 7.4(b). As the electric field (D/ϵ_0) increases, ρ_{xx} increases around the CNP. In terms of conductance, it gets supressed with electric field. This can be an indicator that a gap is opening in BLG [118].

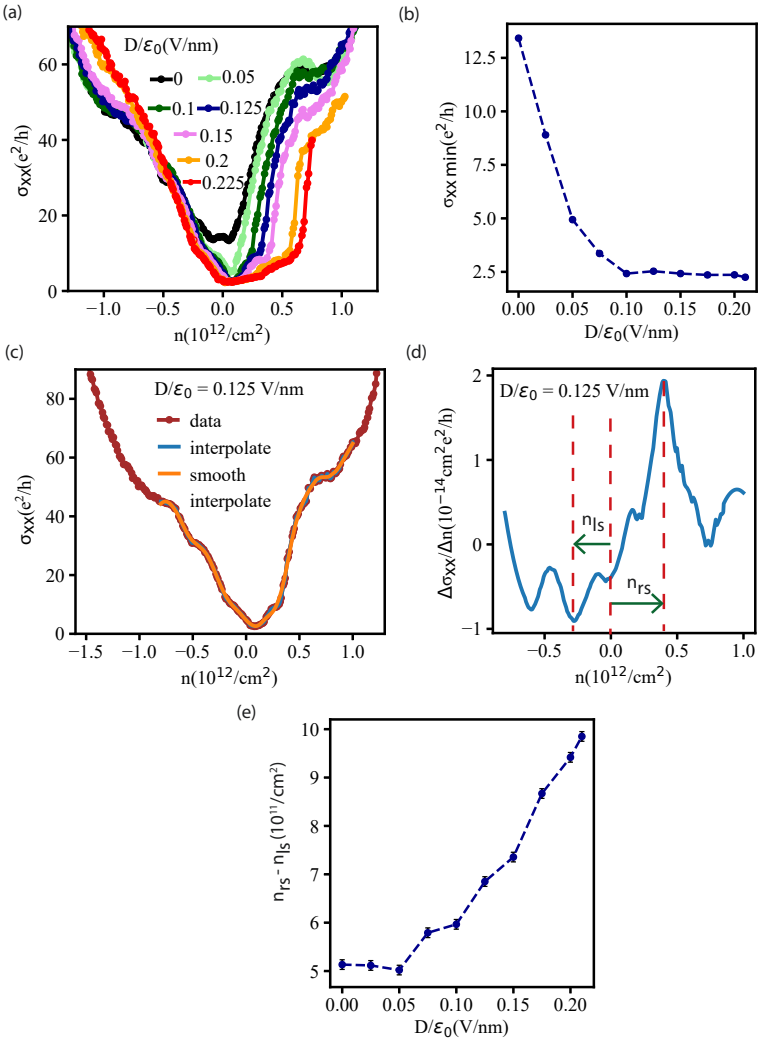

Figure 7.5 σ_{xx} around CNP at finite D field. (a) Cross-section along n axis of n-D/ϵ_0 map in Fig. 7.4(a). **(b)** Minimum conductivity(σ_{xx}^{min}) plotted against D/ϵ_0 from each curve in (a). **(c,d)** Smoothening of the data to avoid small fluctuations to identify n_{rs} and n_{ls} from the derivative of conductivity. **(e)** (n_{rs} - n_{ls}) versus D/ϵ_0 using the procedure described in (c,d). It captures the increase in broadening of σ_{xx} around CNP with the applied electric field.

7.2.1 Conductance around CNP at finite electric field

The four terminal conductivity (σ_{xx}) around CNP at different electric fields (D/ϵ_0) is compared in Fig. 7.5(a). First, on the minimum conductivity and later on the broadening of the CNP region due to electric field is discussed in this part of the section.

Electric field effect on minimum conductivity at CNP

As the electric field is increased, the minimum conductivity decreases and saturates around 2.5 e^2/h, see Fig. 7.5(a). The plot of minimum condcutivity read out from each curve in Fig. 7.5(a) versus the electric field is shown un Fig. 7.5(b). The decrease in minimum conductivity is an indication of band gap opening in BLG [118] but still there is some residual conductivity which might point to the gap having a residual density of states. One possibility for such conducting states in the gap is through the spatial potential fluctuations in the device that modulate the band structure and can create electron-hole puddles [119]. These spatial fluctuations within the gap don't get screened due to low charge carrier density and when fermi level alligns with the band gap region in bilayer graphene (BLG), the states existing due to fluctuations contributes to the conducting paths. The device exhibited secondary dirac point in transport characteristics, which we interprete as stemming from a moié superlattice formed by the superposition of the hBN and bilayer graphene lattice. Thus the moiré potential can be one of the sources for spatially modulated potential fluctuation in the device. Other possibility might include the conduction along the edges of BLG where it may be not gated as effectively as in bulk.

Broadening of CNP region with electric field

In addition to the decrease in minimum conductivity, the curve broadens with electric field (D/ϵ_0), see Fig. 7.5(a). The broadening mostly happens to the electron side ($n>0$) in comparison with the hole side ($n<0$). The point of steepest slope of σ_{xx} around the CNP along n axis shifts with electric field. The point of steepest slope in conductivity around CNP at electron side is labeled as n_{rs} and on hole side as n_{ls}. The steepest slope is considered as the transition from residual density of states in the band gap to the density of state of BLG.

Inorder to extract n_{rs} and n_{ls} for each curve in Fig. 7.5(a), we did intially an interpolation of the conductivity (σ_{xx}) curve around the charge neutrality point (CNP) followed by smoothening of it inorder to avoid the small fluctuations in between which makes it difficult to extract the exact position of n_{rs} and n_{ls}. This is shown in Fig. 7.5(c). Further, the derivative of the σ_{xx} versus

n after smoothing of the small fluctuations in data is shown in Fig. 7.5(c), the highest slope value from the derivative on electron and hole side gives the position of n_{rs} and n_{ls}. The difference, (n_{rs} - n_{ls}) is plotted against D/ϵ_0 (Fig, 7.5(e)) which captures the increase in broadening of σ_{xx} around the CNP region for increasing D/ϵ_0 .

7.2.2 Strain effect around CNP at finite electric field

The effect of tensile strain on the conductivity (σ_{xx}) around CNP at finite electric field (D/ϵ_0) will be discussed in the following.

Fig. 7.6(a),(b) shows the σ_{xx} versus n plot for different Δz (distance moved by wedge to bend substrate in strain setup I) at an applied electric field (D/ϵ_0) of 0 and 0.2 V/nm. The change in the position of steepest slope of conductivity in the electron side (n_{rs}) with strain seem to occur for D/ϵ_0 = 0.2 V/nm. The hole side shows not much change in the position of steepest slope region of conductivity with strain for both D/ϵ_0 = 0 and 0.2 V/nm. The effect of tensile strain in σ_{xx} versus n at D/ϵ_0 = 0.2 V/nm looks like an addition to the applied D/ϵ_0 as the position of n_{rs} (at electron side) is shifted further towards higher density, similar to the effect of D/ϵ_0 on σ_{xx} as shown in Fig. 7.5(a). Based on this the change in D/ϵ_0 due to tensile strain is estimated in the following.

Estimation of change in D/ϵ_0 due to tensile strain

The same analysis carried out in subsec. 7.2.1 for estimating the position of steepest slope in conductivity along n axis is used to get the position of steepest slope in conductivity for the electron side (n_{rs}) for different Δz. In the hole side ($n < 0$), the position of the steepest slope (n_{ls}) with Δz remains almost the same, no significant change. So, we further only look at the changes in n_{rs} with Δz. The shift of n_{rs} with Δz for different D/ϵ_0 is shown in Fig. 7.6(c). Towards higher D/ϵ_0, n_{rs} versus Δz curve gradually develops a slope. The additional electric field due to tensile strain is estimated using the n_{rs} versus D/ϵ_0 dependence for Δz = 0 found in subsec. 7.2.1 and the plot is shown in Fig. 7.6(d). The axis of the plot is inverted to make an estimate for the slope of D/ϵ_0 versus n_{rs} by making a linear fit from the point where there is significant change in the plot. The slope is $\sim (3.72 \pm 0.16)\times 10^{-8}$ Vm. The slope extracted in combination with the plot of n_{rs} versus Δz in Fig. 7.6(c) is used to estimate the calculated electric field (D_{calc}/ϵ_0) corresponding to Δz for a given applied electric field (D/ϵ_0), shown in Fig. 7.6(f).

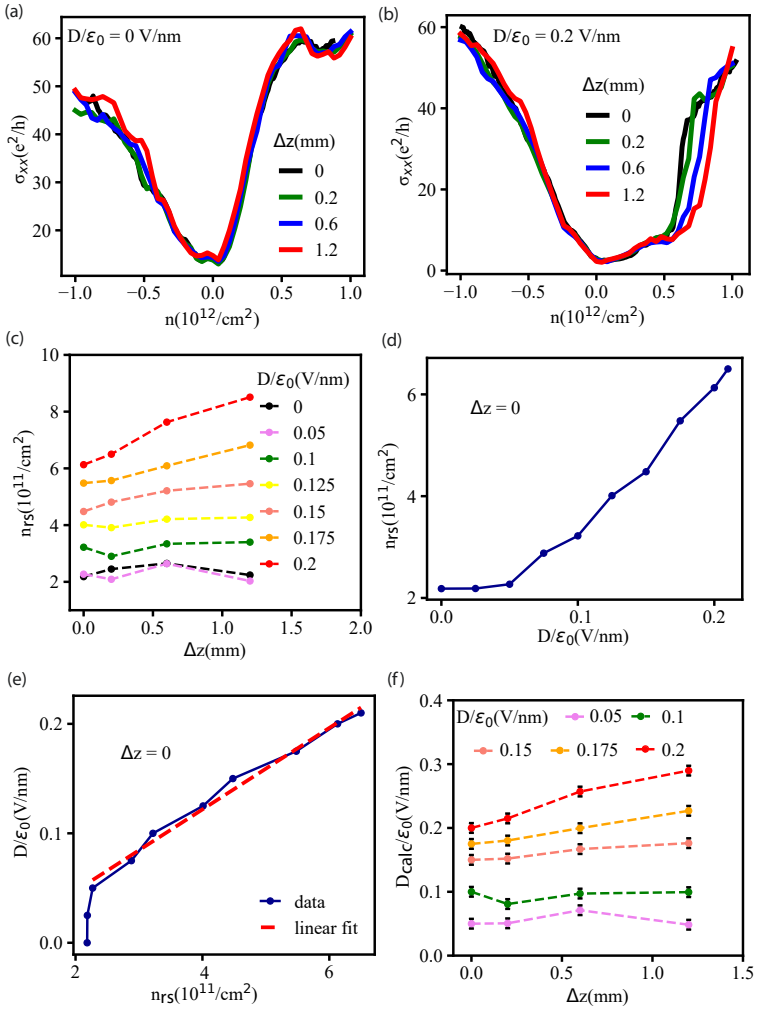

Figure 7.6 Strain effect on σ_{xx} around CNP at finite D/ϵ_0. (a,b) σ_{xx} versus n for $D/\epsilon_0 = 0{,}0.2$ V/nm under tensile strain. For $D/\epsilon_0 = 0.2$ V/nm, n_{rs} shifts with strain. **(c)** The shift of n_{rs} with Δz for different D/ϵ_0. The slope of n_{rs} versus Δz seems to have dpendance on D/ϵ_0. **(d,e)** From analysis in Fig. 7.5(d) carried for $\Delta z = 0$ for different D/ϵ_0. The plot is inverted to get the slope of D/ϵ_0 with n_{rs}. **(f)** D_{calc}/ϵ_0 versus Δz. Estimation of D_{calc}/ϵ_0 is described above.

D_{calc}/ϵ_0 includes the applied electric field (D/ϵ_0) and the additional electric field considered to come from strain. As Δz is increased, strain increases, discussed in sec. 4.9. Thus we can see there is an additional contribution to electric field from bending if there is aready an applied electric field. The possibilities for such an observation will be discussed in the next part of the section.

Possible mechanisms for strain induced changes in electric field

Tensile strain induced scalar potential in BLG is discussed in Ch. 6. If top and bottom layer of BLG are not equally strained, then this can result in a scalar potential difference which possibly can create an addtional electric field in the system. Also, if the interlayer distance in BLG change under tensile strain but with a constant charge on each layer, then it can result in a change in the electric field. In the following, a simple model is described that allows us to estimate the magnitude of both effects mentioned.

Let μ_t^{elch} and μ_b^{elch} be the electrochemical potential of the top and bottom layer of BLG. Then electrochemical potential difference between the layers is,

$$\Delta\mu^{elch} = \mu_t^{elch} - \mu_b^{elch} \tag{7.5}$$

The electrochemical potential in each of the layer can be written as,

$$\begin{aligned} \mu_t^{elch} &= \mu_t^{el} + \mu_t^{ch} \\ \mu_b^{elch} &= \mu_b^{el} + \mu_b^{ch} \end{aligned} \tag{7.6}$$

where μ_t^{el} , μ_b^{el} are the electrical potential of the top and bottom layer of BLG, μ_t^{ch} , μ_b^{ch} are the chemical potential of the top and bottom layer of BLG. Using Eq. 7.6 in 7.5 gives,

$$\begin{aligned} \Delta\mu^{elch} &= (\mu_t^{el} - \mu_b^{el}) + (\mu_t^{ch} - \mu_b^{ch}) \\ &= \Delta\mu^{el} + \Delta\mu^{ch} \end{aligned} \tag{7.7}$$

The difference in electrical potential between top and bottom layer gives rise to electric field between the layers, $D/\epsilon = \Delta\mu^{el}/\mathrm{d}_{blg}$ where d_{blg} is the interlayer distance in BLG , $\epsilon = \epsilon_0\epsilon_{blg}$ is the effective dielectric constant of BLG, D/ϵ is the effective electric field between the two layers. Thus one can rewrite Eq. 7.7 into

$$\Delta\mu^{elch} = \frac{Dd_{blg}}{\epsilon_0\epsilon_{blg}} + \Delta\mu^{ch} \tag{7.8}$$

From this the applied electric field, D/ϵ_0 is

$$\frac{D}{\epsilon_0} = \frac{\epsilon_{blg}}{d_{blg}}(\Delta\mu^{elch} - \Delta\mu^{ch}) \tag{7.9}$$

Upon introducing tensile strain (ε) in the expression for applied electric field we get,

$$\frac{D(\varepsilon)}{\epsilon_0} = \frac{\epsilon_{blg}}{d_{blg}(\varepsilon)}(\Delta\mu^{elch}(\varepsilon) - \Delta\mu^{ch}(\varepsilon)) \tag{7.10}$$

under the assumption that ϵ_{blg} will not change with strain. Also the assumption that top and bottom gate capacitance in the device to remain same under tensile strain. The maximum strain achievable with bending setup and edge contact technique is less than 1 %. We assume that each quantity depends on ε linearly, effectively using a Taylor expansion in ε. From Eq. 7.10 we can consider different cases :

1. Change in interlayer distance ($\mathbf{d}_{\mathrm{blg}}$)

Considering only the change in interlayer distance with strain and while keeping the electron densities and potentials constant, we can write,

$$d_{blg}(\varepsilon) = d_{blg}(\varepsilon = 0) + \frac{\partial d_{blg}}{\partial \varepsilon}\varepsilon \tag{7.11}$$

On substituting Eq. 7.11 in Eq. 7.10 we get,

$$\frac{D(\varepsilon) - D(0)}{\epsilon_0} = -\frac{\epsilon_{blg}D(0)}{\epsilon_0 d_{blg}(0)}\frac{\partial d_{blg}}{\partial \varepsilon}\varepsilon \tag{7.12}$$

$$D(0) = \frac{\epsilon_0\epsilon_{blg}(\Delta\mu^{elch}(0) - \Delta\mu^{ch}(0))}{d_{blg}(0)} \tag{7.13}$$

where $d_{blg}(0) = 3.4$ Å. The dielectric constant of BLG is around 3 [120]. Now this expression can be used to estimate the interlayer distance change with in-plane tensile strain (ε). In other terms it is a measure of Poisson ratio of BLG in the perpendicular direction to its plane. For the applied electric field $D(0)/\epsilon_0 = 0.2$ V/nm , the additional electric field induced from strain at Δz = 1.2 mm is given by (D_{calc} - $D(0)$)/ϵ_0 = 0.09 V/nm, from Fig. 7.6(f). This gives an estimate of $\frac{\partial d_{blg}}{\partial \varepsilon}$ = -0.05 Å/% strain upon considering the maximum possible in-plane strain from the setup (ε = 1%). This would mean for an in plane tensile strain of 1%, the interlayer distance decrease by 1.5%, a factor of 5 different compared to Ref. [121], but on a similar order of magnitude . Ref. [121] considers interlayer distance to decrease by 0.33% for 1% of in-plane tensile strain.

In Fig. 7.6(f) we can see that the slope of D_{calc}/ϵ_0 versus Δz depends on the applied field($D(0)/\epsilon_0$). This is captured by the Eq. 7.12. The strain, ε is proportional to Δz. We considered ε = 1%, maximum possible from the setup. From Eq. 7.12 we can write,

$$\frac{\partial d_{blg}}{\partial \varepsilon} = -\Big(\frac{D(\varepsilon) - D(0)}{\epsilon_0 \varepsilon}\Big)\Big(\frac{\epsilon_0 d_{blg}(0)}{\epsilon_{blg}D(0)}\Big) \tag{7.14}$$

The Poisson ratio in the out of plane direction for BLG, ν_{blg} we get from the model is,

$$\nu_{blg} = \Big(\frac{1}{d_{blg}(0)}\Big)\frac{\partial d_{blg}}{\partial \varepsilon} = -\Big(\frac{D(\varepsilon) - D(0)}{\epsilon_0 \varepsilon}\Big)\Big(\frac{\epsilon_0}{\epsilon_{blg} D(0)}\Big) \tag{7.15}$$

As estimated above, for an in plane strain of 1%, the interlayer distance decrease by 15% (for an applied field $D(0)/\epsilon_0$), this gives ν_{blg} = -0.15.

2.Difference in scalar potential in two layers of BLG

Above, we assume that both layers in BLG are assumed to be under equal tensile strain. However, in the actual experiment, the strain is obtained by a bending of the substrate, so that the top and bottom layers might be strained differently. Some of the possibilities that can lead to non-equal strain in top and bottom layer of BLG are :

(a) If the edge contact is not equally mechanically coupled to the top and bottom layer of BLG then both layers can get differently strained for the same Δz (distance moved by wedge to bend the substrate)

(b) If we consider the BLG hall bar device to have a curvature with bending of the substrate, then its possible that top layer to be tensile strained and bottom layer to be under compressive strain (like in the plate bending model in Ch. 2)

Independent of the mechanism, if the top and bottom layer are strained differently, one can expect that the scalar potential in the two layers is different, resulting in an additional, strain induced electric field. The strain induced scalar potential results in shift of the chemical potential and the electrostatic potential such that the electrochemical potential remains the same. Thus,

$$\Delta\mu^{elch}(\varepsilon) = \Delta\mu^{elch}(0) \tag{7.16}$$

Let ε_t,ε_b represent the strain in the top and bottom layer of BLG. Let $\bar{\varepsilon}$ be the average tensile strain in the two layers of BLG, $\bar{\varepsilon} = (\varepsilon_t + \varepsilon_b)/2$ and let $\delta\varepsilon$ be the difference in tensile strain in the two layers, $\delta\varepsilon = \varepsilon_t$ - ε_b. Eq. 7.10 can be written as,

$$\frac{D(\bar{\varepsilon})}{\epsilon_0} = \frac{\epsilon_{blg}}{d_{blg}}(\Delta\mu^{elch}(0) - (\mu_t^{ch}(\bar{\varepsilon} + \delta\varepsilon/2) - \mu_b^{ch}(\bar{\varepsilon} - \delta\varepsilon/2))) \tag{7.17}$$

$$\frac{D(\bar{\varepsilon})}{\epsilon_0} = \frac{\epsilon_{blg}}{d_{blg}}(\Delta\mu^{elch}(0) - \Delta\mu^{ch}(0) - (\frac{\partial\mu_t^{ch}}{\partial\varepsilon}(\bar{\varepsilon}+\delta\varepsilon/2) - \frac{\partial\mu_b^{ch}}{\partial\varepsilon}(\bar{\varepsilon}-\delta\varepsilon/2))) \tag{7.18}$$

where $\frac{\partial \mu_t^{ch}}{\partial \varepsilon} = \frac{\partial \mu_b^{ch}}{\partial \varepsilon} = s_0/\mathrm{e}$, where s_0 is the scalar potential constant introduced in Ch. 6. The interlayer distance d_{blg} is assumed to remain same in this estimate. Thus

$$\begin{aligned} \frac{D(\bar{\varepsilon}) - D(0)}{\epsilon_0} &= \frac{\epsilon_{blg}\delta\varepsilon}{2ed_{blg}} s_0 \\ \frac{D(0)}{\epsilon_0} &= \frac{\epsilon_0 \epsilon_{blg}}{d_{blg}} (\Delta\mu^{elch}(0) - \Delta\mu^{ch}(0)) \end{aligned} \tag{7.19}$$

The dielectric constant(ϵ_{blg}) of BLG is ~ 3, the interlayer distance (d_{blg}) in BLG is ~ 3.4 Åand the scalar potential constant (s_0) for BLG is ~ 3.4 eV.

Let's consider the case where edge contacts are not equally coupled to the two layers of BLG. Thus upon increasing Δz, one layer get more strained compared to the other.

Let's consider the limit where $\delta\varepsilon$ is proportional to $\bar{\varepsilon}$, this happens when one layer is very weakly coupled and the other very strongly coupled to the edge contact. In that case we can write, $\delta\varepsilon = p\bar{\varepsilon}$, where p is the constant of proportionality from our assumption. Introducing this to Eq. 7.19 we get,

$$\frac{D(\bar{\varepsilon}) - D(0)}{\epsilon_0} = \frac{\epsilon_{blg} p}{2ed_{blg}} s_0 \bar{\varepsilon} \tag{7.20}$$

The average strain, $\bar{\varepsilon}$ is proportional to Δz. From Eq. 7.20, the slope of $D(\bar{\varepsilon})/\epsilon_0$ versus $\bar{\varepsilon}$ doesnot depend on the applied field, $D(0)/\epsilon_0$. But our observation in Fig. 7.6(f), the slope of the total electric field with strain depends on the applied field ($D(0)/\epsilon_0$). Thus, in this limit the estimate didn't captured the observation

In the limit of $\delta\varepsilon$ remaining constant with changing $\bar{\varepsilon}$, then Eq. 7.19 implies $D(\bar{\varepsilon})/\epsilon_0$ doesnot depend on $\bar{\varepsilon}$. But from Fig. 7.6(f), we can see that the total electric field increase with strain ($\bar{\varepsilon}$). So also in this limit, the estimate doesn't capture the observation.

Thus the possibility of difference in scalar potential in the two layers due to strain variation doesn't seem to capture the observation in Fig. 7.6(f).

3. Charge induced in BLG due to piezo electric nature of hBN

Monolayer hBN is shown to be a piezoelectric material using electrostatic force microscopy, with a charge induced to its surfaces when strained and the in plane piezo electric constant estimated is $2.91\times10^{-10}\mathrm{Cm}^{-1}$ [122–124]. But bilayer hBN, multilayer hBN are reported to be not piezo electric [123] with

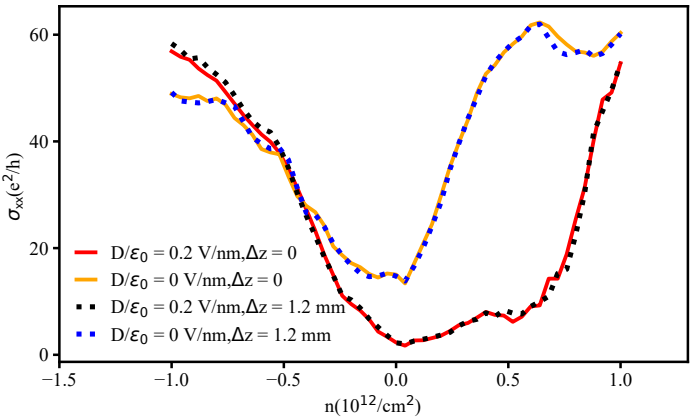

Figure 7.7 σ_{xx} versus n for D/ϵ_0= 0 ,0.2 V/nm for unstraining cycle. For the unstraining cycle from $\Delta z = 1.2$ mm to $\Delta z = 0$ mm the curve at D/ϵ_0 = 0.2 V/nm didn't reverted back to the initial state as in Fig. 7.6(b).

the same electrostatic force microscopy. The lack of inversion symmetry is considered to be the cause for piezoelectric behaviour in monolayer hBN. But multilayer hBN is used for stacking which in principle as from Ref. [123] is not piezoelectric. But still lets consider one of the layer of hBN out of the mutilayer becomes piezoelectric active with strain. This results in an induced polarization in the plane of hBN and it is not out of plane. The change we observed is in the applied out of plane electric field with strain. So the in plane polarization arising from strain in monolayer hBN doesn't seem to be the cause.

Thus out of the three possibilities, it seems the change in the interlayer distance in BLG under in plane strain captures the observation in Fig. 7.6(f).

7.2.3 Non-reversibility of the broadening around CNP with strain at finite D/ϵ_0

In the unstraining cycle, the shift observed in Fig. 7.6(b) was not reversibe. This non-reversibility observed in Fig. 7.6(b) can be due to :

(i) The top gate in the device is implemented by placing another 30 nm thick stack of Graphite/hBN on top of the pre-fabricated hBN/BLG/hBN stack(by method 2 discussed in subsec. 3.1.3) can possibly make the strain relaxation

in the unstraining cycle difficult. Thus the force released at the edge contact in the unbending cycle not enough to move the BLG to the initial unstrained state.

(ii) It can also be that with fabrication, the layers are all arranged may be not in a stable configuration [125] and with strain the layers could adjust to a new stable equilibrium arrangement. Thus, in the unstraining cycle it became difficult to return back to the intial arrangement making the effect not reversible.

(ii) other possibility includes the piezo electric behaviour reported in monolayer hBN as piezoelectric materials can show hysteritic behaviour. But multilayer hBN is non piezoelectric [123]. For the encapsulation, multilayer hBN is used, so this possibility can be neglected.

7.3 Strain effects in hBN/BLG moiré at finite D/ϵ_0

The bilayer graphene hall bar device with dual gate exhibited another resistive feature at higher charge carrier density (n) on both electron and hole side, shown in Fig. 7.8(a). One of the hBN layer is alligned with one of the graphene layers in the bilayer graphene system. The hBN and graphene have a lattice mismatch (δ) of 1.8% from their respective lattice constants. In addition there can be a twist angle (ϕ) between the two lattices. The secondary dirac point (sDP) is at a charge carrier density (n_s) $\sim 3.85\times10^{12}\text{cm}^{-2}$ and $n_s = 4/A_s$, where A_s is the area of super lattice and is given by $A_s = (\sqrt{3}/2)\lambda^2$. The moire superlattice spacing, λ is also given by [126],

$$\lambda = \frac{(1+\delta)a}{\sqrt{2(1+\delta)(1-cos\phi)+\delta^2}} \tag{7.21}$$

where ϕ is the rotation angle of BLG with respect to hBN and a (= 2.46 Å) is the lattice constant of graphene. The moire lattice spacing, λ = 10.95 nm. On combining the estimate for λ with Eq. 7.21 gives $\phi \sim 0.8°$.

The effect of applied electric field (D/ϵ_0) on resistivity at sDP as well as the effect of strain on it will be discussed in the following.

7.3.1 ρ_{xx} at finite D/ϵ_0

At finite electric field (D/ϵ_0), the resistivity at sDP on hole side (n_s = -3.85 $\times$ 10^{12}cm^{-2}) is larger compared to that at electron side ($n_s = 3.85 \times 10^{12}\text{cm}^{-2}$), can be seen in the four terminal resistivity (ρ_{xx}) map in Fig. 7.8(a). Also, the sDP resistivity in hole side is more broader than in the electron side along the n axis. The cross-section along D/ϵ_0 in the hole and electron side exhibits a

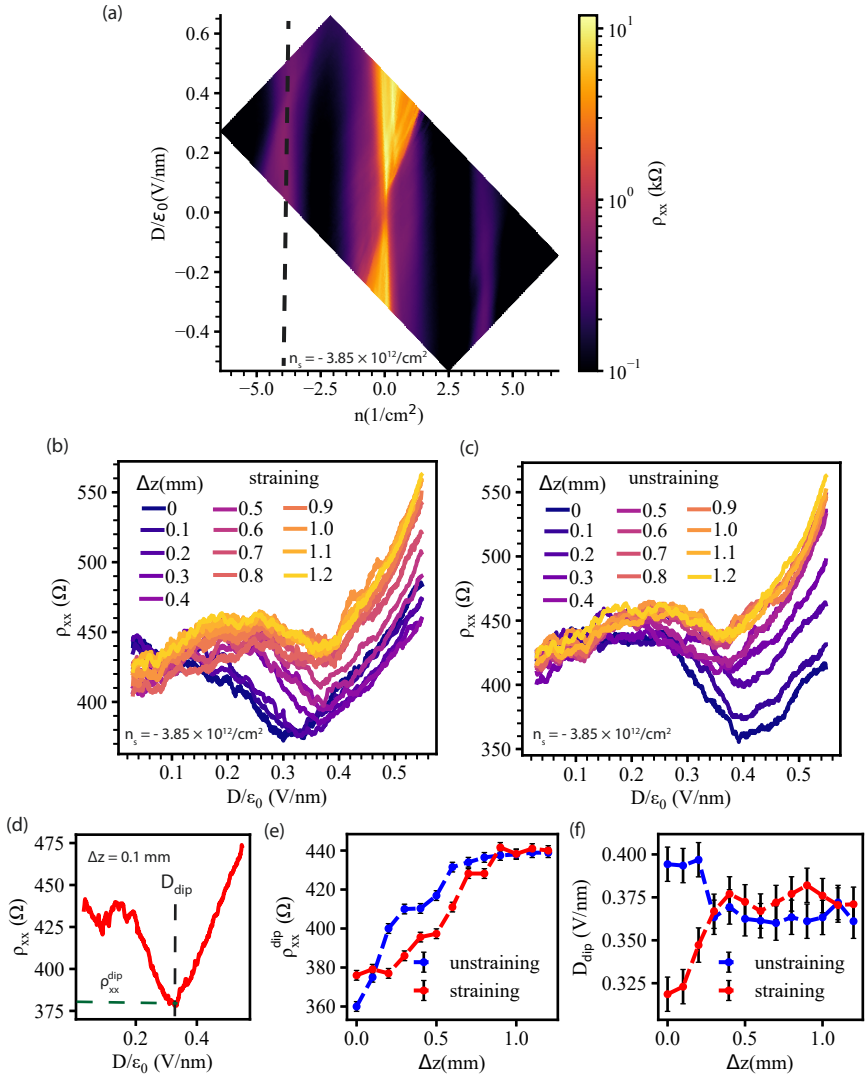

Figure 7.8 **(a)**Four terminal resistivity(ρ_{xx}) map in $n - D/\epsilon_0$ space for hBN/BLG moire device. In addition to main dirac point at $n = 0$ there are two other resistive region,secondary dirac point from moire at $|n_s| \sim 3.85 \times 10^{12}\text{cm}^{-2}$(hole side). **(b,c)** Cross section of ρ_{xx} map along D/ϵ_0 at n_s = -3.85 $\times$ 10^{12}cm^{-2} for straining and unstraining cycle. **(d)** Definition of ρ_{xx}^{dip} and D_{dip}.**(e,f)**ρ_{xx}^{dip} and D_{dip} plotted against Δz for straining and unstraining cycle.

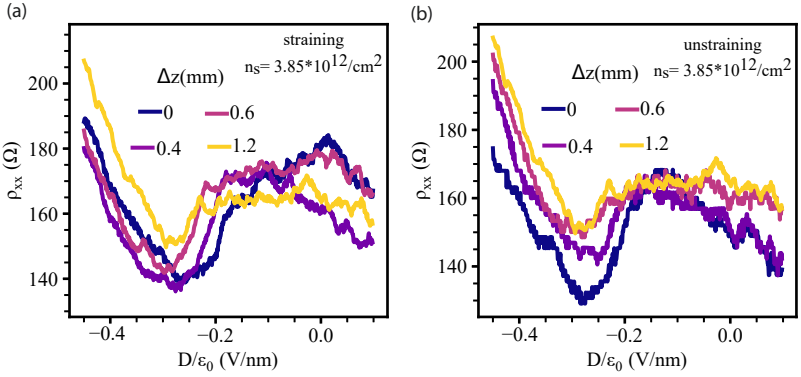

Figure 7.9 (a,b) Cross section of ρ_{xx} map along D/ϵ_0 at $n_s = 3.85 \times 10^{12}\text{cm}^{-2}$(electron side) for straining and unstraining cycle.

dip at finite D/ϵ_0, shown in Fig. 7.8(b) and 7.9(a), such a similar feature is reported in the same kind of device type in Ref. [127]. In the following, we look at possibilities for the origin of dip in ρ_{xx} and the effect of strain on this feature.

7

Dip in $\rho_{xx}(\rho_{xx}^{dip})$ at finite D/ϵ_0

In this part, we will try to see the possibilities that lead to the existense of dip in ρ_{xx} at finite electric field in the electron and hole side. Fig. 7.8(d) shows the ρ_{xx} versus D/ϵ_0 for the hole side at $\Delta z = 0.1$ mm, it shows the definition of ρ_{xx}^{dip} and D_{dip}. ρ_{xx}^{dip} is the resistivity at the dip and D_{dip} corresponds to the position of electric field (D/ϵ_0) at which dip occurs. In the hole side, ρ_{xx}^{dip} is located at $D/\epsilon_0 \sim 0.31$ V/nm for $\Delta z = 0$ and in the electron side, ρ_{xx}^{dip} is located at $D/\epsilon_0 \sim$ -0.26 V/nm for $\Delta z = 0$. Thus the dip occurs almost at symmetrically opposite electric field (D/ϵ_0) in the electron and hole side.

In the following we look at possibilities that can result in a change in ρ_{xx} with electric field (D/ϵ_0):

(i) Assuming one of the layers of BLG forming moiré with either top/bottom hBN, this already breaks the layer symmetry even when $D/\epsilon_0 = 0$. Depending on the sign of D/ϵ_0, the electron (n>0) or hole (n<0) wavefunction will be pushed to the upper or lower layer of BLG. In this case, when the wavefunction of charge carrier is pushed to the moire layer it will experience the additional spatially modulated moire potential which can lead to increase in

resistivity compared to transport in the opposite layer. If this is the case, then it should be a monotonic increase in resistivity but here the resistivity changes in a non-monotonic fashion in both electron and hole side with D/ϵ_0 (electric field).

(ii) The increase in ρ_{xx} with increase in D/ϵ_0 might be related to the gap opening at sDP. It has been shown that gap exists at sDP in hBN/graphene moiré superlattice in Ref. [128] from ARPES experiment due to inversion symmetry breaking. So it can also be that a similar gap opens in BLG/hBN moiré superlattice. Further application of electric field might change the interlayer interaction between the BLG and hBN and can result in changes in the gap. It might be that shape of the curve of ρ_{xx} versus D/ϵ_0 reflects the variation in gap at sDP due to the applied electric field. As the gap increases, ρ_{xx} increases.

The exact reason for the dip in ρ_{xx} at finite D/ϵ_0 couldn't be figured out so far.

7.3.2 Effect of strain on ρ_{xx}^{dip} , D_{dip}

In this section we look at the effect of strain on ρ_{xx}^{dip} and D_{dip}. Fig. 7.8(b),(c) shows the ρ_{xx} versus D/ϵ_0 for straining and unstraining cycle at the hole side. It can be seen that ρ_{xx}^{dip} increases with strain and seems reversible in the unstraining cycle. The corresponding ρ_{xx}^{dip} is plotted in Fig. 7.8(e). On an average ρ_{xx}^{dip} changes by $\sim$ 70 Ω from the straining and unstraining cycle. It shows a reversible trend but the magnitude exactly don't match. In the electron side it only changes by maximum of around $\sim$ 20 Ω, see Fig. 7.9(a),(b). This might indicate that BLG/hBN band structure at sDP is electron-hole asymmetric [127].

Fig. 7.8(f) shows the plot of D_{dip} versus Δz. The trend in D_{dip} with Δz seems not reversible upon comparing the straining and unstraining cycle. Now we will look at possibilities that can result in changes in ρ_{xx}^{dip} and D_{dip} with Δz (or strain).

First we discuss the changes in ρ_{xx}^{dip} with Δz. The possible effects of strain on ρ_{xx}^{dip} are :

(i) It can be that strain changes the interlayer distance between hBN and bilayer graphene (BLG), which might can result in changes of the moiré potential. If it results in an increase in the amplitude of moiré potential, then the electrons might feel this increase in modualtion potential and this might can increase resistivity.

(ii) It has been shown in graphene/hBN moire superlattice, gap opens at both main Dirac point as well as at secondar Dirac point(sDP) from the ARPES measurements in Ref. [128]. The gap opened is suspected to be induced by inversion-symmetry breaking. Also, the gap arising as a result of inversion symmetry breaking is shown to be dependent on the interlayer distance as it is shown from theory studies in Ref. [129], as interlayer distance decreases the gap induced increases. The decrease in interlayer distance between graphene and hBN results in increasing the strength of inversion symmetry breaking as the C atoms in the sublattice interacts more with B and N atoms of hBN. A similar effect can also be considered in the case of BLG/hBN interface under strain. Thus, the increase in ρ_{xx}^{dip} with strain can be an indicator of increase in gap opened at the sDP.

The effect on D_{dip} as mentioned above, it is not reversible. May be it's similar to the effect we observed in Fig. 7.6(f) and Fig. 7.7. The change in the interlayer distance in BLG might have resulted in shifting the position of electric field at which ρ_{xx}^{dip} occurs. In the unstraining cycle as discussed in subsec. 7.2.3, the interlayer distance of BLG didn't returned back resulting the D_{dip} to not change back to the intial value.

7.4 Summary

Tensile strain has an effect on the transport around the charge neutrality point (CNP) in BLG. The effect from strain induced scalar potential near CNP is already discussed in Ch. 6. The conductance around CNP seems to be sensitive to tensile strain and it shows an increase with strain. It seems, the mobility (μ) enhancement with strain in the regime where μ is proportioanl to V_{bg} results in the increase in conductance around CNP. Strain also shows an effect around CNP under finite electric field which breaks the interlayer symmetry in bilayer graphene(BLG). It seems that tensile strain results in an additional electric field in the system. For this finding, we discuss several possible mechanisms : change in interlayer distance of BLG, difference in scalar potential between the layers in BLG, piezoelectric nature of hBN. Based on the linear dependance of electric field (D/ϵ_0) with strain and the linear dependance of D/ϵ_0 on $D(\varepsilon = 0)/\epsilon_0$, we tentatively conclude that the bending also affects the interlayer distance of BLG, with an effective Poisson ratio of -0.15 in the z-direction at an applied electric field of 0.2 V/nm and in plane strain of 1%. The other discussed mechanisms like change in scalar potential in the two layers due to strain variation can result in a similar order of magnitude of electric field but doesnot capture the dependance on strain (ε) and the applied electric field ($D(\varepsilon = 0)/\epsilon_0$). The non-reversibility of the effect observed can be due to the hsyteresis at edge contact, as the top gated device has additional 30

nm thick Graphite/hBN stack on top which might have made it difficult to return back to the initial state after unstraining. The secondary dirac point (sDP) in the system at finite electric field also exhibited changes with strain. The dip in the resistivity at sDP for a fintie electric field is not understood yet. It can be related to bandgap change around sDP with the applied electric field. And with strain, the resistvity at the dip increases, which might indicate that bandgap at sDP increases with strain. It can be that strain also change the interlayer interaction between BLG and hBN by causing changes in the interlayer distance.

As the device structure involves more additions like top gate, it can also make the strain experiments non-reversible due to possible mechanical hysteresis. Improvement of device design for strain experiments in top gated devices is still something where there is room for improvement.

8 Strain pattern engineering

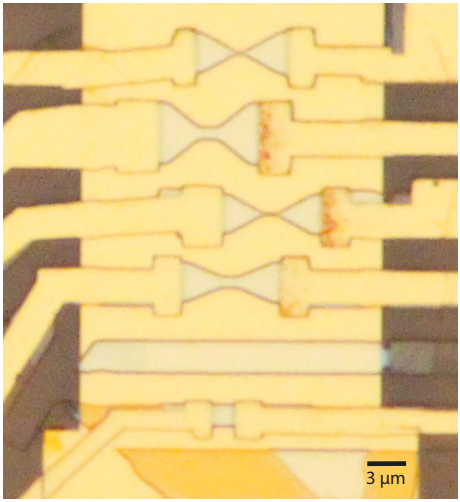

This chapter introduces the possibilities of controlled strain engineering in encapsulated graphene device junctions. The edge contacts play important role in inducing strain in the clamped 2D material, when the substrate is bent. First section discusses the possibility to enhance strain by exploiting the geometry of the device junctions. One such possibility is shown with Quantum Point Contact[1](QPC) shaped junctions, where the center region is narrower compared to the contact region which is wider. In addition to strain tuning, strain gradient tuning is demonstrated in two different geometries, a QPC device geometry and a trapezoid device geometry. QPC shaped device under strain results in strain gradient along the x-axis, whereas with trapezoid geometry it is possible to generate tunable strain gradient in y-axis. The technique of strain patterning opens up new possibilities for experiments in other 2D materials especially 2D semiconductors where strain can tune the band gap [93].

[1]Optical image of QPC shaped encapsulated graphene devices.

8.1 Introduction

The magnitude of strain itself plays an important factor in determining the type of strain effects that can be observed in the bandstructure of graphene [34]. A free-standing graphene lattice can withstand tensile strain upto 26-28% beyond which it will reach the fracture point [19, 21, 34]. However, in a device fabricated for charge carrier transport, metal-graphene edge contact interface is prone to mechanical fracture for a tensile strain close to 1% [91]. The maximum strain obtained from strain setup II is $\sim 0.13\%$, is it possible to enhance strain beyond this limit will be explored.

This chapter discusses the role of geometry of device junction in engineering strain as well as strain gradients. The Raman mapping experiments in this chapter are carried out at 1.6 K, in the newly designed attocube strain setup II, as described in Ch. 4.

8.2 Geometry as a strain engineering parameter

The strain generated in the graphene device junction is limited to the range of 0.1-0.2% for the maximum distance moved by piezo walkers to bend the substrate in strain setup II, shown in Sec. 4.9. The distance moved by piezo walker in strain setup II is represented by Δz (equivalent of distance moved by wedge in strain setup I). For the same Δz, force per unit width along the edge contact is assumed to be the same. The geometry of the device junction is another knob which can be used to check whether it is possible to enhance strain for the same Δz. A test experiment was carried out to check whether the variation in width along the length of junction can result in more strain at the narrower regions. If this is the case, then it would mean that the force acting along the edge contact is now distributed over a smaller width, resulting in more tensile strain in those regions. A quantum point contact (QPC) shaped junction are wider at the ends and narrow at center region. In this section, the strain distribution obtained in such QPC shaped junctions at room temperature and low temeprature will be discussed. Spatial Raman mapping of 2D peak position is used to obtain the strain distribution for different Δz, as shown in sec. 4.9.

8.2.1 Room temperature bending experiment

The design of the device junction is based on wider contact region followed by a narrow central region, as shown in the optical image of the device(J1) in Fig. 8.1(a) resembling a QPC(Quantum Point Contact) shaped device geometry. The width of junction at the edge contact side is 6 μm, and the width at center is 1.5 μm. The left and right side of the junction turned out to be

slightly asymmetric after fabrication.

A bending experiment with spatial Raman mapping is carried out to look into the evolution of strain pattern in the shaped junction. At $\Delta z = 2$ mm, the redshift of ω_{2D} at the center of junction is more than at the edge contact region, as shown in Fig. 8.1(d). The difference map shown in Fig. 8.1(e) between $\Delta z = 2$ mm and $\Delta z = 0$ mm tells about the relative spatial changes in ω_{2D} ($\Delta\omega_{2D}$) or in other terms its the spatial strain distribution. The shift of ω_{2D} (ω_{2D}) with Δz is used as a measure to quantify the tensile strain (ε) using $\frac{\partial\omega_{2D}}{\partial\epsilon}$ = -54 cm^{-1}/% strain [74], discussed in subsec. 2.5.3.

The width ratio of the junction at the center and edge contact region is 1:4. From our assumption, the force at the edge contact region is distributed at a narrower central region. Thus, force per unit width at the center of junction is four times than at the edge. In the linear stress - strain regime, force per unit width is proportional to strain. This means we can expect the centre of junction to be four times more strained than at the edge contacts.

The region close to the edge contact on either end of the junction is under strain of around 0.2% whereas at the center of the junction it is around 0.7-0.8%, see Fig. 8.1(d). This gives the ratio of strain at center to the edge contact region around 3.5-4. Thus, the estimate for the strain from force distribution carried out above almost matches with the strain distribution from experiment. The four corners of the junction along the contact edge are blue shifted compared to the center region or in other words four corners are the least strained region in the device area. One possibility is that the corner regions are free to move under the application of force by the edge contact, which might lead to less strain at the corners. Thus analysing the strain pattern can give indications to the boundary conditions in the system. On comparing such a shaped junction to a square/rectangle geometry (sec. 4.9), the force distributed per unit width of junction varies over the length of the junction.

Thus, with geometry it is possible to enhance strain locally for the same Δz. The force distribution seems to follow the inverse of width distribution of the junction along the length in such QPC shaped geometry resulting in more strain at the center compared to the edge contact region.

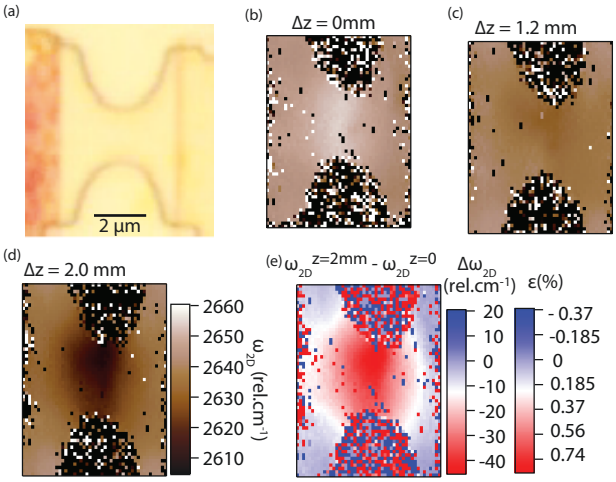

Figure 8.1 Spatial map of ω_{2D} in QPC shaped junction at room temperature. **(a)** Optical image of the device junction J1. **(b,c,d)** Spatial Raman map of ω_{2D} for bending distance $\Delta z = 0$, 1.2 mm,2 mm. **(e)** The difference of the spatial Raman map between $\Delta z = 2$ mm and at $\Delta z = 0$ mm. The redshift of ω_{2D} is more towards the center of J1 and thereby more tensile strain at the center.

8.2.2 Low temperature bending experiment

The same bending experiment was carried out at low temperature (1.6 K) to check whether a similar magnitude of strain can be obtained at the center of the junction. The change in width of the device junction J1 (Fig. 8.1(a)) from the edge contact side to center of junction is steep and this might have resulted in four corners to be the least strained region. So the shape of the junction is slightly modified by making a less steeper change in width from contact region to the central part of junction. The width of junction at the contact side is 2.6 μm and at the center of junction is $\sim$ 160 nm. Raman mapping carried out at low temperature in device junction (J2), is shown in Fig. 8.2(a). After $\Delta z > 2$ mm, there is a slight tilt in the raman mapping image, which appears to be an issue from the setup. The strain setup is fixed to the scanners for Raman mapping and the coaxial cable for the piezo walkers is connected to the outer titanium cage of the strain setup II. The issue looks like somehow the coaxial cable exert slight force on the scanners via the outer titanium cage of the strain setup. At low temperatures, the coaxial cables become stiff, and which may contribute to issue.

From Fig. 8.2(a), the overall distribution of strain (ε) in J2 looks similar to J1, as the central part of junction is under more tensile strain than near the contact edges. The cross section along x-axis through the center of junction at different positions along y-axis is shown in Fig. 8.2(b) for $\Delta z = 2.6$ mm, where the zero in the y-axis is taken to be at the center of the junction. The cross section overlaps except at few positions in x-axis, which can be due to slight strain variations in those particular regions along y-axis direction. The ω_{2D} at the center of the junction in J2 varies within 3 cm^{-1}, which in terms of $\varepsilon < 0.1\%$. Towards the left and right contact edges, the intial value of ω_{2D} is different, which can be due to either a different initial pre-strain at the contacts or different doping from the contacts to the graphene [100].

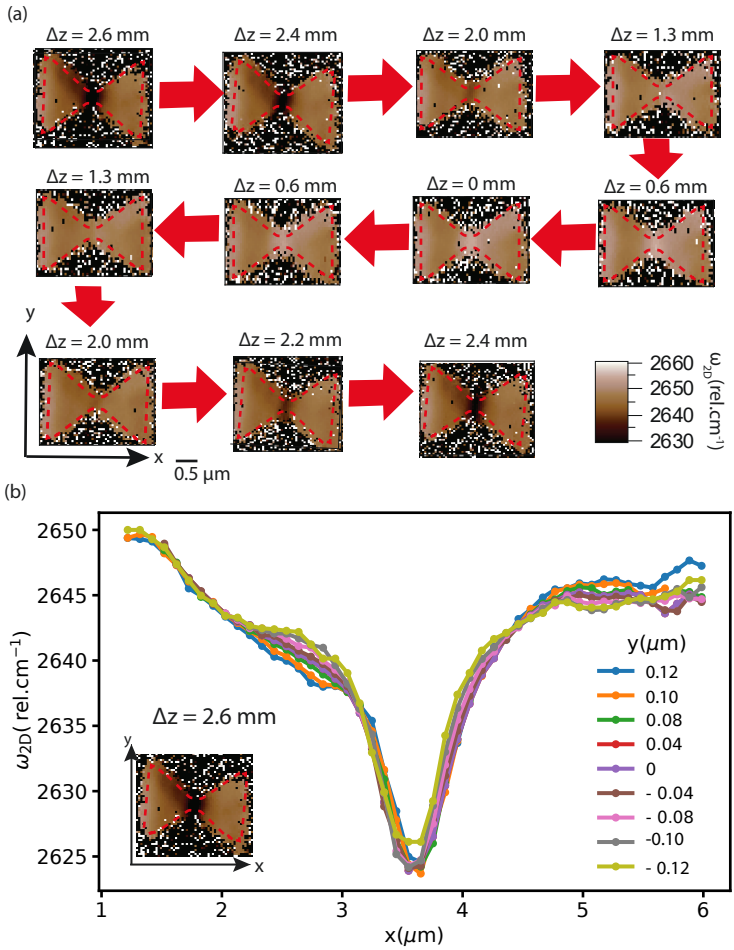

Figure 8.2 Spatial Raman mapping of junction J2 at low temperature.(a) Spatial Raman map of ω_{2D} for the unbending and bending cycle in J2 indicated by red arrows for the change in Δz. The red dotted lines marks the boundary of device. **(b)** Cross sections along x axis of the spatial ω_{2D} map at $\Delta z = 2.6$ mm for different positions at y axis. The center of the junction shows more redshift in ω_{2D} and thereby more tensile strain at the center. The zero in the y axis is taken at the center of junction.

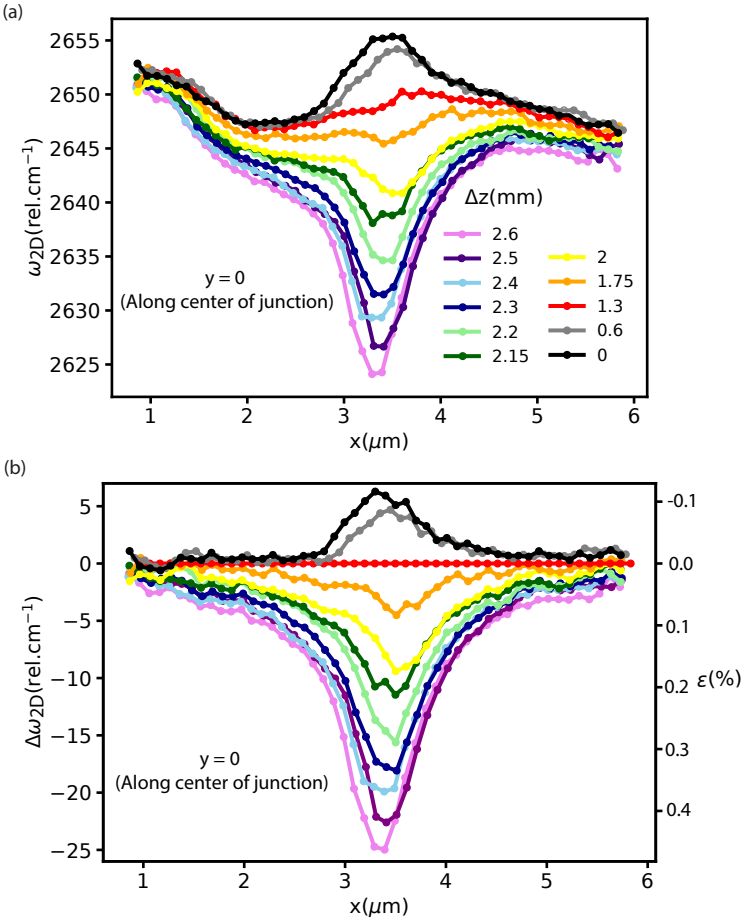

Figure 8.3 Evolution of cross-section of spatial Raman map of ω_{2D} at y = 0 with Δz in J2. (a) Cross section along x axis at y = 0 for different Δz from the spatial Raman maps in Fig. 8.2(a). The cross section shows that red shift of ω_{2D} depends on the position along x axis and the maximum occurs at the center of junction(x $\sim$ 3.4 μm). **(b)** Raman map at Δz = 1.3 mm is more uniform over the whole junction compared to that at Δz = 0, 0.6 mm where at the center of the junction ω_{2D} is blue shifted compared to the other regions. So the cross-section at Δz = 1.3 mm is chosen as the reference with respect to which changes in ω_{2D} will be described for other Δz. The plot shows change in $\omega_{2D}(\Delta\omega_{2D})$ on the left axis with respect to the cross section at Δz = 1.3 mm. The corresponding $\Delta\omega_{2D}$ is converted to strain(ε) on the right axis.

Fig. 8.3(a) shows cross, section of spatial raman map of J2 along x-axis at y = 0 for different Δz. For Δz = 0 and 0.6 mm the center region of J2 (x $\sim$ 3.2 μm) is blue shifted in ω_{2D} compared to the other regions. This feature is also present in J1 (Fig. 8.1(b)) at Δz = 0, where ω_{2D} in the center of the junction is blue shifted with respect to the other regions in the device junction. Intially when the device junction is not under tensile strain, the center of the junction is free from tension due to clamping which is present at the region near to edge contacts. At Δz = 1.3 mm, the spatial raman map is more uniform in comparison to that at Δz = 0 and 0.6 mm and thus the cross section at Δz = 1.3 mm is taken as a reference to describe the changes in the cross section of ω_{2D} ($\Delta\omega_{2D}$) for rest of the Δz. The corresponding plot is shown in Fig. 8.3(b). For Δz > 1.3 mm, the magnitude of $\Delta\omega_{2D}$ increases with Δz, and in terms of strain(ε) it can be read out from the axis in right of Fig. 8.3(b). The maximum strain obtained at the center of J2 is around 0.48%. The average of the ratio of strain at the center to the contact region on both the left and right side of the junction is around 8.9, from Fig. 8.3(b). The ratio of the width at contact region to that at the center is $\sim$ 16. But the strain obtained at the center is only around half of this factor. It might be possible that some part of the tensile force is lost against the friction at the interface of graphene-hBN [130], and not transferred to the central part of the junction. It can also be that at low temperature edge contacts are not able to exert the same force for the same bending as at room temperature, as the metals at the contact can be more rigid at low temperature, resulting in less strain at center compared to the estimate from width ratio.

At low temperature the magnitude of strain is less compared to room temperature (upon considering the width ratio estimates), it can be that edge contact is not able to pull the same way or it can also be a device to device variation due to difference in mechanical coupling of edge contacts to the graphene. The strain distribution nearly follows the inverse of width distribution along the junction at room temperature and but at low temperature it less than from the estimate. Such a strain distribution results in a strain gradient, which is discussed in next section.

8.3 Strain gradient

Apart from strain tuning, controlling the gradient of strain is also an important knob in strain related experiments. The pseudo magnetic field predicted and observed in STM experiments exist only in presence of strain gradient [38]. The idea of engineering strain gradients can be extended to the other van der Waals material like TMDCs for engineering spatially varying band gap [27, 28]. In this section, we will discuss about engineering strain gradients in x,y-axis

in the QPC shaped device geometry and in the trapezoid geometry.

8.3.1 QPC shaped geometry

In this geometry, the maximum tensile strain is at the center of the junction, as shown in Fig. 8.2(a). The distance moved by piezo walker in strain setup II is represented by Δz (equivalent of distance moved by wedge in strain setup I). For Δz = 2.6 mm, the cross sections in Fig. 8.2(b) shows that variation of ω_{2D} along y-axis is small especially near the center of junction and variation in strain will also follow the same trend. The cross section along x-axis shown in Fig. 8.3(b) shows the change in strain (ε) along x-axis of the device junction J2 for different Δz. The gradient of this distribution of ε(x) will give the strain gradient along x-axis and it is shown in Fig. 8.4(a). The strain gradient close to the center of device (x $\sim$ 3.1 μm - 3.6 μm) seems tunable with Δz. Upon increasing Δz, the strain gradient around the center region of junction increases. The magnitude of the maximum of strain gradient along x direction on either side of the center of the junction(x $\sim$ 3.4 μm) is plotted against Δz in Fig. 8.4(b). As mentioned in subsec. 8.2.2, Δz = 1.3 mm is taken as the reference for zero strain. So by changing Δ z from 1.3 mm to 2.6 mm lead to a change of strain gradient by 0.6%/μm around the center of junction (at x $\sim$ 3.1 μm , x $\sim$ 3.4 μm).

Calculating the absolute change in length

The absolute change in length of the graphene under strain can be calcualted if the strain distribution is known. By integrating the strain profile along the x-axis in Fig. 8.3(b) gives the absolute change in length of the graphene under tensile strain.

Let dx represent a length element along the x-axis. Upon tensile strain the length of the element changes by δx. The tensile strain, $\varepsilon = \delta$x/dx. Thus,

$$\delta x = \varepsilon dx \tag{8.1}$$

$$\Delta L_x = \int_0^L \delta x = \int_0^L \varepsilon(x)\ dx \tag{8.2}$$

where L is the total length of the junction, ΔL_x is the total change in length under tensile strain, ε(x) is the strain profile. The length of the junction J2 is 4.9 μm. The plot of ΔL_x versus Δz is shown in Fig. 8.4(d). The maximum ΔL_x obtained is 33 nm for Δz = 2.6 mm.

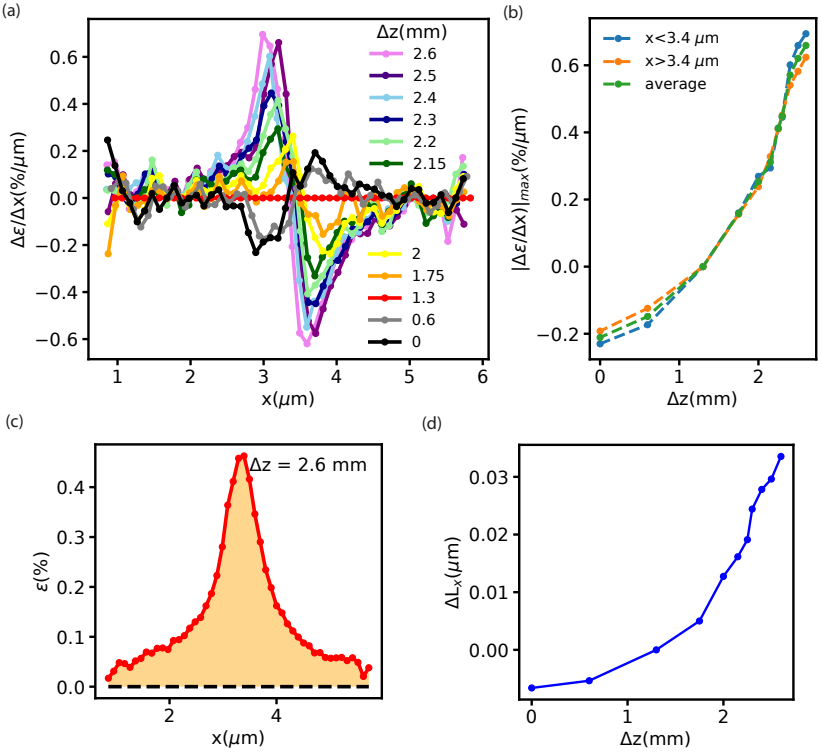

Figure 8.4 Strain gradient distribution in J2. **(a)** The gradient of the ε along the x axis in Fig. 8.3(b) is plotted for different Δz. The gradient is maximum around the center of junction (x = 3.4 μm) at x $\sim$ 3.1 μm and x $\sim$ 3.4 μm. **(b)** The magnitude of the maximum of gradient about the center of junction J2 plotted against Δz. A tunable strain gradient is possible in this geometry near the center of J2. **(c)** Strain distribution along x-axis in J2 at y = 0 for Δz = 2.6 mm,from Fig. 8.3(b). The area under ε(x) gives the absolute change in length of the device junction J2. **(d)** The change in length of junction J2 (ΔL_x) calculated from the integration of ε(x) curve for different Δz. Since the reference chosen is at Δz = 1.3 mm, the corresponding ΔL_x = 0. For Δz = 0 and 0.6 mm, the calculated ΔL_x is negative indicating initally the junction is slightly under less tensile strain that can be seen as a blue shift in ω_{2D} in the central region in J2 (discussed in subsec. 8.2.2).

Comparison with a wider QPC geometry

A comparison based on the width of the central region in QPC shaped junction on strain and strain gradient distribution between two junctions is carried out. The junction J3 is of same geometry type as J2 but with twice the width of the central region in J2. The schematic of the device junctions J2 and J3 are shown in Fig. 8.5(b).

The cross section of the Raman map through y= 0 at $\Delta z = 2.6$ mm is compared for J2 and J3 in Fig. 8.5(c). The maximum strain at the center of junction differs only by $\sim 0.06\%$. But away from center, J3 shows more extended distribution of strain in comparison to J2. In other terms, the tensile strain is more distributed around the center of junction in J3 whereas it is a sharp increase in strain towards the center of junction in the narrow J2 junction. This is reflected in the strain gradient plot in Fig. 8.5(d).

Thus, a tunable strain gradient around the center of junction is engineered with QPC shaped device geometry. It seems a wider center region of such QPC shaped junction results in broader distribution of strain along the length of junction compared to a narrow one resulting in less strain gradient for the former compared to later. Also, knowing the strain distribution can be used to calculate the actual change in length of the graphene under strain.

8.3.2 Trapezoidal geometry

The device junction with trapezoidal geometry contains a shorter and a longer length edge. The force exerted by the edge contacts upon bending the substrate is assumed to be same along the y-axis for a given edge. Thus force per unit width (f) is assumed to be uniform along the y direction. If we consider the trapezoid as a combination of strips of width dW and length L_y at position y along x axis. The Hooke's law for a strip at a given position in y can be written as,

$$f dW = \kappa dL_y \tag{8.3}$$

where κ is the in-plane stiffness constant of graphene or it is the two-dimensional Young's Modulus [19, 21], dL_y is the change in length of the strip element at position y. This can be modified to get the strain of each strip,

$$\frac{f dW}{L_y} = \frac{\kappa dL_y}{L_y} = \kappa \varepsilon_y \tag{8.4}$$

$$\varepsilon_y = \frac{f dW}{\kappa L_y} \tag{8.5}$$

where ε_y is the tensile strain on the strip at position y. As show in Fig. 8.6(b), length of bottom edge is less than at the top edge, $L_{yb} < L_{yt}$. Thus strain in

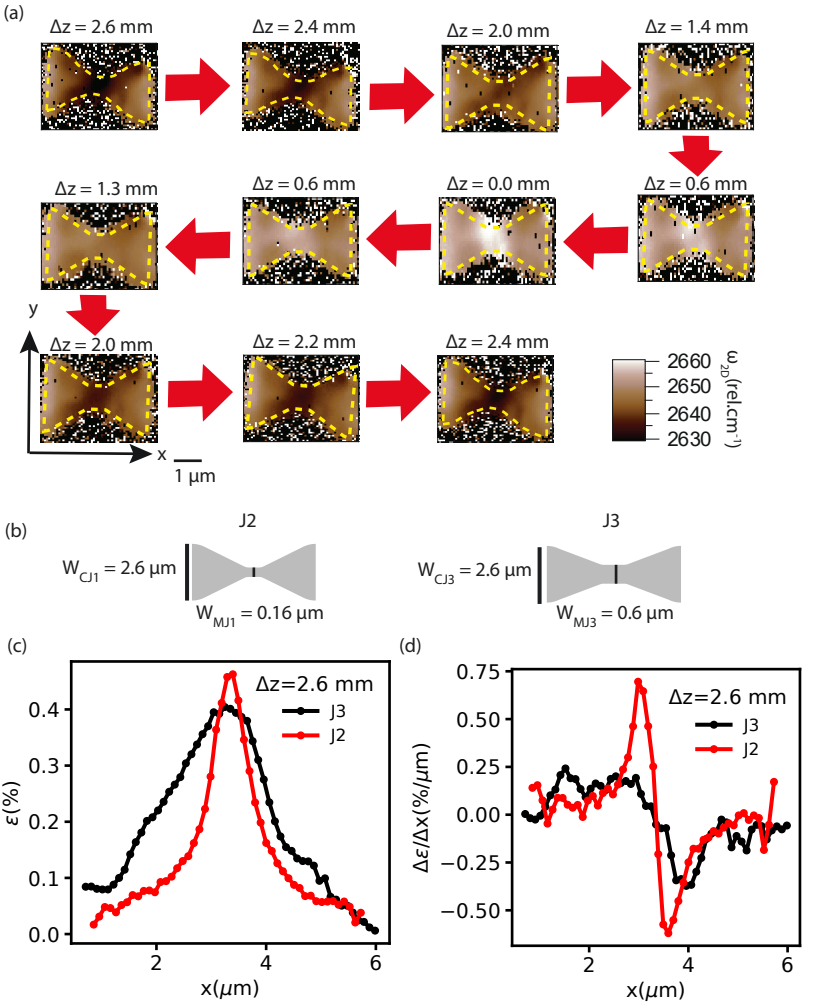

Figure 8.5 Strain and strain gradient comparison in QPC shaped junctions J2,J3. **(a)** Spatial Raman map of ω_{2D} for the unbending and bending cycle in J3 indicated by red arrows for the change in Δz. The yellow dotted lines mark the boundary of device. **(b)** The schematic of the geometry of the device junction J2 , J3. J3 is more wider at the center of junction.**(c)** Strain distribution along x axis at y = 0 for $\Delta z = 2.6$ mm in J2 , J3. **(d)** Strain gradient distribution in J2 and J3 for $\Delta z = 2.6$ mm. J3 has a broader distribution in strain resulting in less strain gradient in comaprison to J2.

the bottom and top edge follows : $\varepsilon_y(\ L_{yb}) > \varepsilon_y(L_{yt})$.

From the Raman maps in Fig. 8.6(a), we see that the shorter bottom edge to be more strained compared to the top edge which is longer. Fig. 8.6(b) shows the cross section at different positions in x-axis as shown in the schematic of the device junction. As Δz increases, ω_{2D} redshifts, see Fig. 8.6(b) and the amount of redshift depends on the position in y axis. This indicates that there is a strain gradient along y-axis direction. The redshift in ω_{2D} is converted to ε the same way as described in the previous sections. Fig. 8.6(c) shows the plot of ε along the width of trapezoid at positions in x-axis marked by the color in the schematic(Fig. 8.6(b)). The strain gradient along the y direction is around $\sim 0.016\%/\mu$m for Δz = 0.6 mm.

Thus, trapezoid geometry can be used to engineer strain gradient along y-axis in Cartesian coordinates.

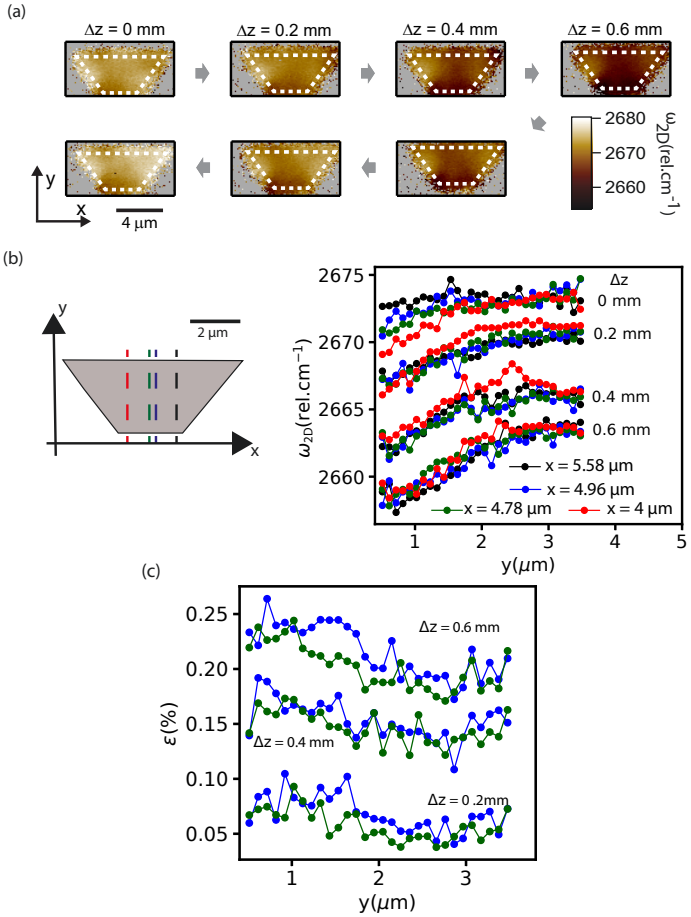

Figure 8.6 Straining a trapezoid device geometry. **(a)** Spatial Raman map of ω_{2D} in trapezoid shaped device junction for bending and unbending cycle indicated by the arrow for change in Δz. **(b)** Schematic of the device junction on the left side and on right side the cross section of ω_{2D} map along y direction for different Δz at positions in x axis indicated by dotted lines in the schematic. **(c)** The change in ω_{2D} converted to strain(ε) as described in Sec. **??**. The variation of ε along y axis is plotted for different Δz at positions marked by green and blue dotted line in the schematic of device in (b). The zero in the y axis is taken at the bottom edge of the trapezoid. For $\Delta z = 0.6$ mm , ε develops slope along the width direction y resulting in a strain gradient along y and it is $\sim 0.016\%/\mu$m.

8.4 Summary

The maximum strain generated in a square shape geometry with strain setup II at low temeprature (1.6 K) is $\sim$ 0.13%. For the same bending in a QPC shaped geometry, a maximum of $\sim$ 0.4-0.5% strain is generated at it's center region, at 1.6 K. So, with geometry of the device junction one could locally enhance the strain in the device area. The strain distribution in QPC geometry follows the inverse of width distribution along the length of the junction. In addition to tuning of strain, the control on strain gradient is also demonstrated with QPC and trapezoid device geometry. Thus we are able to engineer strain and strain gradient parallel and perpendicular to the current direction in a device.

Control on strain gradient can be a significant tuning knob for strain experiments in the future for pseudo magnetic field [38] or in spatial band gap engineering in TMDcs [27, 28]. But we are still limited by the magnitude of strain within 1% in the setup which in turn control the magnitude of the effects observed.

9 Summary and Outlook

This doctoral thesis is focussed on applying strain to electronic (quantum) devices in a controlled and in-situ tunable manner, with the aim of disentangling strain effects in the active material from other, less interesting effects. We will use mainly graphene or bilayer graphene as a test structure, because the changes in the bulk properties with strain can be fairly directly understood considering the corresponding C-C bond elongations, which is less intuitive in more complex. A major part of the thesis looked into how to implement controlled in-situ straining in practice, focussed on van der Waals materials. In Ch. 4 we demonstrated the design, working of fully home built three point bending setup (strain setup II) and how strain is generated in graphene using this setup. The bending setup is combined with optics for confocal Raman microscopy in the attodrY2100 system from Attocube. The optics in the system can accomodate polarization specific equipments. This new system allows us to map the strain patterns using Raman microscopy at low temperature and high magnetic fields along with the charge carrier transport or other optics experiments in the setup.

The tensile strain has an impact on both the lattice of graphene and bilayer graphene (BLG) as well as on the graphene-metal (Cr/Au) contact interface. Ch. 5 showcases the effect of strain on graphene-metal (Cr/Au) edge contact, which is visible in the two terminal differential conductance measurements. Absence of similar changes in four terminal measurements shows that the effect is possibly from edge contact interface. Also, the effects due to these changes at interface seems to not affect the features at low carrier density where the graphene channel dominates in conductance. The tensile strain seems to improve the contact properties in terms of conductivity towards larger gate voltage before the breaking limit of contact interface is reached. Strain can have an impact on the contact properties through reduction in barriers at the interface or through changes in chemical bond but the exact mechanism for the effect oberved is still a question.

In Ch. 6 and Ref. [35] we show one of the effects of strain observed on the crystal lattice of graphene that is the scalar potential. A similar effect observed in BLG is also presented and compared to single layer graphene. In

transport it appear as shift of charge neutralilty point (CNP) in gate voltage or any other feature in conductance stemming from the bandstructure of the system. The shift of CNP observed with strain is not due to bending induced changes in the gate capacitance as in that case the shift of a given feature should have scaled with the gate voltage. The strain induced scalar potential shifts the Dirac cone down in energy. It can be understood as arising due to changes in the next nearest neighbour hopping with strain which describes the changes in on site energy of the sublattice atoms. The rate of change of scalar potential with strain, defined as scalar potential constant is of similar magnitude in both graphene and bilayer graphene (BLG).

Interlayer interaction makes BLG special compared to graphene and it posses additional degree of freedom of interlayer symmetry. Ch. 7 first showcases the effect of strain on the transport around CNP. The increase in conductance around CNP can be due to the mobility enhancement with strain around CNP. Around CNP, the transport is limited by the mobility as it is linearly dependant on charge carrier density upto a certain gate voltage before mobility saturates and with strain, mobility in this regime increased. This can be similar to strain enhancement of mobility by reduction in strain fluctuations [53]. The dual gating is implemented in BLG devices to access control over charge carrier density and electric field in the system. Further, when the interlayer symmetry is broken with electric field, the strain seems to take the role of electric field by increasing the broadening of conductivity curve along charge carrier density (n). Few possibilities were discussed, that will lead strain to generate an additional electric field in the system including change in interlayer distance of BLG, difference in scalar potential between the layers in BLG, piezoelectric nature of hBN. Thus the total electric field includes the applied electric field and the additional field generated due to strain. Based on the linear dependance of total electric field (D/ϵ_0) with strain and the linear dependance of total electric field (D/ϵ_0) on the applied electric field ($D(\varepsilon = 0)/\epsilon_0$), we tentatively conclude that the bending also affects the interlayer distance of BLG, with an effective Poisson ratio in the z-direction of -1.5 at an applied electric field of 0.2 V/nm and for an in plane strain of 1%. The other possibilities doesnot captured the linear dependance of the total electric field on applied electric field and strain. But the effect observed is non-reversible in strain. The device structure with top gate includes an additional 30 nm of Graphite/hBN stack on top of the hBN/BLG/hBN stack, this might have made the strain relaxation in the unstraining cycle difficult. Thus the force released at the edge contact in the unbending cycle not enough to move the BLG to the initial unstrained state.

The experiments so far discussed all relied on strain as the tuning knob. We demonstrate in Ch. 8, the further possibility of tunable strain gradient as a

knob for the future experiments with strain. Strain gradients can be utilized to create engineered electric field and magnetic fields [38] in the crystal lattice through scalar potential and magnetic vector potential gradient. By making use of geometry as an additional parameter, strain gradients along a desired direction in xy-plane can be made possible. We demonstrate with a QPC shaped geometry and trapezoid geometry the possibility to engineer tunable strain gradients along x,y direction in Cartesian coordinates.

Outlook

The work done in the thesis shows tunable strain control on the fabricated device junctions in the size range from 150 nm to 7 μm. The effects observed were not only from the lattice but also from the edge contact interface. But these effects on contacts seems to not affect the features at low carrier density and that in four probe measurements and this helped to disentagle the effects. The non-reversibility of the effects observed in top gated BLG device implies the room for improvement in desigining such devices for strain experiments. Also demonstrated the strain induced scalar potential effect on graphene and bilayer graphene lattices. The technique of straining developed in the thesis can be extended beyond graphene to other van der Waals material system. A different material system will have a different bandstructure and the effect of strain on other material system could be studied with the setup which can combine charge carrier transport along with the optical experiments.

CrSBr, a van der Waals magnet, with strain of the order of 1% has reported to show magnetic phase transition [32] from antiferromagnetic to ferromagnetic state. The transport signatures under such phase transitions can be studied with strain as the knob. In addition to transport, the optical experiments combined with polarization optics can be utilized to look into the phase transition with more probes.

Quantum capacitance measurement [131] combined with strain can be an experiment to know changes in density of states around CNP in BLG and thereby know the effect of tensile strain on the mass of charge carriers. Or one needs to combine scanning tunneling spectroscopy on strained lattices [132] to detect the changes in density of states with tensile strain. These experiments can give an insight whether the strain of order of 1% result in observable change in mass of the charge carriers in BLG.

The possibility of generating strain gradient can be extended to TMDCs to create regions of different band gap. One potential application of this can be in the exciton funneling experiments [133]. The strain gradient creating wide range of band gap in such material system makes it possible to absorb radia-

tions in a larger range of wavelength, thus making a possibility in enhancing the capability of existing solar cells.

One another possibility is developing strain sensors based on piezo electric 2D materials. The single layer of 2D material like hBN, MoS_2 are piezo electric [122]. The in palne strain can induce poalrization in such systems which can be used to sense the strain.

Bibliography

[1] B. L. Ooi, J. M. Gilbert, and A. R. A. Aziz, Acta Mechanica Sinica **32**, 670 (2016).

[2] A. C. To, X. Liang, and W. Dong (2023) pp. 219–265.

[3] J. Moreland and J. W. Ekin, Journal of Applied Physics **58**, 3888 (1985).

[4] C. J. Muller, J. M. van Ruitenbeek, and L. J. de Jongh, Phys. Rev. Lett. **69**, 140 (1992).

[5] J. M. van Ruitenbeek, A. Alvarez, I. Piñeyro, C. Grahmann, P. Joyez, M. H. Devoret, D. Esteve, and C. Urbina, Review of Scientific Instruments **67**, 108 (1996).

[6] S. A. G. Vrouwe, E. van der Giessen, S. J. van der Molen, D. Dulic, M. L. Trouwborst, and B. J. van Wees, Phys. Rev. B **71**, 035313 (2005).

[7] S. Dolabella, A. Borzì, A. Dommann, and A. Neels, Small Methods **6**, 2100932 (2022).

[8] T. Vogelsang and K. R. Hofmann, IEEE Transactions on Electron Devices **39**, 2641 (1992).

[9] Y. Sun, S. E. Thompson, and T. Nishida, J. Appl. Phys. **101**, 104503 (2007).

[10] Y.-C. Yeo, in *Proceedings. 7th International Conference on Solid-State and Integrated Circuits Technology, 2004.*, Vol. 1 (2004) pp. 310–314 vol.1.

[11] C. H. Diaz, ECS Transactions **2**, 341 (2006).

[12] K.-W. Ang, C. H. Tung, N. Balu, G. Samudra, and Y.-C. Yeo, Electron Device Letters, IEEE **28**, 609 (2007).

[13] J. Munguía, G. Bremond, J. M. Bluet, J. M. Hartmann, and M. Mermoux, Appl. Phys. Lett. **93**, 102101 (2008).

[14] L. Balaghi, G. Bussone, R. Grifone, R. Hübner, J. Grenzer, M. Ghorbani-Asl, A. V. Krasheninnikov, H. Schneider, M. Helm, and E. Dimakis, Nature Communications **10**, 2793 (2019).

[15] Y. Chen, Y. Lei, Y. Li, Y. Yu, J. Cai, M.-H. Chiu, R. Rao, Y. Gu, C. Wang, W. Choi, H. Hu, C. Wang, Y. Li, J. Song, J. Zhang, B. Qi, M. Lin, Z. Zhang, A. E. Islam, B. Maruyama, S. Dayeh, L.-J. Li, K. Yang, Y.-H. Lo, and S. Xu, Nature **577**, 209 (2020).

[16] H.-S. Kim and N.-G. Park, NPG Asia Materials **12**, 78 (2020).

[17] H. Hu, S. Zhou, H. Wan, X. Liu, N. Li, and H. Xu, Scientific Reports **9**, 3447 (2019).

[18] C. Androulidakis, K. Zhang, M. Robertson, and S. Tawfick, 2D Materials **5**, 032005 (2018).

[19] C. Lee, X. Wei, J. W. Kysar, and J. Hone, Science **321**, 385 (2008).

[20] A. Falin, Q. Cai, E. J. G. Santos, D. Scullion, D. Qian, R. Zhang, Z. Yang, S. Huang, K. Watanabe, T. Taniguchi, M. R. Barnett, Y. Chen, R. S. Ruoff, and L. H. Li, Nature Communications **8**, 15815 (2017).

[21] K. Cao, S. Feng, Y. Han, L. Gao, T. Hue Ly, Z. Xu, and Y. Lu, Nature Communications **11**, 284 (2020).

[22] G. Plechinger, A. Castellanos-Gomez, M. Buscema, H. S. J. van der Zant, G. A. Steele, A. Kuc, T. Heine, C. Schüller, and T. Korn, 2D Materials **2**, 015006 (2015).

[23] J.-K. Lee, S. Yamazaki, H. Yun, J. Park, G. P. Kennedy, G.-T. Kim, O. Pietzsch, R. Wiesendanger, S. Lee, S. Hong, U. Dettlaff-Weglikowska, and S. Roth, Nano Lett. **13**, 3494 (2013).

[24] S. Yang, Y. Chen, and C. Jiang, InfoMat **3**, 397 (2021).

[25] L. Wang, S. Zihlmann, A. Baumgartner, J. Overbeck, K. Watanabe, T. Taniguchi, P. Makk, and C. Schönenberger, Nano Lett. **19**, 4097 (2019).

[26] M. Goldsche, G. J. Verbiest, T. Khodkov, J. Sonntag, N. v. d. Driesch, D. Buca, and C. Stampfer, Nanotechnology **29**, 375301 (2018).

[27] P. San-Jose, V. Parente, F. Guinea, R. Roldán, and E. Prada, Phys. Rev. X **6**, 031046 (2016).

[28] A. Castellanos-Gomez, R. Roldán, E. Cappelluti, M. Buscema, F. Guinea, H. S. J. van der Zant, and G. A. Steele, Nano Lett. **13**, 5361 (2013).

[29] R. Maiti, C. Patil, M. A. S. R. Saadi, T. Xie, J. G. Azadani, B. Uluutku, R. Amin, A. F. Briggs, M. Miscuglio, D. Van Thourhout, S. D. Solares, T. Low, R. Agarwal, S. R. Bank, and V. J. Sorger, Nature Photonics **14**, 578 (2020).

[30] A. Branny, S. Kumar, R. Proux, and B. D. Gerardot, Nature Communications **8**, 15053 (2017).

[31] Z. Wang, Q. Jingjing, X. Wang, Z. Zhang, Y. Chen, X. Huang, and W. Huang, Chem. Soc. Rev. **47**, 6128 (2018).

[32] J. Cenker, S. Sivakumar, K. Xie, A. Miller, P. Thijssen, Z. Liu, A. Dismukes, J. Fonseca, E. Anderson, X. Zhu, X. Roy, D. Xiao, J.-H. Chu, T. Cao, and X. Xu, Nature Nanotechnology **17**, 256 (2022).

[33] L. Wang, I. Meric, P. Y. Huang, Q. Gao, Y. Gao, H. Tran, T. Taniguchi, K. Watanabe, L. M. Campos, D. A. Muller, J. Guo, P. Kim, J. Hone, K. L. Shepard, and C. R. Dean, Science **342**, 614 (2013).

[34] S.-M. Choi, S.-H. Jhi, and Y.-W. Son, Phys. Rev. B **81**, 081407 (2010).

[35] L. Wang, A. Baumgartner, P. Makk, S. Zihlmann, B. S. Varghese, D. I. Indolese, K. Watanabe, T. Taniguchi, and C. Schönenberger, Communications Physics **4**, 147 (2021).

[36] R. M. Ribeiro, V. M. Pereira, N. M. R. Peres, P. R. Briddon, and A. H. Castro Neto, New Journal of Physics **11**, 115002 (2009).

[37] M. A. H. Vozmediano, M. I. Katsnelson, and F. Guinea, Physics Reports **496**, 109 (2010).

[38] S. Zhu, J. A. Stroscio, and T. Li, Phys. Rev. Lett. **115**, 245501 (2015).

[39] M. M. Fogler, F. Guinea, and M. I. Katsnelson, Phys. Rev. Lett. **101**, 226804 (2008).

[40] E. McCann and M. Koshino, Reports on Progress in Physics **76**, 056503 (2013).

[41] P. J. Zomer, M. H. D. Guimarães, J. C. Brant, N. Tombros, and B. J. van Wees, Applied Physics Letters **105**, 013101 (2014).

[42] C. R. Dean, A. F. Young, I. Meric, C. Lee, L. Wang, S. Sorgenfrei, K. Watanabe, T. Taniguchi, P. Kim, K. L. Shepard, and J. Hone, Nature Nanotechnology **5**, 722 (2010).

[43] A. H. Castro Neto, F. Guinea, N. M. R. Peres, K. S. Novoselov, and A. K. Geim, Rev. Mod. Phys. **81**, 109 (2009).

[44] K. Bhaskar and T. K. Varadan, "Classical Plate Theory," in *Plates: Theories and Applications* (Springer International Publishing, Cham, 2021) pp. 11–28.

[45] T. Ihn, *Semiconductor Nanostructures: Quantum states and electronic transport*, Semiconductor Nanostructures: Quantum States and Electronic Transport (OUP Oxford, 2009).

[46] A. Varlet, M. Mucha-Kruczyński, D. Bischoff, P. Simonet, T. Taniguchi, K. Watanabe, V. Fal'ko, T. Ihn, and K. Ensslin, Synthetic Metals **210**, 19 (2015).

[47] A. B. Kuzmenko, I. Crassee, D. van der Marel, P. Blake, and K. S. Novoselov, Phys. Rev. B **80**, 165406 (2009).

[48] Y. Zhang, T.-T. Tang, C. Girit, Z. Hao, M. C. Martin, A. Zettl, M. F. Crommie, Y. R. Shen, and F. Wang, Nature **459**, 820 (2009).

[49] E. McCann and V. I. Fal'ko, Phys. Rev. Lett. **96**, 086805 (2006).

[50] J. Martin, N. Akerman, G. Ulbricht, T. Lohmann, J. H. Smet, K. von Klitzing, and A. Yacoby, Nature Physics **4**, 144 (2008).

[51] Y.-W. Tan, Y. Zhang, K. Bolotin, Y. Zhao, S. Adam, E. H. Hwang, S. Das Sarma, H. L. Stormer, and P. Kim, Phys. Rev. Lett. **99**, 246803 (2007).

[52] R. Beams, L. G. Cançado, and L. Novotny, Journal of Physics: Condensed Matter **27**, 083002 (2015).

[53] L. Wang, P. Makk, S. Zihlmann, A. Baumgartner, D. I. Indolese, K. Watanabe, T. Taniguchi, and C. Schönenberger, Phys. Rev. Lett. **124**, 157701 (2020).

[54] B. Terrés, L. A. Chizhova, F. Libisch, J. Peiro, D. Jörger, S. Engels, A. Girschik, K. Watanabe, T. Taniguchi, S. V. Rotkin, J. Burgdörfer, and C. Stampfer, Nature Communications **7**, 11528 (2016).

[55] E. H. Hall, American Journal of Mathematics **2**, 287 (1879).

[56] K. v. Klitzing, G. Dorda, and M. Pepper, Phys. Rev. Lett. **45**, 494 (1980).

[57] S. Das Sarma, S. Adam, E. H. Hwang, and E. Rossi, Rev. Mod. Phys. **83**, 407 (2011).

[58] Y. Zhang, Y.-W. Tan, H. L. Stormer, and P. Kim, Nature **438**, 201 (2005).

[59] K. S. Novoselov, Z. Jiang, Y. Zhang, S. V. Morozov, H. L. Stormer, U. Zeitler, J. C. Maan, G. S. Boebinger, P. Kim, and A. K. Geim, Science **315**, 1379 (2007).

[60] K. S. Novoselov, E. McCann, S. V. Morozov, V. I. Fal'ko, M. I. Katsnelson, U. Zeitler, D. Jiang, F. Schedin, and A. K. Geim, Novosolev2006 **2**, 177 (2006).

[61] J. R. Williams, D. A. Abanin, L. DiCarlo, L. S. Levitov, and C. M. Marcus, Phys. Rev. B **80**, 045408 (2009).

[62] E. M. LIFSHITZ, A. M. KOSEVICH, L. P. PITAEVSKII, E. M. LIFSHITZ, A. M. KOSEVICH, and L. P. PITAEVSKII, in *Theory of Elasticity (Third Edition)* (Butterworth-Heinemann, Oxford, 1986) pp. 1–37.

[63] J.-B. Wu, M.-L. Lin, X. Cong, H.-N. Liu, and P.-H. Tan, Chem. Soc. Rev. **47**, 1822 (2018).

[64] E. Anastassakis, A. Pinczuk, E. Burstein, F. Pollak, and M. Cardona, Solid State Communications **88**, 1053 (1993).

[65] A. C. Ferrari, J. C. Meyer, V. Scardaci, C. Casiraghi, M. Lazzeri, F. Mauri, S. Piscanec, D. Jiang, K. S. Novoselov, S. Roth, and A. K. Geim, Phys. Rev. Lett. **97**, 187401 (2006).

[66] C. Lee, H. Yan, L. E. Brus, T. F. Heinz, J. Hone, and S. Ryu, ACS Nano **4**, 2695 (2010).

[67] L. G. Cançado, M. A. Pimenta, B. R. A. Neves, M. S. S. Dantas, and A. Jorio, PRL **93**, 247401 (2004).

[68] A. C. Ferrari and D. M. Basko, Nature Nanotechnology **8**, 235 (2013).

[69] M. Lazzeri, C. Attaccalite, L. Wirtz, and F. Mauri, Phys. Rev. B **78**, 081406 (2008).

[70] M. Lucchese, F. Stavale, E. M. Ferreira, C. Vilani, M. Moutinho, R. B. Capaz, C. Achete, and A. Jorio, Carbon **48**, 1592 (2010).

[71] J.-H. Zhong, J. Zhang, X. Jin, J.-Y. Liu, Q. Li, M.-H. Li, W. Cai, D.-Y. Wu, D. Zhan, and B. Ren, Journal of the American Chemical Society **136**, 16609 (2014).

[72] C. Thomsen and S. Reich, Phys. Rev. Lett. **85**, 5214 (2000).

[73] L. Malard, M. Pimenta, G. Dresselhaus, and M. Dresselhaus, Physics Reports **473**, 51 (2009).

[74] M. Mohr, K. Papagelis, J. Maultzsch, and C. Thomsen, Phys. Rev. B **80**, 205410 (2009).

[75] F. Guinea, Solid State Communications **152**, 1437 (2012).

[76] M. Oliva-Leyva and G. G. Naumis, Phys. Rev. B **88**, 085430 (2013).

[77] G. G. Naumis, S. Barraza-Lopez, M. Oliva-Leyva, and H. Terrones, Reports on Progress in Physics **80**, 096501 (2017).

[78] A. McRae, G. Wei, and A. Champagne, Phys. Rev. Appl. **11**, 054019 (2019).

[79] K. V. Zakharchenko, M. I. Katsnelson, and A. Fasolino, Phys. Rev. Lett. **102**, 046808 (2009).

[80] M. Farjam and H. Rafii-Tabar, Phys. Rev. B **80**, 167401 (2009).

[81] A. L. Kitt, V. M. Pereira, A. K. Swan, and B. B. Goldberg, Phys. Rev. B **85**, 115432 (2012).

[82] A. L. Kitt, V. M. Pereira, A. K. Swan, and B. B. Goldberg, Phys. Rev. B **87**, 159909 (2013).

[83] J. L. Mañes, PRB **76**, 045430 (2007).

[84] K. I. Bolotin, K. J. Sikes, Z. Jiang, M. Klima, G. Fudenberg, J. Hone, P. Kim, and H. L. Stormer, Solid State Communications **146**, 351 (2008).

[85] S. Lee, H. Choi, I. Moon, H. Shin, K. Watanabe, T. Taniguchi, and W. J. Yoo, Adv. Electron. Mater. **8**, 2101169 (2022).

[86] K. S. Novoselov, A. K. Geim, S. V. Morozov, D. Jiang, Y. Zhang, S. V. Dubonos, I. V. Grigorieva, and A. A. Firsov, Science **306**, 666 (2004).

[87] Y. Li, G. Kuang, Z. Jiao, L. Yao, and R. Duan, Materials Research Express **9**, 122001 (2022).

[88] T. Taniguchi and K. Watanabe, Journal of Crystal Growth **303**, 525 (2007).

[89] Z. H. Ni, H. M. Wang, J. Kasim, H. M. Fan, T. Yu, Y. H. Wu, Y. P. Feng, and Z. X. Shen, Nano Lett. **7**, 2758 (2007).

[90] S. Zihlmann, *Spin and charge relaxation in graphene*, Ph.D. thesis, University_of_Basel (2018).

[91] L. Wang, *Quantum transport experiments in strain-engineered graphene*, Ph.D. thesis, University of Basel (2019).

[92] Y. Sun, J. Pan, Z. Zhang, K. Zhang, J. Liang, W. Wang, Z. Yuan, Y. Hao, B. Wang, J. Wang, Y. Wu, J. Zheng, L. Jiao, S. Zhou, K. Liu, C. Cheng, W. Duan, Y. Xu, Q. Yan, and K. Liu, Nano Lett. **19**, 761 (2019).

[93] H. J. Conley, B. Wang, J. I. Ziegler, R. F. J. Haglund, S. T. Pantelides, and K. I. Bolotin, Nano Lett. **13**, 3626 (2013).

[94] Z. Xie, W. Xue, H. Chen, and Y. Huang, Ceramics International **37**, 2165 (2011).

[95] G. K. White and M. L. Minges, International Journal of Thermophysics **18**, 1269 (1997).

[96] W. Wang, R. Huang, Y. Zhao, H. Liu, C. Huang, X. Yang, Y. Shan, X. Zhao, and L. Li, Journal of Alloys and Compounds **740**, 47 (2018).

[97] Q. Wang and F. Li, Scripta Materialia **191**, 67 (2021).

[98] K. Wang and R. Reeber, High Temperature and Materials Science **35**, 181 (1996).

[99] D. Wang, Y. Fotinich, and G. P. Carman, Journal of Applied Physics **83**, 5342 (1998).

[100] J. Sonntag, K. Watanabe, T. Taniguchi, B. Beschoten, and C. Stampfer, Phys. Rev. B **107**, 075420 (2023).

[101] Y. Khatami, H. Li, C. Xu, and K. Banerjee, IEEE Transactions on Electron Devices **59**, 2444 (2012).

[102] K. Nagashio, T. Nishimura, K. Kita, and A. Toriumi, Appl. Phys. Lett. **97**, 143514 (2010).

[103] C. V. Morfonios, P. Schmelcher, C. V. Morfonios, and P. Schmelcher, in *Control of Magnetotransport in Quantum Billiards: Theory, Computation and Applications* (Springer International Publishing, Cham, 2017) pp. 37–58.

[104] Y. Wang, J. Lei, and Z. Liu, Diamond and Related Materials **93**, 66 (2019).

[105] Q. Gao and J. Guo, APL Mater. **2**, 056105 (2014).

[106] M. S. Choi, N. Ali, T. D. Ngo, H. Choi, B. Oh, H. Yang, and W. J. Yoo, Adv. Mater. **34**, 2202408 (2022).

[107] Z.-Z. Cao, Y.-F. Cheng, and G.-Q. Li, Appl. Phys. Lett. **101**, 253507 (2012).

[108] W.-R. Hannes, M. Jonson, and M. Titov, Phys. Rev. B **84**, 045414 (2011).

[109] R. Frisenda, G. D. Harzmann, J. A. Celis Gil, J. M. Thijssen, M. Mayor, and H. S. J. van der Zant, Nano Lett. **16**, 4733 (2016).

[110] F. de Juan, M. Sturla, and M. A. H. Vozmediano, Phys. Rev. Lett. **108**, 227205 (2012).

[111] M. Huang, H. Yan, T. F. Heinz, and J. Hone, Nano Lett. **10**, 4074 (2010).

[112] D. Grassano, M. D'Alessandro, O. Pulci, S. G. Sharapov, V. P. Gusynin, and A. A. Varlamov, Phys. Rev. B **101**, 245115 (2020).

[113] X. He, N. Tang, X. Sun, L. Gan, F. Ke, T. Wang, F. Xu, X. Wang, X. Yang, W. Ge, and B. Shen, Appl. Phys. Lett. **106**, 043106 (2015).

[114] F. Guinea, A. K. Geim, M. I. Katsnelson, and K. S. Novoselov, Phys. Rev. B **81**, 035408 (2010).

[115] W. Zhu, V. Perebeinos, M. Freitag, and P. Avouris, Phys. Rev. B **80**, 235402 (2009).

[116] T. Ando, J. Phys. Soc. Jpn. **80**, 014707 (2010).

[117] J.-H. Chen, C. Jang, S. Adam, M. S. Fuhrer, E. D. Williams, and M. Ishigami, Nature Physics **4**, 377 (2008).

[118] E. Icking, L. Banszerus, F. Wörtche, F. Volmer, P. Schmidt, C. Steiner, S. Engels, J. Hesselmann, M. Goldsche, K. Watanabe, T. Taniguchi, C. Volk, B. Beschoten, and C. Stampfer, Adv. Electron. Mater. **8**, 2200510 (2022).

[119] M. A. Aamir and A. Ghosh, 2D Materials **6**, 025018 (2019).

[120] E. J. G. Santos and E. Kaxiras, Nano Lett. **13**, 898 (2013).

[121] S. H. Lee, C. W. Chiu, and M. F. Lin, Physica E: Low-dimensional Systems and Nanostructures **42**, 732 (2010).

[122] K.-A. N. Duerloo, M. T. Ong, and E. J. Reed, J. Phys. Chem. Lett. **3**, 2871 (2012).

[123] P. Ares, T. Cea, M. Holwill, Y. B. Wang, R. Roldán, F. Guinea, D. V. Andreeva, L. Fumagalli, K. S. Novoselov, and C. R. Woods, Adv. Mater. **32**, 1905504 (2020).

[124] M. Droth, G. Burkard, and V. M. Pereira, Phys. Rev. B **94**, 075404 (2016).

[125] R. Guerra, M. van Wijk, A. Vanossi, A. Fasolino, and E. Tosatti, Nanoscale **9**, 8799 (2017).

[126] L. Wang, S. Zihlmann, M.-H. Liu, P. Makk, K. Watanabe, T. Taniguchi, A. Baumgartner, and C. Schönenberger, Nano Lett. **19**, 2371 (2019).

[127] B. Cheng, C. Pan, S. Che, P. Wang, Y. Wu, K. Watanabe, T. Taniguchi, S. Ge, R. Lake, D. Smirnov, C. N. Lau, and M. Bockrath, Nano Lett. **19**, 4321 (2019).

[128] E. Wang, X. Lu, S. Ding, W. Yao, M. Yan, G. Wan, K. Deng, S. Wang, G. Chen, L. Ma, J. Jung, A. V. Fedorov, Y. Zhang, G. Zhang, and S. Zhou, Nature Physics **12**, 1111 (2016).

[129] G. Giovannetti, P. A. Khomyakov, G. Brocks, P. J. Kelly, and J. van den Brink, Phys. Rev. B **76**, 073103 (2007).

[130] Y. Guo, J. Qiu, and W. Guo, Nanoscale **8**, 575 (2016).

[131] K. Nagashio, T. Nishimura, and A. Toriumi, Appl. Phys. Lett. **102**, 173507 (2013).

[132] W.-J. Jang, H. Kim, Y.-R. Shin, M. Wang, S. K. Jang, M. Kim, S. Lee, S.-W. Kim, Y. J. Song, and S.-J. Kahng, Carbon **74**, 139 (2014).

[133] V. S. Mangu, M. Zamiri, S. R. J. Brueck, and F. Cavallo, Nanoscale **9**, 16602 (2017).

1 Fabrication Recipes

The details of the fabrication recipes used will be discussed in the following.

1.1 Preparation of flexible substrate

1. Cut the 0.3 mm/ 0.2 mm thick large phosphor bronze plate into pieces of 5 cm × 5 cm.

2. Polish the surface of the plate with a lapping machine. The plate is fixed to a holder

3. Spin coat polyimide with a two-step procedure:

   500 rpm/1 s/10 s

   2500 rpm/5 s/60 s.

4. Soft bake at 170 °C for 3 min.

5. Repeat spin coating and soft baking (steps 3,4) for two more time to get ticker polyimide film on the plate.

6. Polyimide curing: increase the temperature from 170 °C to 350 °C with rate 4 °C min^{-1}, bake at 350 °C for 30 min then switch off the hot plate, let it cool to room temperature.

7. Spin coat a thick PMMA layer (∼1 µm) to protect the polyimide surface before cutting into smaller pieces using a diamond wire saw.

1.2 Fabrication of hBN encapsulated graphene

1.2.1 Exfoliation

1. Dicing the fresh Si (with ∼285 nmthick SiO_2) wafer into appropriate sizes (∼1 cm × 1 cm).

2. Blow the cut Si wafer with N_2/compressed air to remove any particles from dicing .

3. Exfoliate graphene or hBN on the wafer and identify them with an optical microscopy.

4. Heating treatment can be used to increase the exfoliation yield especially for graphene.

1.2.2 Polycarbonate(PC) solution preparation

1. Mix 0.8 g of PC with 20 ml of chloroform($CHCl_3$)

2. Continuous overnight stirring for around 12 h will result in dissolving PC in $CHCl_3$.

1.2.3 Assembly of hBN/graphene/hBN stacks

1. PC film preparation: drop caste PC solution (dissolved in chloroform with 9 wt%) on a glass slide. Use a second glass slide to press and slide against the first glass slide immediately. Let them dry in a fume hood.

2. Use a piece of scotch tape with a widow ($\sim$1 cm $\times$ 1 cm) cut in the center to transfer the dried PC film onto a PDMS stamp $\sim$0.5 cm $\times$ 0.5 cm, which is mounted on a glass slide.

3. Pick up top hBN layer with the PC film at $\sim$80 °C.

4. Pick up the graphene and the bottom hBN sequentially in the same way.

5. Place down the assembled stack onto the target substrate by heating to 170 °C to release the PC layer from the PDMS.

6. Remove PC film from the target substrate with chloroform ($\sim$1 h). Chloroform dissolves the PC fim while the stack will be adhered to th e target substrate.

1.3 E-beam lithography and development

1.3.1 PMMA resist with cold-development

1. Spin-coat 420 nm PMMA and bake at 180 °C for 3 min.

2. Expose with E-beam (V = 20 keV; Dose = 450 µC/cm^2).

3. Cold-development in IPA:H_2O (ratio 7:3) at $\sim$5 °C for 60 s, blow-dry.

1.4 Reactive ion etching

1.4.1 CHF_3:O_2 plasma

1. Parameters: CHF_3:O_2 (80 sccm/4 sccm), P =60 W, p =60 mTorr. This plasma is used to cut the stack with a controlled etching time for evaporating edge contacts.

2. Etching rates:

   hBN: ∼20 nm/min

   PMMA: <10 nm/min

   Polyimide: negligible

1.4.2 SF_6:Ar:O_2 plasma

1. Parameters: SF_6:Ar:O_2 (76 sccm/3.6 sccm/5 sccm), $P = 50$ W, $p = 25$ mTorr. This plasma is used to shape the stack.

2. Etching rates:

   hBN: >300 nm/min

   SiO_2: ∼30 nm/min

   PMMA: ∼80 nm/min

It is important to do a short O_2 plasma etching after each SF_6 plasma etching step to remove the cross-linked PMMA layer due to SF_6 plasma.

1.4.3 Ar/O_2 plasma

1. Parameters: Ar:O_2 (22 sccm/8 sccm), P =30 W, p =80 mTorr. This plasma is used to remove PMMA or to etch and shape graphite.

2. Etching rates:

   hBN: ∼2 nm/min

   PMMA: ∼ 68-70 nm/min

   graphene: ∼ 6-8 nm/min

1.5 Metal evaporation

1.5.1 Cr/Au leads

1. Type: E-beam evaporation

2. Pumping to base-pressure of $<2 \times 10^{-7}$ Pa
3. Evaporate away ∼30 nm of Cr before opening the shutter, since the Cr-target oxidizes in ambient condition, where it is stored.
4. Open shutter
5. Evaporate 5 nm of Cr (0.7 Å/s to 1.2 Å/s)
6. Evaporate 110 nm of Au (0.7 Å/s to 1.2 Å/s)

2 Lever arm calculation in dual gated BLG devices

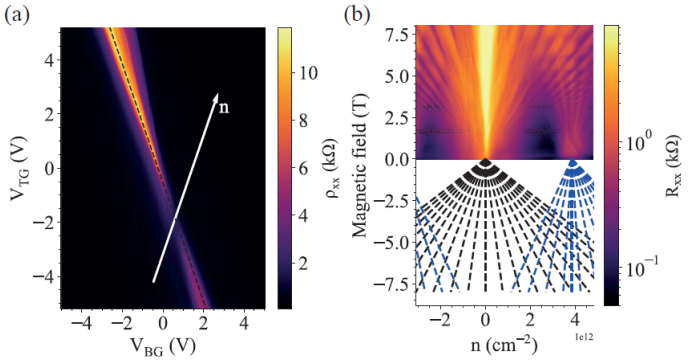

Figure 2.1 (a) Resistivity as a function of the top gate and bottom gate voltage. The bright region is the CNP line, the black dashed line is a fit to the CNP line. (b) Landau fan plot. ρ_{xx} with respect to n and B. As a guide to the eye, the landau levels from CNP of BLG are shown with black dashed lines.

2.1 Lever arm

The procedure used to obtain lever arms, c_t and c_b are the following : The measured twodimensional resistance map as a function of the top gate(V_{tg}) and bottom gate voltages(V_{bg}) as shown in Fig. 2.1(a). Ideally in the BLG as a gap opens with electric field, we see a highly resistive line (CNP line), which has a minimum and from there it increases monotonically with electric field. By fitting a line on it, we can extract the lever arm ratio (c_b/c_t). Let $m = c_b/c_t$

The charge density (n) and electric displacement field (D) is related to the

top and bottom gate voltage by,

$$n = (c_t V_{tg} + c_b V_{bg})/e + n_0 \tag{2.1}$$

The effective average displacement field(D) can be written as,

$$D = \frac{(c_t V_{tg} - c_b V_{bg})e + D_0}{2} \tag{2.2}$$

where n_0 and D_0 are the offset doping and offset displacement field in the system. In Fig. 2.1(a), the CNP line is chosen as n = 0 and the resistance minimum along CNP line gives the location of D = 0 . The (V_{bg},V_{tg}) corresponding to D = 0 is noted down and is used to solve Eq. 2.1,. 2.2 along with using m. This gives n_0 and D_0. Let's choose $c_t = 1$, then c_b = m. Thus,

$$n - n_0 = (V_{tg} + mV_{bg})/e \tag{2.3}$$

The next step is to do a quantum hall measurement by measuring the resistance as a function of applied magnetic field and charge density at the D = 0 line, which is shown as a white arrow in Fig. 2.1(a). In the quantum hall measurement, from identifying a known filling factor(ν) the exact density can be calculated(n_{qhe}). Now compare the density calculated from quantum hall and that to Eq. 2.3.

$$n_{qhe} = (eB/h)\nu \tag{2.4}$$

where B is the magnetic field. Also, $n_{qhe} = (c_t V_{tg} + c_b V_{bg})/e$. Thus we get,

$$\frac{n_{qhe}}{n - n_0} = c_t \tag{2.5}$$

as m = c_b/c_t. Once we know c_t, $c_b = mc_t$
The lever arm obtained are : $c_t = 3.60 \times 10^{-4}\mathrm{V}^{-1}\mathrm{m}^{-2}$, $c_t = 7.90 \times 10^{-4}\mathrm{V}^{-1}\mathrm{m}^{-2}$.

The offsets are : $n_0 = 1.8 \times 10^{15}\mathrm{m}^{-2}$, $D_0 = 0.065$ V/nm.

Publications

- *"Global strain-induced scalar potential in graphene devices"*
  L. Wang, A. Baumgartner, P. Makk, S. Zihlmann, B.S. Varghese, D. I. Indolese, K. Watanabe, T. Taniguchi and C. Schönenberger
  Commun Phys **4**, 147 (2021).

Talks

- *Controlled Strain engineering in graphene electronic devices*
  7th Graphene Workshop, Basel(Switzerland), August 2023

Poster Contributions

- *"Scalar potential effects in deterministically strained graphene"*
  Graphene2021, Grenoble (France), October 2021

Acknowledgements

It was an important phase in the life when I look back. Met lot of new people, far away from home, learned lessons in both science and life, got the opportunity to try out different sport and outdoor activities. This PhD thesis would not have been possible without the help and support from many people. In the following, I would like to express my sincere gratitude to all of them for their precious contributions.

First of all thanks Chrisitian for hosting me as phd in the nanoelectronics lab for the strain engineering project. The name of project sounded cool and the project really had quite some engineering in it. Thanks for the nice discussions and few insights in the physics of strain engineering. I really appreciate the effort Christian puts in to make the lab environment better by keeping regular summer and winter group trips, also the Christmas dinner plus many more lab events which create enough chances to mingle with everyone in the group. I think this good atmosphere in lab is really important in a phd life. Also, the activeness and enthusiasm of Christian towards sports like biking, running always motivated and helped me realize sports can really keep the life more active.

Secondly, I thank Andreas for all the support and discussions involved with the project during last four years. It is quite interesting to see him involved in almost all the scientific discussions in the lab. I don't know how he manages time to find time for all. Also, the small theoretical insights and the list of possibilities for an observation from him is really nice.

Then, I would like to thank Prof. Dr. Christoph Stampfer and Prof. Dr. Adrian Bachtold for making the effort to read my thesis. It is my great honor to have two such excellent physicists in my PhD committee.

When I joined the group, it was quite big, around 30 members in the lab but during my four years I could see the transition to a smaller group. I would like to thank all the previous members of the group for their help and support. Thanks to David for initially teaching 2D material fabrication procedures. Then I would like to thank Lujun who introduced me to the strain

project and taught the fabrication procedures specific to the project, also the nice discussions on the measurement data eventhough most of the time we failed to understand the effects of strain. Thanks to the 2D subgroup which I guess started during the CoVID time and the members of the subgroup Ian, Mehdi, Zarina, Paritosh, Artem, Martin, Rounak for all the subgroup meetings and suggestions from them and also to the nice times of trying exfoliation together to get hBN flakes, graphene, graphite. At some point it was really difficult to find clean hBN flakes. Thanks to Paritosh for the in between small discussions of physics moiré superlattices and other topics in 2D materials to get a picture of it from a understanding point of view.

I would like to thank Sascha Martin from mechanical workshop who helped us to realise the strain setup we built and for all his support in the project. Next, I would like to thank Sascha Linder for all his support regarding the design we worked together for the electrical clamps for the devices in the new strain setup

Then I would like to thank the initiative Mehdi undertook to oragnise movie nights once in a while, that was really nice and helped to go through cinema's all over the world, could see the differnces in the style of movies from different regions. Those were really good times. Thanks to Arunav, to push us intially to start with Klettersteig, it was an amazing experience. Started with the easy level and then pushed a bit to the just next higher one but not too far. I would like to thank usual group activity organisers LukYi, Alessia (not the group trips) for movies, escape rooms and many more. The VR gaming was an amazing experience with LukYi, Alessia and Deep. It was as intensive as running in Sola Basel, the zombie game involved lot of running, got really exhausted. I hope we would go for more of it. The in between evening football games during the beginning of PhD was really nice, Matthijas and Carlo the best palyers I guess from our group. It was fun, I hope in the group we will find sometime to play football again. Thanks to all the group trip organisers : Martin, Alessia, Ian, Carlo who do such a good job in arranging and organising everything. Thanks Han, Deep, Rounak for the in between short table tennis game which help to motivate a bit in the lab. I would like to thank Lukyi for joining the bike trip to Freiburg and Zurich, it was a nice experience and the first time for me to go on such long distances on bicycle. The strawberry fields on the way Freiburg by road is a refreshing point to realise the nice taste of it. The Sola Basel event is a memorable one, I have not run that many long distances before coming to Basel, only once or twice a 5K. But Sola Basel motivated me to run more and the group event was really nice. The last run with the group in Sola Basel was really nice and also the BBQ aferwards it. Special thanks also go to many people behind the scene at the Physics Department. Barbara Kammermann and Astrid Kalt were the best secretaries I have ever met, from whom I got extremely helpful assistance to all administrative work.

I would also like to thank Dominik Sifrig for the supply of helium, Patrick Stöcklin for the help in the cryolab, Daniel Sacker and Laurent Marot for the help with the cleanroom.

I would like to thank the people with whom I live in the student dorm in Basel for making the last 4 years memorable. All the amazing kitchen dinners, movie night, watching football was all really nice. Thanks Agni for offering his screen to help my thesis writing at home. Also, I would like to thank all the members of green kitchen who motivated me in the writing of this thesis. Thanks Sela, Hari for all the help and support for all the coding related doubts and for the motivation. I would take this oppurtunity to thank the friends who I met here but still from Kerala to whom I can talk my mother tongue. Hari, Rohan, Devi , Anupa, Ajmal, Jikson, Jibin 1, Jibin 2, Amal, Nanditha for all the good times spent to cook together dishes back from home and for all the fun trips. Excited to the ongoing Cricke world cup to watch together with you all including Rounak and Deep.

Thanks to all my friends back from India who motivated me the whole time. Lot of thanks to our old Whatsapp group "Push Karo Kush Raho" to help me stay in touch with friends from my masters. Thanks Ambili for all the phone calls and nice time we had together, I will not forget it.

Thanks to my parents (Varghese and Mary), Jesson (brother), Neethu(sister-in-law) and all my other relatives who supported and backed me this whole journey in Phd.